Nano-petrophysics study of Haynesville Shale, East Texas, USA

by

Qiming Wang

Thesis

Presented to the Faculty of the Graduate School of

The University of Texas at Arlington in Partial Fulfillment

of the Requirements

for the Degree of

MASTERS OF SCIENCE IN EARTH AND ENVIRONMENTAL SCIENCES

THE UNIVERSITY OF TEXAS AT ARLINGTON
May 2019

Nano-petrophysics study of Haynesville Shale,
East Texas, USA

Qiming Wang, M.S.
The University of Texas at Arlington, 2019

Supervising Professor: Qinhong (Max) Hu

As one of the most productive shale gas plays, the Haynesville Shale has a high geopressure gradient and high temperature, but with a lack of petrophysical understanding. To analyze the pore geometry and wettability related connectivity of this formation, multiple methods such as total organic carbon content (TOC), X-ray diffraction (XRD), vacuum saturation, mercury intrusion capillary pressure (MICP), contact angle, fluid imbibition, and helium pycnometry were used on 10 Haynesville Shale core samples from a single well over a vertical distance of 123 ft. The results from those tests show that the Haynesville Shale is calcareous shale with 2.26~5.28% of TOC. The porosities range from 3 to 8%, and the pore-throat sizes are concentrated at the nanoscale (2.8~50 nm). Moreover, the permeability and effective tortuosity of the pore network controlled by 2.8 to 50 nm pore-throat size are 3.7 to 23.4 nD and 1413 to 3433, respectively. All ten samples show strong oil-wet characteristics and only three samples exhibit mixed wettability (both oil-wet and water-wet). In general oil-wet samples show higher pore connectivity when they imbibe hydrophobic (a mixture of n-decane:toluene at 2:1, as an oil analog) than hydrophilic (deionized water) fluids.

Table of Content

List of Figures

List of Tables

List of Abbreviations Used

CT	Computed tomography
DIW/ DI Water	Deionized Water
DT2	N-decane: toluene at 2:1 in volume
FE-SEM	Field emission-scanning electron microscopy
FIB-SEM	Focused ion beam-scanning electron microscopy
FID	Flame ionization detector
nD	Nano-darcy
NMR	Nuclear magnetic resonance
MICP	Mercury intrusion capillary pressure
PI	Production index
THF	Tetrahydrofuran
TOC	Total organic content
SANS	Small-angle neutron scattering
SAXS	Small-angle X-ray scattering
USANS	Ultra-small angle neutron scattering
XRD	X-Ray diffraction
cm	Centimeter
μm	Micrometer
nm	Nanometer

Acknowledgments

I would like to thank my advisor, Dr. Qinhong Hu for his constant and patient guidance, support, and encouragement over the past two years, which motivated and inspired me to take steps which I never thought that I could make. I very much appreciate the opportunity he provided to work in his research group and with other collaborators. I would also like to thank my committee member Mr. Fred Meendsen who provided samples and spent his time working with me to make this research possible. I would like to thank Dr. John Wickham for his advice on my thesis work and graduate life in the department.

Thanks to the folks at UTA, especially Gang Lei, Yuxiang Zhang, Md Golam Kibria, Ahmad Rabbani, and Ayobami Ojo for their help.

Special thanks to Dr. Wan Yang and Dr. Mingli Wan who taught me the value of how to be a real scientist. I will always keep honesty, hard work, devotion, and acumen in my mind.

In the end, I would like to thank my parents for their undying love and support.

Petroleum exists in geologists' minds.

Chapter 1: Introduction

1.1 Introduction

Shale gas, as a type of clean fossil fuel, was first economically produced in the Barnett Shale by the development of hydraulic fracturing and horizontal drilling (Institute for Energy Research, 2011). After decades of exploration and production, shale gas industry is facing a critical problem that shale gas production always exhibits sharp declines after months or years of production (Baihly et al., 2010). Shale gas recovery behavior can be related to reservoir quality and liquid & gas movement in a complex shale matrix. In order to obtain consistent production and reduced decline rate, researches on the understanding of hydrocarbon migration behavior in tight shale has attracted more attention (Dehghanpour et al., 2013; Dehghanpour et al., 2012; Gao & Hu, 2016b; Javadpour et al., 2007; Lan et al., Makhanov et al., 2012; Roychaudhuri et al., , 2013; Shen et al., , 2016; Slatt & O'Brien, 2011; Swami & Settari, 2012; Yang et al., 2017; Yuan et al., 2014; Zhou et al., 2014).

The Late Jurassic was one of the best times for the formation of organic-rich source rocks (Klemme, 1994). The Haynesville Shale was first commercially produced in 2008 by Chesapeake Energy Corp; it was estimated to hold 75 trillion cubic feet of recoverable gas in 2011 and 195 trillion cubic feet in 2017 (Instititure for Energy Research, 2011; U.S. Energy Information Administration, 2011; U.S. Geological Survey, 2017). From 2008 to 2009, 275 horizontal wells were drilled in the Haynesville formation and reached its first production peak in 2011-2012 (Baihly et al., 2010; Rystad Energy, 2019). After three years of decline, production in the Haynesville bounced back in the fourth quarter of 2017 (Figure 1). The primary reason for this bounce was the design of new drilling and completion operations (Oil & Gas Journal, 2018).

As one of the significant factors in gas recovery, pore structure and fluid movement study of the Haynesville Shale is not available in the literature. This study selected ten core samples from the Haynesville formation with different mineral compositions, organic richness, and depth from a gas-producing well. Integrated laboratory analyses of mineralogy, organic richness, thermal maturity, pore structure, and fluid movement behavior of the Haynesville Shale will provide a significant reference to evaluate reservoir quality and enhance gas recovery.

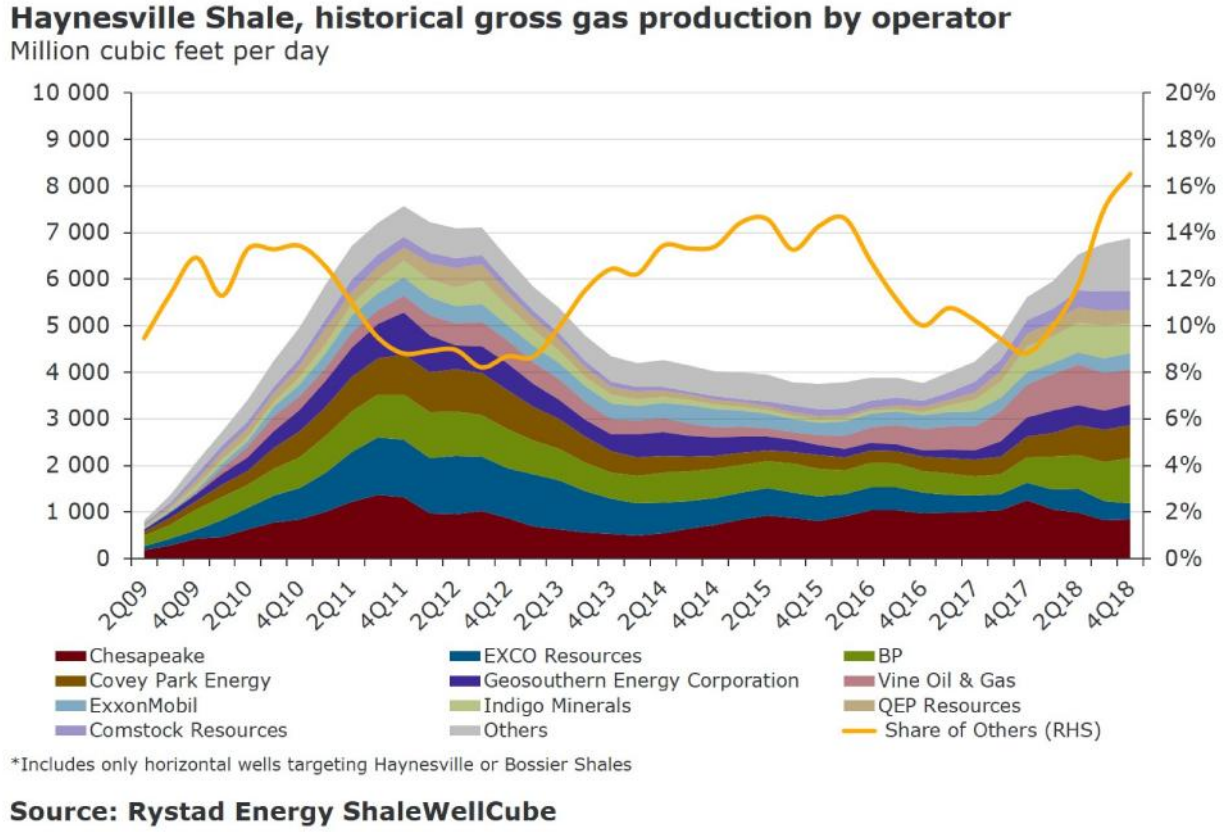

Figure 1. Haynesville Shale, historical gross gas production by operators (Rystad Energy, 2019).

1.2 Literature review

1.2.1 Nano-scale shale characterization

As a type of unconventional hydrocarbon reservoir with low porosity, ultra-low permeability, and high total organic carbon content (TOC), shale attracted world-wide attention in past decades (Euzen, 2011; Ground Water Protection Council, 2009; Lu et al., 2016; Reig et al., 2014; Slatt, 2011). To maximize and stabilize shale gas production, having a better understanding of shale is the first mission in shale study. Folk (1980) and Boggs (2009) named shale as fissile and laminated mudstone. By using traditional technologies such as outcrop core description and thin section study, detailed information of shale is hard to be obtained. Consequently, Boggs (2009) suggested to utilize X-ray diffraction and scanning electron microscopy to study the shale petrology. In the oil industry, petrology studies of shale alone are not enough to characterize and evaluate shale reservoir quality. Over the past decades, combined with conventional reservoir characterization technologies such as TOC, pyrolysis, seismic interpretation and well logs, high-resolution tools have been adopted in shale research (Lu et al., 2016; Sondergeld et al., 2010). High-resolution imaging techniques such as field emission-scanning electron microscopy (FE-SEM), focused ion beam-scanning electron microscopy (FIB-SEM), micro-CT (computed tomography) imaging, and nano-CT imaging and petrophysical methods such as mercury intrusion capillary pressure (MICP), N_2 and CO_2 sorption isotherm, spontaneous imbibition, gas diffusion, nuclear magnetic resonance (NMR), small-angle X-ray scattering (SAXS), small-angle neutron scattering (SANS) and ultra-small angle neutron scattering (USANS) give researchers opportunities to investigate pore structure and fluid movement behavior in shale. In the oil

industry, petrophysical analyses more refer to seismic interpretation and well log analysis. Here, in this study, nano-petrophysical analyses are employed to investigate micro-nanometer features of pore space or show fluid movement behavior in shale.

Shale gas production is facing challenges from several aspects. In this study, we are focusing on two significant problems in both the production and environmental aspect. The first challenge is inaccurate reservoir quality evaluation. Lu et al. (2016) asked what properties a shale needs to be considered as a producible reservoir. Establishing a general reservoir quality evaluation system could help oil companies reduce costs caused by inadequate reservoir quality evaluation. The second challenge is water resources (Kargbo et al., 2010; Wang et al., 2014). Table 2 shows a large amount of fresh water being consumed during the hydraulic fracturing (U.S. Environmental Protection Agency, 2016). During the flowback stage, only around 10% to 40% of fracturing fluid could be recovered from the subsurface (Arthur et al., 2008).

To conquer those two challenges, petrophysicists have started to shift their attention from conventional reservoirs (sandstone and carbonate rocks) to unconventional reservoirs (shale). A series of petrophysical parameters is employed to characterize shale properties. Porosity, pore volume, pore-throat distribution, permeability, wettability, connectivity, and diffusivity are the most critical petrophysical parameters (Chen et al., 2011; Clarkson et al., 2013; Gao & Hu, 2016b; Gao et al., 2013; Hu et al., 2012; Neithalath et al., 2010; Peng et al., 2012). In this study, only experiment-based studies will be discussed.

State	Number of FracFocus 1.0 Disclosures	Median Volume per Well (gallons)	10th percentile (gallons)	90th percentile (gallons)
Arkansas	1,423	5,259,965	3,234,963	7,121,249
California	711	76,818	21,462	285,306
Colorado	4,898	463,462	147,353	3,092,024
Kansas	121	1,453,788	10,836	2,227,926
Louisiana	966	5,077,863	1,812,099	7,945,630
Montana	207	1,455,757	367,326	2,997,552
New Mexico	1,145	175,241	35,638	1,871,666
North Dakota	2,109	2,022,380	969,380	3,313,482
Ohio	146	3,887,499	2,885,568	5,571,027
Oklahoma	1,783	2,591,778	1,260,906	7,402,230
Pennsylvania	2,445	4,184,936	2,313,649	6,615,981
Texas	16,882	1,420,613	58,709	6,115,195
Utah	1,406	302,075	76,286	769,360
West Virginia	273	5,012,238	3,170,210	7,297,080
Wyoming	1,405	322,793	5,727	1,837,602

Table 1. Introduction of shale pore structure characterization methods.

1.2.2 Pore structure

Pore structure parameters (porosity, pore type, and pore size distribution) are among the first concerns in the evaluation of highly heterogeneous reservoirs. To accurately predict resource potential, pore structure parameters play a critical role (Jarvie, 2012). In the oil industry, SEM, CT, gas adsorption, mercury injection capillary pressure (MICP), helium porosimetry, fluid saturation method, and nuclear magnetic resonance are currently the most popular porosity measurement methods (Li et al., 2019; Rodriguez1 et al., 2014). Those porosity and pore structure characterization methods have their unique functions and detection ranges (Table 2).

To study the pore type and 3D pore distribution, Rodriguez1 et al. (2014) introduced the most popular shale study imaging tools. While SEM imaging was widely used in materials science, Loucks et al. (2009) first applied SEM to shale research. Only one year later, more than 20 publications followed up this method. Shale pore types are classified as organic pores,

interparticle pores, intraparticle pores, and intercrystallite pores (Loucks et al., 2009; 2010). Porosity can be determined by helium pycnometry, fluid saturation, and MICP. Helium pycnometry can measure grain density (and hence porosity) without subjecting samples to liquids, which the other two methods could not achieve. Usually, the fluid saturation method is only associated with water. However, additional fluids with different wettabilities could also be introduced in this method to test the relationship between measured porosity vs. wettability. MICP is the most functional method among those three; it can not only generate porosity but also reveal the pore-throat distribution and pore volumes in different pore systems over μm-nm ranges. In addition, pore-size distribution is another parameter which merits more attention. As a significant parameter to characterize the pathways of hydrocarbon migration (Slatt & O'Brien, 2011), the pore-size distribution provides necessary information for hydrocarbon production and reservoir simulation (Michel et al., 2011; Tian et al., 2019).

Method	**Pore size detection line**	**Major function**
SEM	~5 nm	2D Imaging
CT	~50 nm	3D Imaging
Gas Adsorption	0.33–100 nm	Pore size distribution
MICP	2.8 nm to 1000 um	Porosity and Pore size distribution
NMR	~0.1-10,000 nm	Pore size distrinition measured by different wettability fluids
Helium Porosimetry	All pore sizes larger than the molecular sizes of Helium (0.14 nm)	Porosity
Fluid Saturation	All pore sizes larger than the molecular sizes of water (0.275 nm)	Porosity measured by different wettability fluids

Table 2. Introduction of shale pore structure characterization methods.

1.2.3 Permeability

Permeability is an important parameter to quantify the degree of difficulty for fluids to pass through porous media. Hydrocarbon migration in the reservoir is highly related to permeability. Unlike pore structure characterization, which is easy to conduct, a permeability determination is challenging. Current laboratory methods of permeability determination of shale matrix include (1) gas expansion for core and crushed samples; (2) mercury intrusion (Cui et al., 2009). When applying the gas expansion method on the core and crushed samples, permeability results always conflict, and the causes of this are still being debated (Peng & Loucks, 2016; Tinni et al., 2012). Due to the high experimental cost, long duration, and controversy of the gas expansion method, it is not being considered in this study. Over the recent 20 years, many studies have attempted to use MICP data to estimate permeability (Brown, 2015; Daigle, 2016; Gao & Hu, 2013; Hunt & Gee, 2002). MICP can analyze one sample within several hours and generate pore structure, permeability, and tortuosity. Considering the time and cost, MICP permeability approach could be used as an alternative method.

1.2.4 Tortuosity

Tortuosity is defined as the fraction of traveled distance over a straight line between two points (Schlumberger Oilfield Glossary, 2019). It can reflect the complexity of pore space and hydrocarbon pathway morphology (Ghanbarian et al., 2013). When fluids migrate in a porous media, they spend less time in transit through porous media with lower tortuosity. CT, acoustic absorption, reflection wave, diffusion diaphragm, and MICP were reported to be utilized to determine the tortuosity of porous media (Diao et al., 2017; Fellah et al., 2003; Gommes et al.,

2012; Hu et al., 2017). As mentioned in the previous chapter, MICP is utilized to determine the tortuosity to save time and reduce cost.

1.3 Problems of petrophysical study in the Haynesville Shale

Petrophysical studies in the Haynesville have two major problems. The first problem is that the samples chosen are not representative enough. Some studies only use 2-5 samples to characterize the whole formation. For a geological formation, especially a thick oil and gas producing formation, a small number and random sample selection cannot reflect the true reservoir quality. In the oil industry, this problem will enhance the unnecessary cost caused by poor quality reservoir evaluation. The second problem is the resolution of the experiments. In the oil industry, the popular petrophysical analysis methods are well logging and seismic interpretation, which are only useful methods for large scale interpretation. However, when down to the nano-scale, they are not applicable anymore. To investigate nanoscale features and fluid flow behavior in the Haynesville Shale, nano-petrophysical methods such as MICP and spontaneous fluid imbibition are utilized in this study.

1.4 Study Objectives

The purposes of this study were to characterize the Haynesville Shale, evaluate reservoir quality of different interest zones, and provide valuable conclusions for the operators to explore the Haynesville Shale.

The specific research objectives of this study were to (1) investigate petrophysical properties of the Haynesville Shale such as TOC, mineral composition, wettability, porosity, permeability, tortuosity, wettability related connectivity; (2) characterize fluid movement behavior in the shale samples; and (3) evaluate reservoir quality with higher vertical resolution.

Chapter 2 Geological background

2.1 Geological setting

The Haynesville Shale is a package within the upper part of the Upper Jurassic Haynesville Formation and was deposited in an area in northeast Texas and northwest Louisiana in the northern Gulf of Mexico basin (noted by the red outline in Figure 2). It overlays the Smackover limestone and is succeeded by the Bossier Shale. The Haynesville Shale was deposited in the area bounded by the Rodessa fault and the North Louisiana fault zone in the north, by the East Texas salt basin and North Louisiana to the east and west, and by the Sabine Island complex in the south. The total area of the Haynesville covers 9,000 square miles (Ground Water Protection Council, 2009). Structure, depositional model, and stratigraphy of the study area have been studied in detail by others (Adams, 2009; Cicero & Steinhoff, 2013; Ewing, 2009; Galloway, 2008; Goldhammer, 1998; Hammes & Frébourg, 2012; Hammes et al., 2011; Mancini et al., 2008; Nunn, 2012). Briefly speaking, the opening of the Gulf of Mexico and Sabine uplift played a critical role in the Haynesville Shale deposition, in creating accumulation space and introducing sea water to this passive margin basin. The Sabine uplift area did not cause subsidence during the Jurassic, which makes itself a relatively high land in the middle of the basin. Haynesville sediments were deposited along the east and west flanks of the uplift forming two depocenters. The western depocenter lies approximately in Leon County, eastern Texas, and the east depocenter is found in Harrison County, TX and Caddo County, LA.

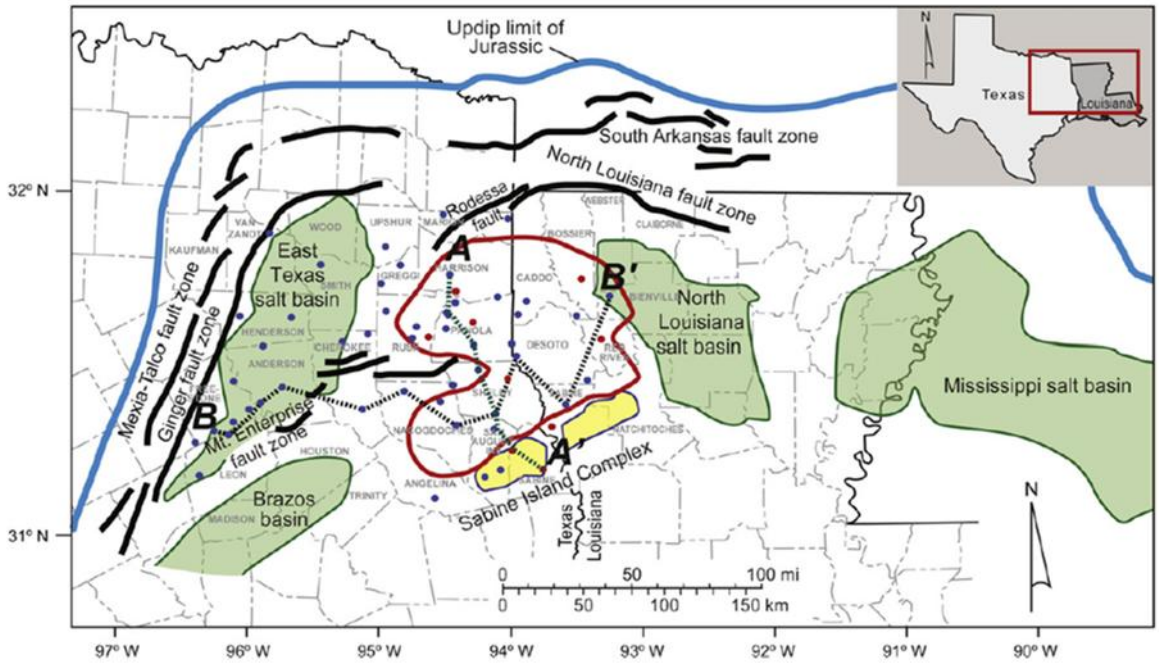

Figure 2. Location and geological features around the Haynesville Formation, outlined in red. (Hammes & Frébourg, 2012)

2.2 Haynesville Shale

The Haynesville Shale is at least partially time equivalent to the carbonate-rich Gilmer and Haynesville Lime members of the Haynesville Formation (Figure 3). However, the lithology of the overall Haynesville Formation includes carbonates, siliciclastic, and to a lesser extent evaporites (Figure 4). The lithological variation is related to the shifting of depositional environments. In northeast Louisiana and western Mississippi, siliciclastic input from the ancestral Mississippi river was dominant (Cicero & Steinhoff, 2013), whereas in east Texas, Gilmer/Haynesville lime carbonate production was dominant, fringing the Haynesville Shale to the west and south (Cicero & Steinhoff, 2013; Torsch, 2013). In general, the Haynesville Shale is an organic-rich mudstone. In previous studies (Hammes & Frébourg, 2012; Hammes et al., 2011; Keator, 2018), researchers came up with several kinds of lithofacies classifications based on

compositional and sedimentary structures. In the northern part of the basin, the Haynesville Shale received terrestrial sediments from three directions, which make the mudstone more siliciclastic rich and has relatively lower TOC contents. In the south, close to the Sabine uplift, the mudstone is more calcareous rich and has higher TOC values (Hammes et al., 2011). In the whole area, the organisms present are major planktons, shallow water benthic dwellers, swimming bottom-dwellers, and algae. Foraminifera, radiolaria, filibranch mollusks, ammonites, pelecypods, sponge spicules, and calcispheres have been reported in the core and thin section scales (Hammes et al., 2011). After death, the organisms sank to the sea floor. The shells and bones became calcareous grains, and the dead bodies, bacteria, and algae became the source of sedimentary organic matter. In summary, this organic-rich black Haynesville Shale was deposited under anoxic shallow marine conditions behind the high energy carbonate buildups, stranded rift blocks.

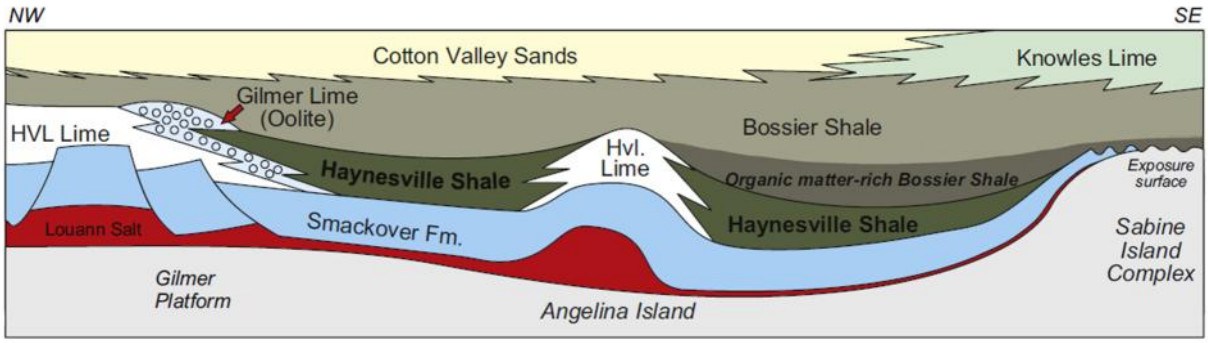

Figure 3. Cross-section of the northern Gulf of Mexico Basin (Hammes and Frébourg, 2012).

The Haynesville Shale is the rapid burial of the overlying lower Cretaceous sediments deposition (Nunn, 2012). The present day temperature in the Haynesville Shale ranges from 260°F (125°C) to 380°F (195°C) (Speight, 2017). The geothermal gradient in the mid-Cretaceous is estimated to

have been about 0.33°F/ft. With heat dissipation over time, geothermal gradients decrease to 0.0135 to 0.02°F/ft at present (Nunn, 2012). With the properties of high geopressured gradients and high ancient temperature gradient, the Haynesville Shale is a vitally important area to study the relationship between pore structure and porosity, permeability, pore size distribution, pore connectivity, and pore types. For example, relationships among high pressure, porosity, and permeability in Haynesville Shale show that the porosity and permeability increased significantly with an increase in pressure (Boosari et al., 2016).

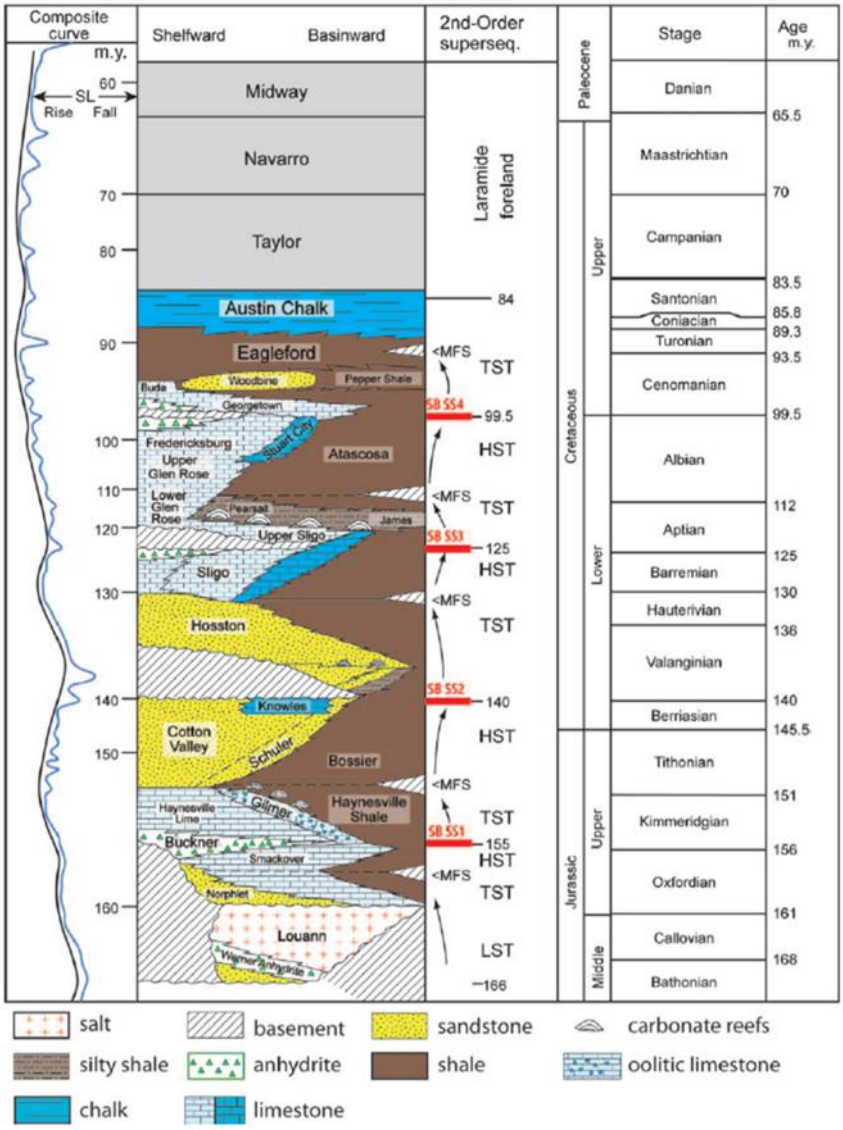

Figure 4. Stratigraphic column of northern Gulf of Mexico Basin (Goldhammer, 1998; Hammes, 2011)

Chapter 3 Methods

3.1. Sample selection, collection, and processing

A total of ten samples was collected from a well located in San Augustine County, Eastern Texas. The samples were selected based on well logs which were used to help locate interesting depths to sample; Table 3 shows basic sample information.

Sample ID	Depth (ft)	Selection Criteria
BS 14359	14358.5	Low clay contant
BS 14374	14374	High porosity
BS 14395	14395	Upper carbonate-rich zone
BS 14404	14404	Mud-rich zone between two carbonate-rich zone
BS 14411	14411	Lower carbonate-rich zone
BS 14427	14426.5	High porosity
BS 14433	14432.5	Hot and low porosity
BS 14446	14446	Hot and high porosity
BS 14462	14462	Hot and high porosity
BS 14482	14482	Hot kitchen

Table 3. Sample depth and selection criteria; BS denotes the abbreviation of the well name.

Samples were first weighed and photographed. 2.5 cm diameter core plug(s) were then taken using a coring machine. After coring, samples were cut into 1 cm^3 cubes and 0.4cm×1cm×1cm thin slabs with a steel saw. Each sample has at least ten cubes and four thin slabs. Rock fragments were then collected and crushed into six different sizes, #8 to #12 mesh, #12 to #20 mesh, #20 to #35 mesh, #35 to #80 mesh, #80 to #200 mesh, and <#200 mesh. Samples from #8/#12 mesh to #80/#200 mesh were washed with deionized water to remove the fines sticking on the sample surface. After being dried in the air, these granular samples were placed into glass jars. <200 mesh size samples were directly bottled for later use such as TOC analyses (Figure 5).

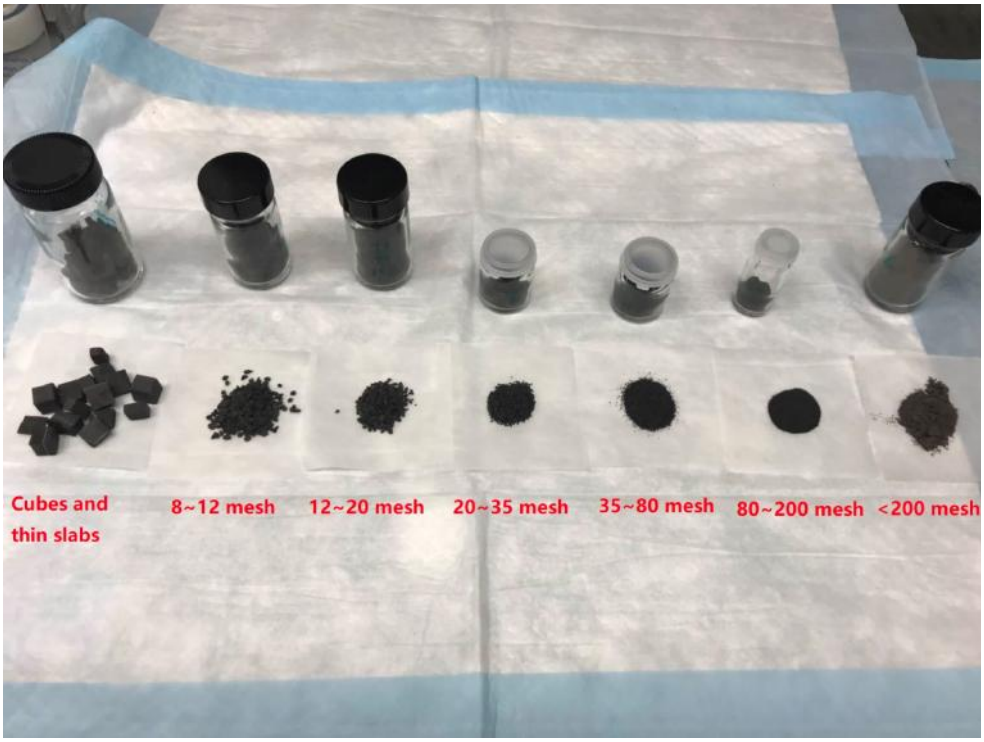

Figure 5. Sample photo with different sizes.

3.2. X-Ray Diffraction

X-Ray Diffraction (XRD) analysis, or X-Ray crystallography, is performed to qualitatively and quantitatively investigate the mineral composition of the rock sample. XRD measures the intensities and angle of beams diffracted by mineral crystals, and through spectrum analysis obtains the mineral compositions and weight percentages. XRD data was obtained using a Shimadzu MaximaX XRD-7000 (Figure 6).

Figure 6. XRD analyzer of Shimadzu MaximaX XRD-7000.

3.3 Pyrolysis and Total Organic Carbon

3.3.1 Pyrolysis

Samples of less than 75 μm were used to detect the organic matter richness and composition and the maturity of the source rock by pyrolysis. Pyrolysis analyses were performed with OGE-V Oil and Gas Evaluation Station (Figure 7) designed by the Research Institute of Petroleum Exploration and Development of PetroChina. According to Lafargue at al. (1998) and Tissot & Welte (1985), the parameter descriptions which are listed below associated with analysis temperature and duration (Table 4).

Figure 7. Pyrolysis analyzer of OGE-V Oil and Gas Evaluation Station.

	Descriptions	Analysis condition	Analysis Duration
S1 (mg HC/g)	The free hydrocarbons (HC) present in the sample before the analysis	300	180s
S2 (mg HC/g)	The volume of hydrocarbons that fromed during thermal pyrolysis	300 ~600	360s
S4 (mg HC/g)	The residual carbon content of the samples	600	60s
Tmax ( )	The temperature maximum point of hydrocarbon generateion during pyrolysis		

Table 4. Pyrolysis parameters and analysis condition.

3.3.2 Total Organic Carbon

TOC refers to the amount of total organic carbon in geological materials. TOC analyses were performed with Rapid CS Cube manufactured by the Elementar Company (Figure 8). High-temperature combustion is the most commonly used method in TOC analyses. By combusting samples at 1200 °C in an oxygen-rich reaction tube, all carbon converts to carbon dioxide which is detected by the sensor.

Figure 8. TOC analyzer of Rapid CS Cube.

3.3.3 Procedure of TOC analyses

The procedure of TOC analyses is straightforward. Samples less than 75 μm were oven-dried at 60 °C for at least 48 hours and then placed in the desiccator to be cooled to room temperature. Around 1 g for each sample was weighted and placed in a silver cup on a thermal-panel with the temperature at 60 °C. HCl was dropped into each silver cup to remove inorganic carbonate acids till no more reaction, followed with adding drops of de-ionized water for several rounds to wash out residual HCl. After completely dry, the sample was wrapped with the silver cup and fed to the TOC analyzer.

3.4 Helium Pycnometry

3.4.1 Introduction of Helium Pycnometry

The helium pycnometry is a work station to measure the grain density, and this test was conducted using a G-Denpyc 2900 (Figure 9). The mechanism of this test is the combination of the volume displacement method and gas expansion principle. First, we expanded a certain quantity of helium into the aluminum chamber at a previously set pressure P_1 to determine the empty chamber volume V_e. Second, we placed samples into the aluminum chamber and resealed the chamber. We flushed the same quantity of helium into the chamber, and recorded the chamber pressure P_2 after the chamber stabilized.

According to Boyle's Law and density equation,

$P_1 * V_e = P_2 * V_{gws}$

$V_e - V_{gws} = V_s$

$\rho_s = M / V_s$

P_1: pressure when chamber filled only with helium, Pascal

P_2: pressure when the chamber filled with both samples and helium, Pascal

V_e: gas volume when the chamber is empty, cm^3

V_{gws}: gas volume when chamber filled with samples, cm^3

V_s: sample grain volume, cm^3

M: sample weight, g

ρ_s: sample grain density, g/cm^3

Figure 9. G-Denpyc 2900 helium pycnometry.

3.4.2 Procedure of Helium pycnometry

Both cubic samples and granular samples were oven-dried at 60°C for 48 hours to remove moisture. Samples were taken out from the oven and placed in the desiccator to be cooled to room temperature. First, an empty aluminum chamber was placed in the analyzer to perform chamber volume calibration. Next, we filled the chamber with weighed samples and re-ran the analysis. Five tests were conducted, and an average grain density of five tests was reported.

3.5 Vacuum saturation

3.5.1 Introduction of Vacuum saturation

As a porosity determination method, vacuum saturation (Figure 10) does not produce as many petrophysical parameters as MICP. However, it has its advantages which MICP does not have: (1) It is efficient for a large sample size and volume: one round of vacuum saturation can test 30-40 core plugs or 240 pieces of $1cm^3$ cubes in 2 days, while MICP can only test 6-8 samples a day; (2) It is low cost: one round of vacuum saturation costs less than 20 dollars but one MICP analysis costs more than 100 dollars; (3) It allows a choice of wetting or non-wetting fluid to probe fluid-associated porosities.

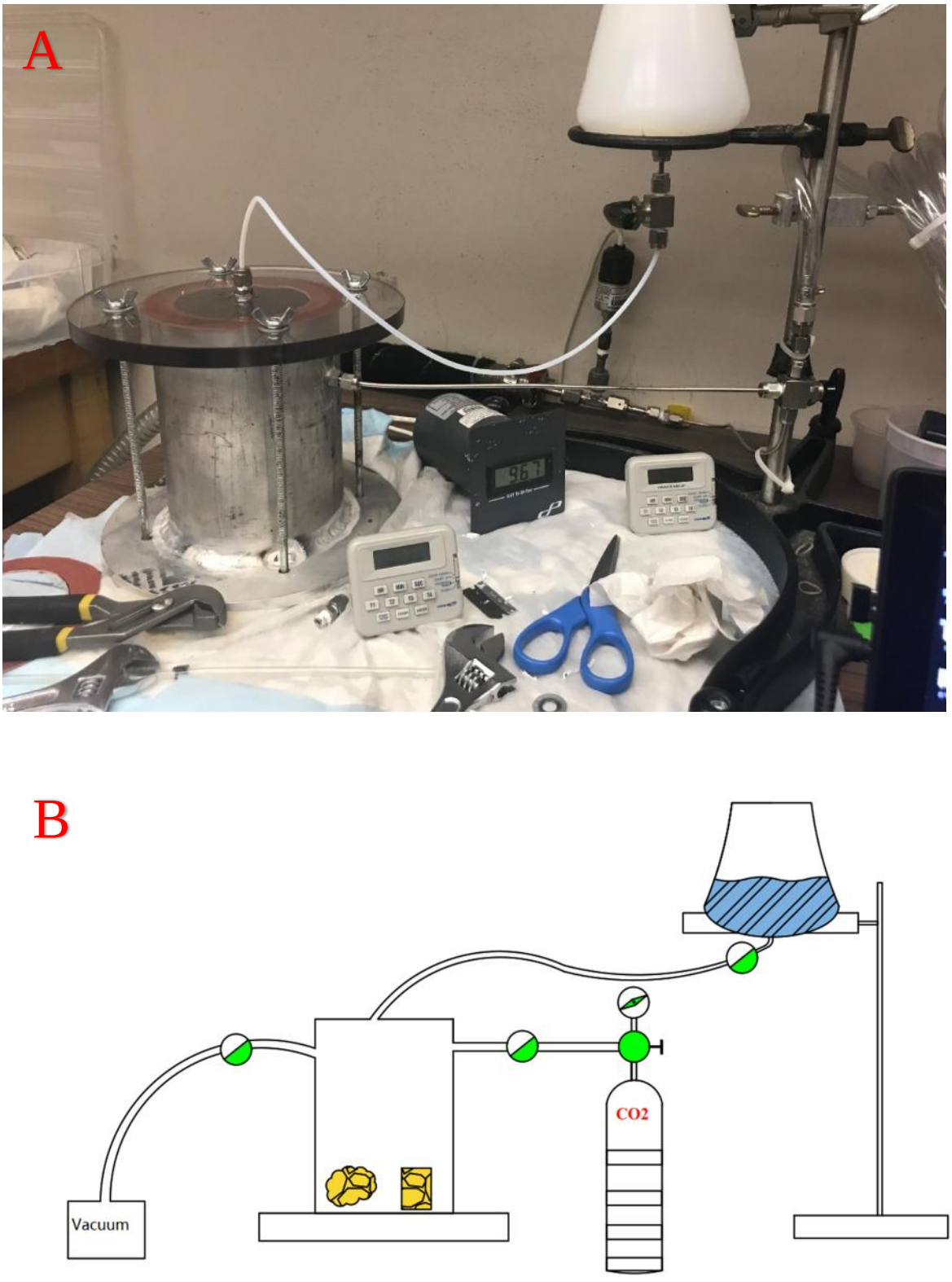

Figure 10. A) A photo and B) schematic diagram of vacuum saturation.

Combined with Archimedes' principle (Figure 11), vacuum saturation can measure porosity, bulk density and grain density of rock samples (American Petroleum Institute, 1998). The vacuum saturation set used in this study was custom designed by Dr. Hu's research group.

The equations used to calculate porosity, bulk density, and grain density are listed below.

$\varphi=V_o/V_b=(W_s-W_d)/W_f$

$\rho_b=V_o/W_d=(W_s-W_d)/\rho_f$

$\rho_g=\rho_b/(1-\varphi)$

where,

φ= porosity, no unit

V_o= void volume, cm^3

V_b= bulk volume, cm^3

W_s= sample weight with fluid saturation, g

W_d= sample over-dry weight, g

W_f= sample submerged weight in fluid, g

ρ_f= fluid density, g/cm^3

ρ_b= bulk density, g/cm^3

ρ_g= grain density, g/cm^3

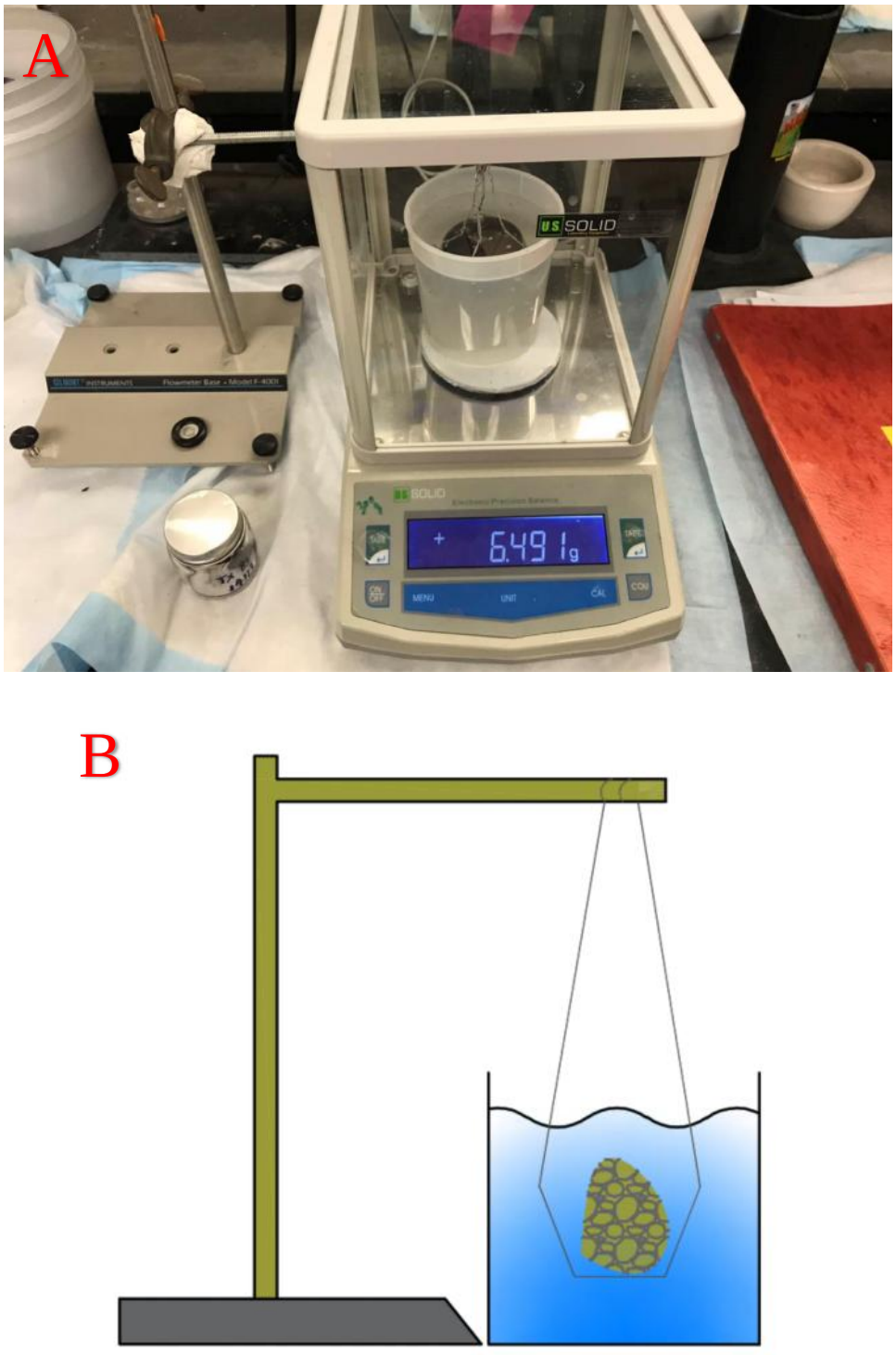

Figure 11. A) A photo and, B) schematic diagram of Archimedes' bucket.

3.5.2 The procedure of vacuum saturation

Samples were oven dried at 60 °C for 48 hours to remove moisture in connected pore spaces and taken out of the oven and placed into a desiccator for 30 minutes. Once the samples were cooled to room temperature, the oven-dry weight was measured. After weighing, for cylinder and irregular samples, they were directly placed into the vacuum chamber. For cubic samples, they were first put into the tray-holder and then placed into the vacuum chamber. After the chamber was properly sealed, the evacuation was started. The first evacuation process removed the air inside the sample for 6 to 8 hours, and the pressure in the chamber dropped to 0.06-0.1 torr (7.999-13.332 Pascal, or 99.99% vacuum). CO_2 was then allowed to enter into the chamber to replace air inside the sample, as CO_2 is more soluble in water than air. The second evacuation following the CO_2 flushing lasted for 12 to 18 hours. After finishing the second evacuation, a fluid (DI water) which invades the edge-accessible pore system was added to the vacuum chamber and 30 psi CO_2 pressure was applied to press water into the samples for 3 to 4 hours. Once the vacuum saturation was complete, samples were taken out of the vacuum chamber. Slightly DI water-moistened Kimwipes were used to wipe off the excess fluid on the sample surface and the saturated weight was recorded in air. Next, the samples were placed into the Archimedes' bucket to weigh the submerged weight. Finally, we used the equations to determine the porosity, bulk density, and grain density.

3.6 Mercury Intrusion Capillary Pressure (MICP)

3.6.1 Introduction of Mercury Intrusion Capillary Pressure analysis

MICP is widely used to analyze pore structure parameters (porosity, pore throat size, pore volume, pore throat size distribution, pore surface area, permeability, and tortuosity). A

Micromeritics AutoPore 9520 (Figure 12) was used to analyze cubic samples. The Washburn equation (Washburn, 1921) describes the relationship between pressure and radius of the capillary pore. The pressure conditions were set from 5 psi to 60,000 psi, which means that the detectable pore-throat diameter ranged from 45,000 to 2.8 nm.

Figure 12. Micromeritics AutoPore 9520.

3.6.2 Procedure of MICP analyses

Samples were oven dried at 60°C for 48 hours to remove the moisture and then placed into a desiccator to be cooled to room temperature. Next, we assembled a sample with a penetrometer and weighed the assembly mass. The penetrometer is an analyzer chamber connecting the sample with the MICP station. The penetrometer was covered with vacuum grease and inserted

into the low- pressure port, where it was evacuated to 50 µm Hg (0.05 torr, 6.666 pascals). Once the evacuation finishes, the penetrometer was filled with mercury to pressure at 5 psi. The low-pressure analysis used pressure ranges from 5 psi to 30 psi. During the analysis, when reaching each pressure point, the system stayed at each specified pressure for a short time (equilibrium time) to stabilize the volume reading and then increased or decreased to the next pressure point. For both low- and high-pressure analyses the equilibrium time was set to 30 seconds.

After low-pressure analysis, we weighed the penetrometer with the vacuum grease and small mercury drops were cleaned from its surface. Then the penetrometer was placed into the high-pressure port. During the high-pressure analysis, the pressure increased from 30 psi to 60,000 psi.

3.7 Contact Angle

3.7.1 Introduction of Contact Angle

The contact angle was first mentioned by Thomas (1804) as an angle created by liquid and solid surface interaction (Figure 13). In Kwok & Neumann (1999), contact angle measurement and interpretation were discussed in detail. In shale studies, a combination of contact angle and spontaneous imbibition is used to characterize the wettability related connectivity.

In this study, a SL200KB Optical Dynamic/ Static Interfacial Tensiometer & Contact Angle Meter (Figure 14) was used for contact angle measurement. DI water, API (American Petroleum Institute) brine, n-decane, and 10% isopropyl alcohol (IPA) were used to determine the contact angles of different fluids. The DI water represents hydrophilic fluid, and n-decane represents hydrophobic fluid. The 10% IPA is an example of amphiphilic fluid. The API brine is used to mimic fluid at the reservoir condition.

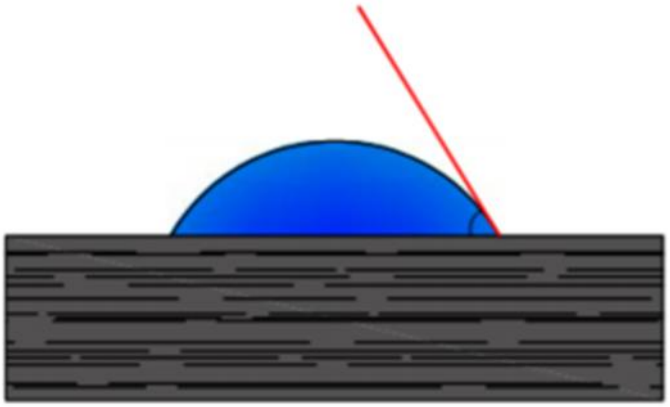

Figure 13. Illustration of contact angle.

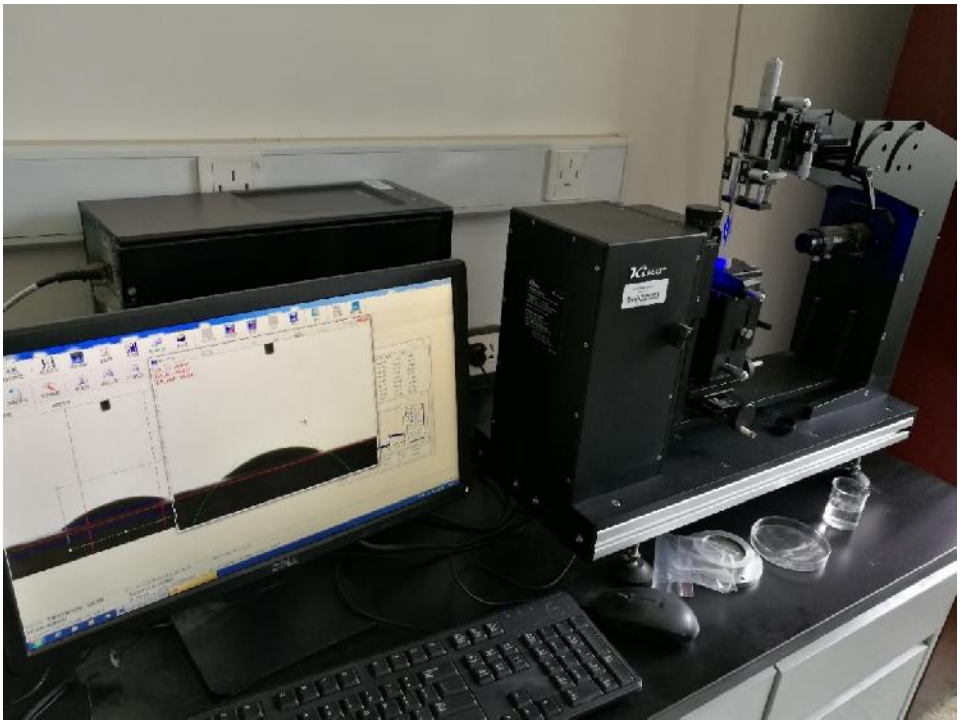

Figure 14. SL200KB Optical Dynamic/ Static Interfacial Tensiometer & Contact Angle Meter.

3.7.2 Procedure of Contact Angle

Oven-dried thin slabs of 1cm×1cm×0.3cm were used in this test. Thin slabs were first sanded or polished by sandpaper or polisher to reduce the roughness of the surface. For each test, one thin slab was placed on an adjustable platform. A droplet of a fluid was dropped onto the surface of a horizontal thin slab. The software was used to capture droplet behavior and generate contact angle data.

3.8 Spontaneous Fluid Imbibition

3.8.1 Introduction of Spontaneous Fluid imbibition

The spontaneous fluid imbibition was used to detect the behavior of fluid interaction with a rock. By conducting imbibition tests using different fluids, pore connectivity and wettability could be quantitatively assessed (Gao & Hu, 2016a, 2016b; Yang et al., 2017). Those studies reported that the amount of fluid one sample takes in is strongly related to the sample's wettability. To create different wettability analysis conditions, DI water was used as the hydrophilic fluid, and n-decane and toluene mixed solution (DT2, n-decane and toluene mixed at 2:1 by volume) was used as the hydrophobic fluid. The first-order driving force in this experiment is the capillary force, and the second-order driving force is diffusion and adsorption of vapor in the air (Kiepsch & Pelster, 2016). The first-order counter force of fluid imbibition is gravity. Handy (1960) claimed that the gravity effect should be negligible in coarse-textured rock.

In this study, we employed Handy's model:

$$Q_w^2=(2P_c k_w \varphi A_c 2S_w/\mu_w)t$$

Q_w: total volume of water imbibed in, cm^3

Pc: capillary pressure, Pa

K_w: the effective permeability of the porous medium to a wetting fluid, cm^2

A_c: imbibition cross-sectional area, cm^2

S_w: water saturation, %

μ_w: fluid viscosity, Pa*s

φ: sample porosity

t: imbibition time, s

3.8.2 Procedure of Spontaneous Fluid imbibition

For the fluid imbibition test, samples were cut into 1 cm^3 cubes. Except for the top and the bottom, all other surfaces were covered with quick cure epoxy. After being epoxied, samples were placed into the 60°C oven for 48 hours to remove the moisture. Then we took the samples out of the oven and immediately placed them into desiccator to be cooled to room temperature. Sample, holder, balance, and fluid dish were assembled as Figure 15 shows. The balance used was the Radwag AS 60/220.R2. Once the sample touched the surface, we started the balance's auto-recording software on the computer. For DI water, the test duration was set to 24 hours. For DT2, the test duration was set to be 6 hours considering its higher wettability onto shale and reduce the impact of its high evaporation rate.

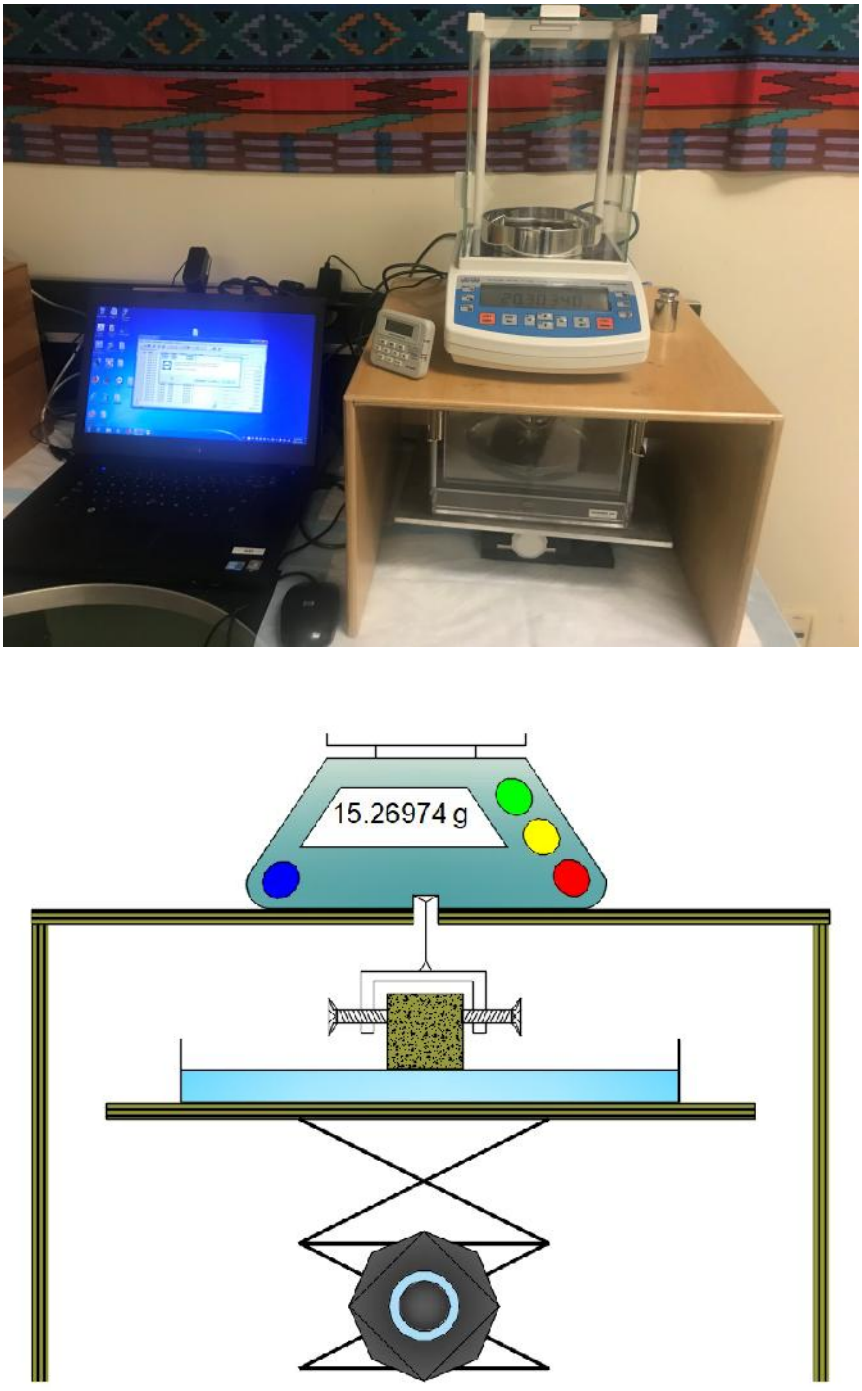

Figure 15. A) A photo and, B) Schematic diagram of imbibition set.

Chapter 4: Results

4.1 X-Ray diffraction

The mineral compositions of the Haynesville Shale samples in the study area shown in Table 5. In general, carbonates, quartz & feldspar, and clays are the three abundant mineral groups. Pyrite and ulvospinel only exist as a small amount. Carbonate composition takes 28.6% to 66.6 % of total weight percentage, quartz & feldspar account for 22.2% to 45.5%, and clay occupies 7% to 23.9%. To classify the Haynesville Shale, a shale classification ternary diagram, modified from Schlumberger (2014), was used. In this study, QFM (quartz, feldspar, and mica) group is replaced by the QF group while muscovite and illite assigned to the clay group because of their claylike sheet structure. The major mineral groups, QF (quartz and feldspar), clays (illite, kaolinite, chlorite, and muscovite), and carbonates (calcite and dolomite) are used to plot the ternary diagram (Figure 16). Also, considered as trace minerals, pyrite and ulvospinel are neglected in this diagram.

From the ternary diagram, most of the ten samples plot as mixed mudstone and carbonate/siliceous mudstone, with only three samples classified as mixed carbonate mudstone and silica-rich mudstone.

More detailed information such as clay mineral content distribution, quart & feldspar content distribution, and calcite vs. dolomite contents are clearly shown in a mineral composition pies diagrams (Figure 17 to 21).

Mineral Content (%) / Sample ID	Quartz	Albite	Anorthite	Microcline	Calcite	Dolomite	Illite	Montmorillonite	Clinochlore	Ulvospinel	Pyrite
BS 14359	24.2	5.0			24.9	21.7	17.5	0.8	1.5	1.4	3.1
BS 14374	33.1	2.9	2.1		29.4	2.4	22.4	0.6	0.9	2.3	3.9
BS 14395	38.3	0.9	1.0	4.3	22.9	10.5	15.2	1.0	0.5	1.8	3.5
BS 14404	40.3	3.7	1.5		24.6	4.0	17.7	0.2	0.5	3.1	4.5
BS 14411	18.7	3.5			65.2	1.4	7.0		0.3	1.1	2.8
BS 14427	24.7	5.6			42.6	1.3	19.5	0.5	0.3	2.1	3.4
BS 14433	23.3	3.0			60.2	1.2	8.0	0.6	0.3	1.1	2.1
BS 14446	34.8	3.8	1.3		31.0	2.1	19.4	0.6	0.3	2.8	4.0
BS 14462	34.6	1.8	1.2		40.6	2.1	14.0	0.9	0.6	0.9	3.3
BS 14482	25.1	2.7	1.0		48.3		14.4	1.0	0.4	1.5	5.6

Table 5. Mineral composition of each sample (wt.%).

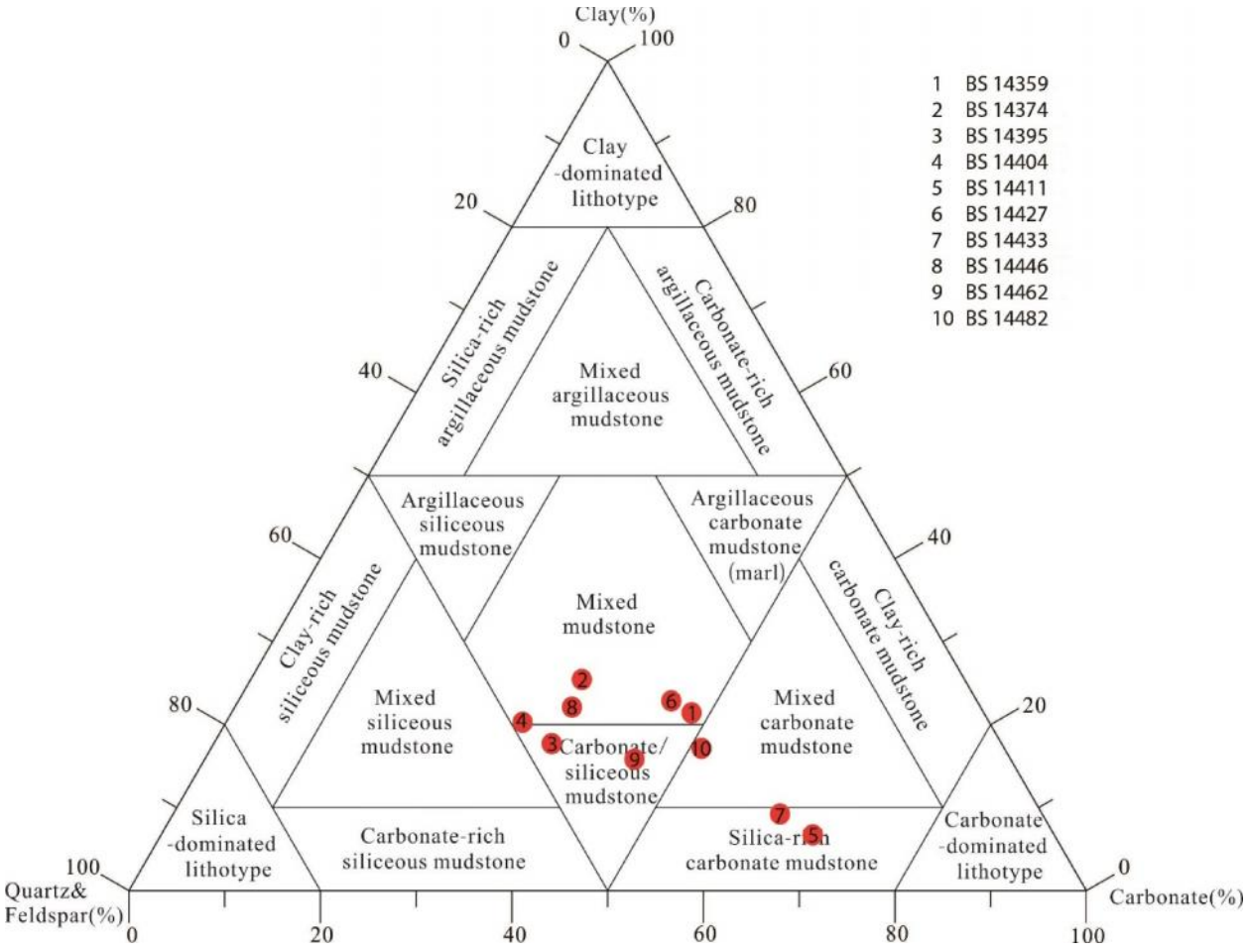

Figure 16.. Ternary shale classification diagram with the Haynesville samples plotted on (modified from Schlumberger, 2014).

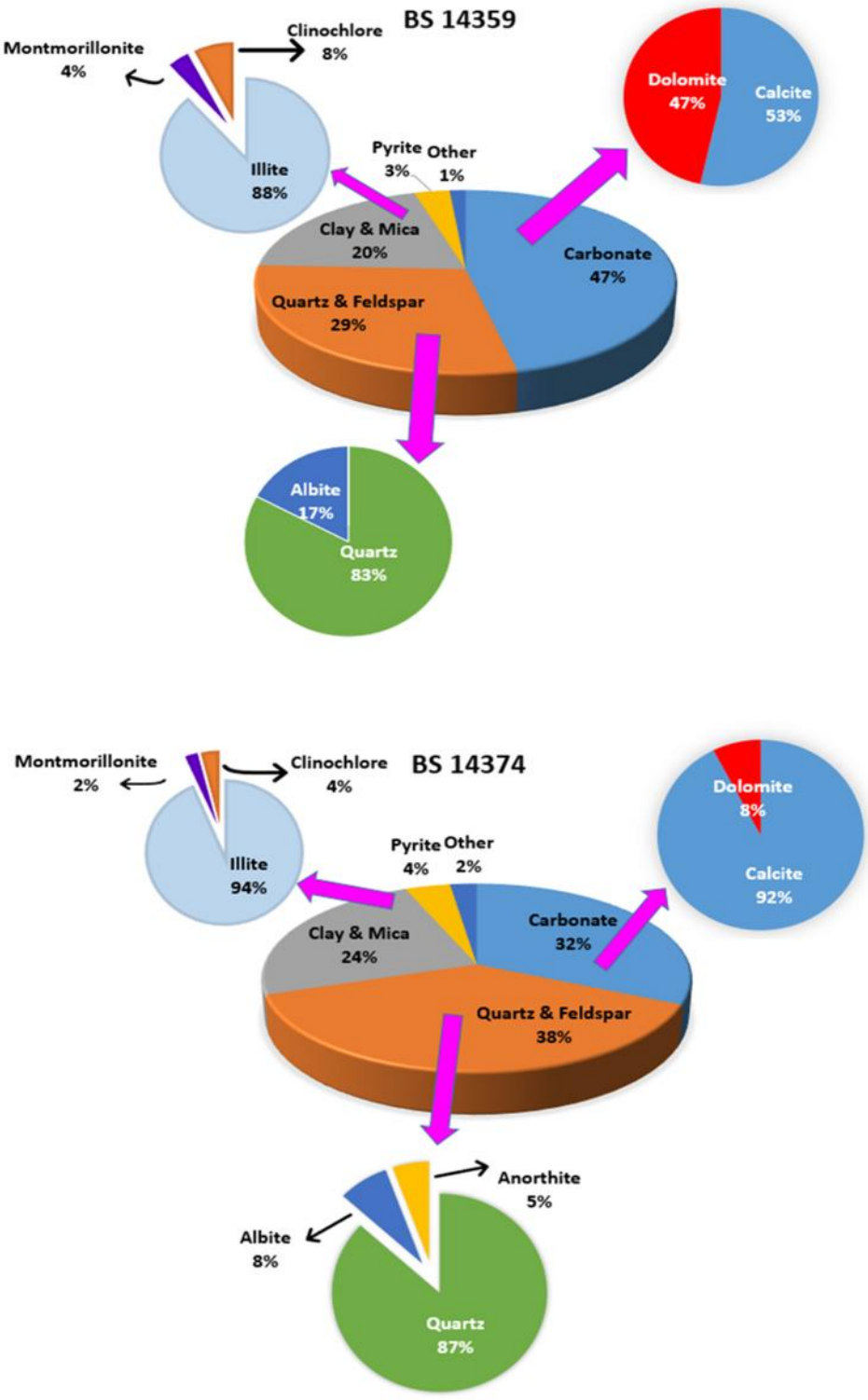

Figure 17. Pie chart of mineral composition: BS 14359 (top) and BS 14374 (bottom).

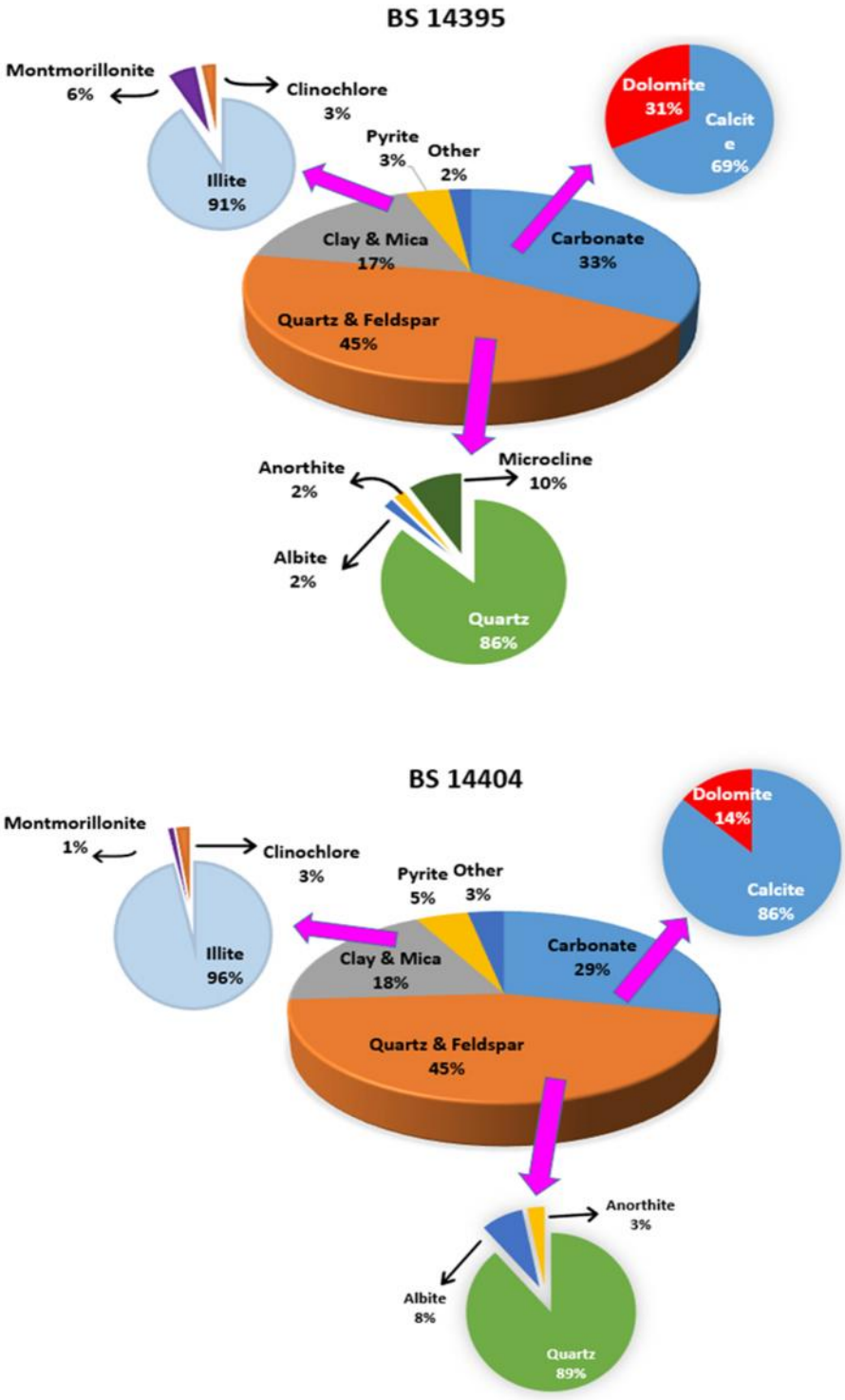

Figure 18. Pie chart of mineral composition: BS 14395 (top) and BS 14404 (bottom).

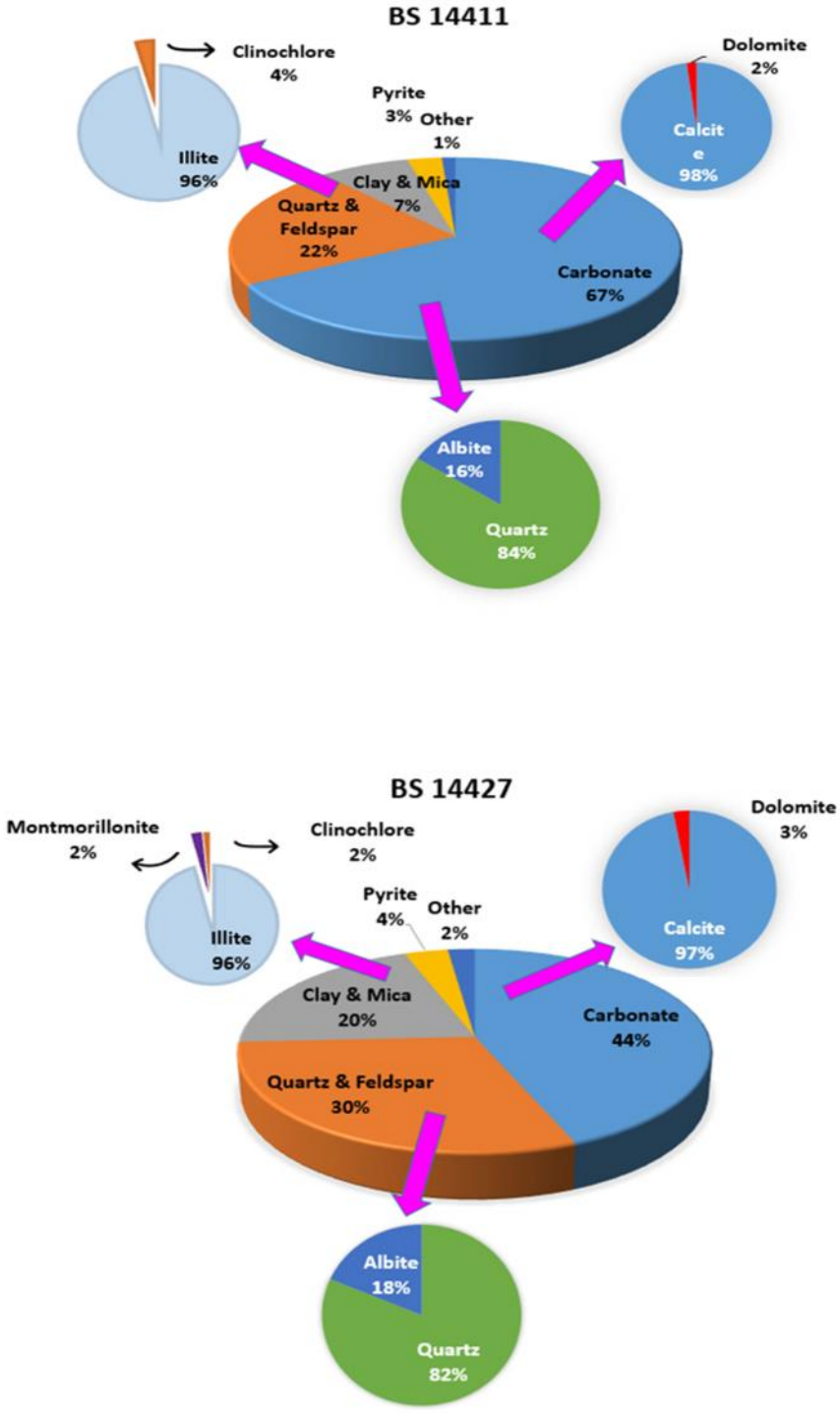

Figure 19. Pie chart of mineral composition. BS 14411 (top) and BS 14427 (bottom).

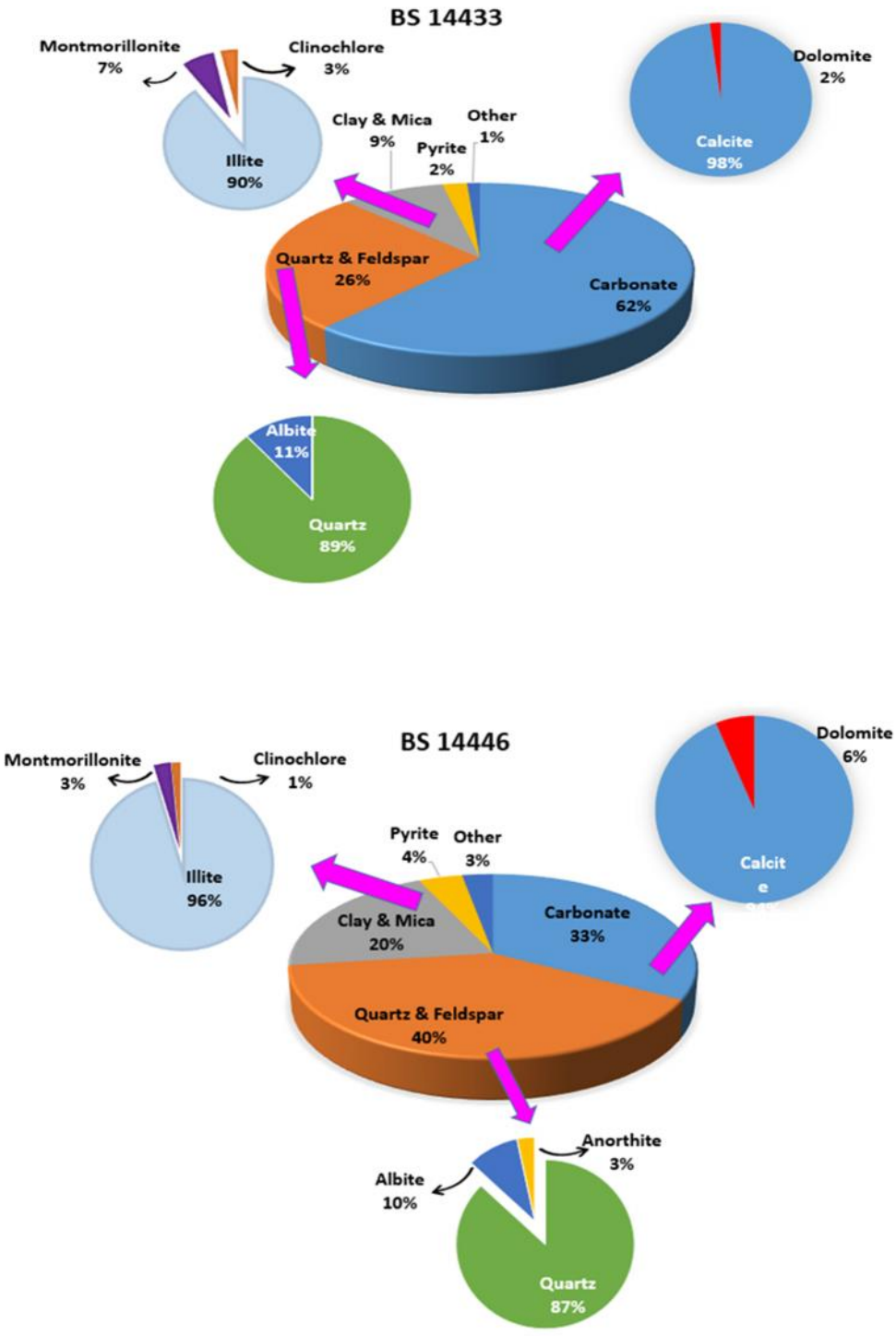

Figure 20. Pie chart of mineral composition. BS 14433 (top) and BS 14446 (bottom).

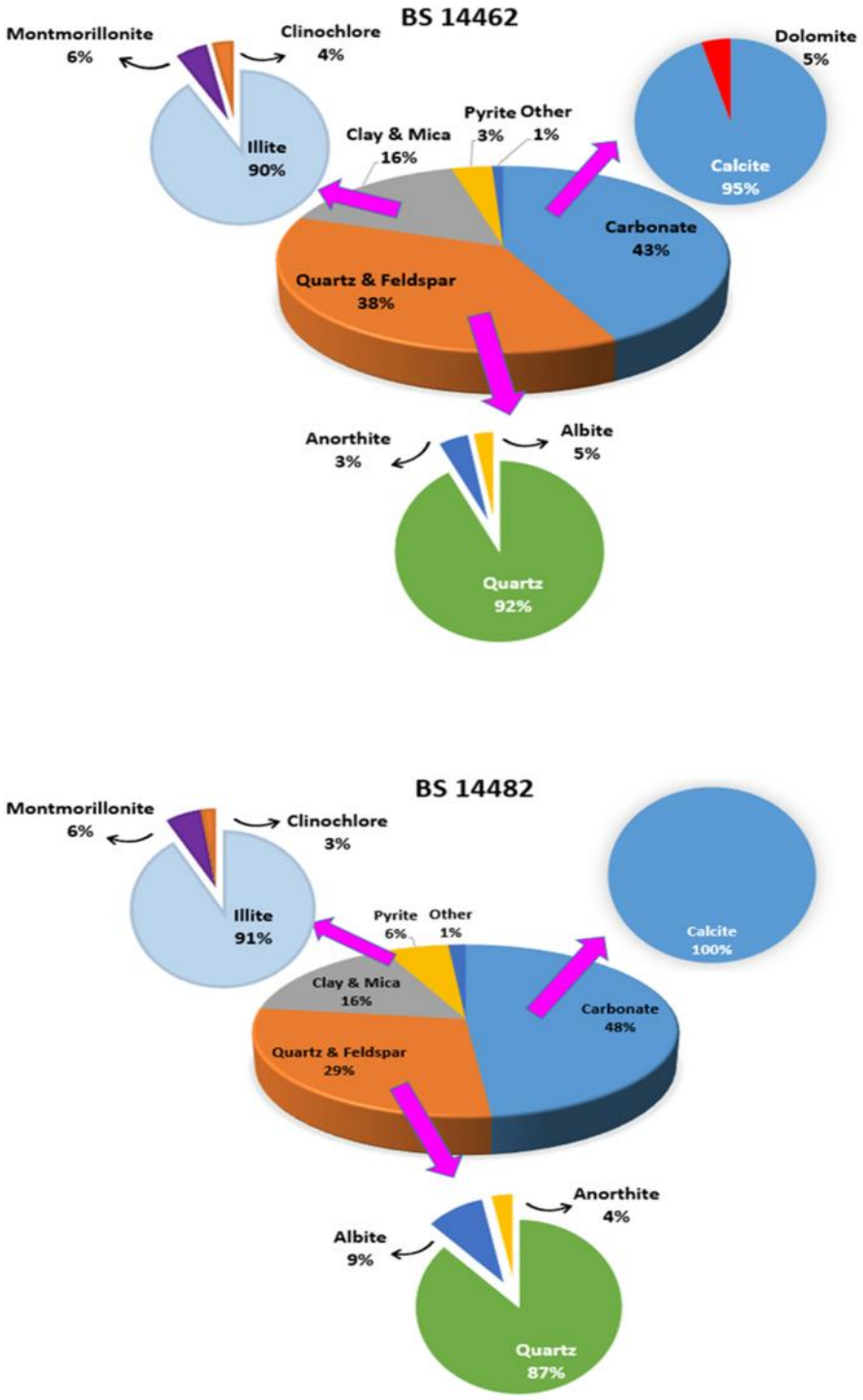

Figure 21. Pie chart of mineral composition. BS 14462 (top) and BS 14482 (bottom).

4.2 Pyrolysis and TOC

Rapid CS Cube generated TOC values were obtained in this study (Figure 22). TOC values generated from pyrolysis are used as a reference group (Table 6). Two issues made the results obtained from the two methods differ. (1) The maximum of the pyrolysis is 600 C°, whereas the temperature of TOC analysis is 1200 C°. The lower temperature in the pyrolysis led some of the organic matters to remain uncombusted. (2) The samples used in pyrolysis were not aicd-washed. The existing of inorganic carbon influenced the final results. Pyrolysis results are shown in Table 6. In this programmed pyrolysis analysis using the OGE-V Oil and Gas Evaluation Station, S3 values were not recorded. For calculated indexes, only the production index (PI) was used in this analysis.

The Haynesville Shale, which has been well-known as an organic-rich shale gas play, has a high maturity and high TOC percentage. The TOC vs. depth trend (Figure 22) shows that the TOC increases with depth by a factor of 2. The Haynesville Shale has the properties of being a good hydrocarbon reservoir such as high TOC content (2.26 to 5.28 %), high S1 values (1.51 to 3.22 mg/g). However, the S2 values, which represent CO_2 signal generated from the cracking of kerogen, range from 0.68 to 1 mg/g. The very low S2 value led to Tmax values unreliable. High S1 values and low S2 values generate high PI. PI reflects the degree of maturity of source rock. The high PI value indicates Haynesville Shale is over-mature and has low hydrocarbon generation potential.

Sample ID	TOC (%)	T_{max} ( )	S1 (mg/g)	S2 (mg/g)	S1+S2 (mg/g)	P I (S1/(S1+S2))
BS 14359	1.97	400.1	1.55	0.73	2.28	0.68
BS 14374	1.97	381.7	3.06	0.48	3.54	0.86
BS 14395	2.48	351.9	2.86	0.81	3.67	0.78
BS 14404	4.54	386.0	3.22	0.97	4.19	0.77
BS 14411	3.23	N/A	1.51	0	1.51	1.00
BS 14427	5.70	371.1	2.63	0.41	3.04	0.87
BS 14433	4.09	371.0	1.58	0.13	1.71	0.92
BS 14446	5.75	365.5	2.27	0.34	2.61	0.87
BS 14462	4.54	386.0	2.16	0.92	3.08	0.70
BS 14482	6.40	358.0	2.57	0.65	3.22	0.80

Table 6. Summary of pyrolysis data.

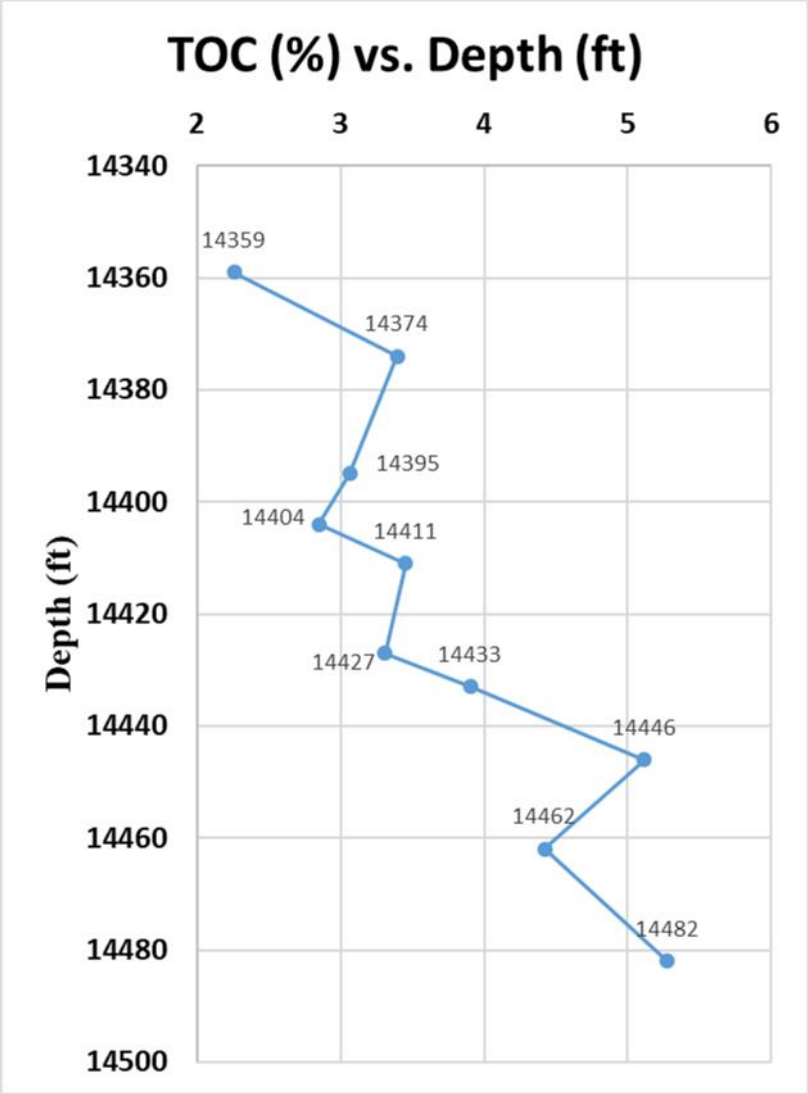

Sample ID	TOC (%)
BS 14359	2.26
BS 14374	3.39
BS 14395	3.07
BS 14404	2.85
BS 14411	3.45
BS 14427	3.31
BS 14433	3.91
BS 14446	5.12
BS 14462	4.42
BS 14482	5.28

Figure 22. Plot of TOC (%) with depth (ft). TOC data from Rapid CS Cube TOC analyses.

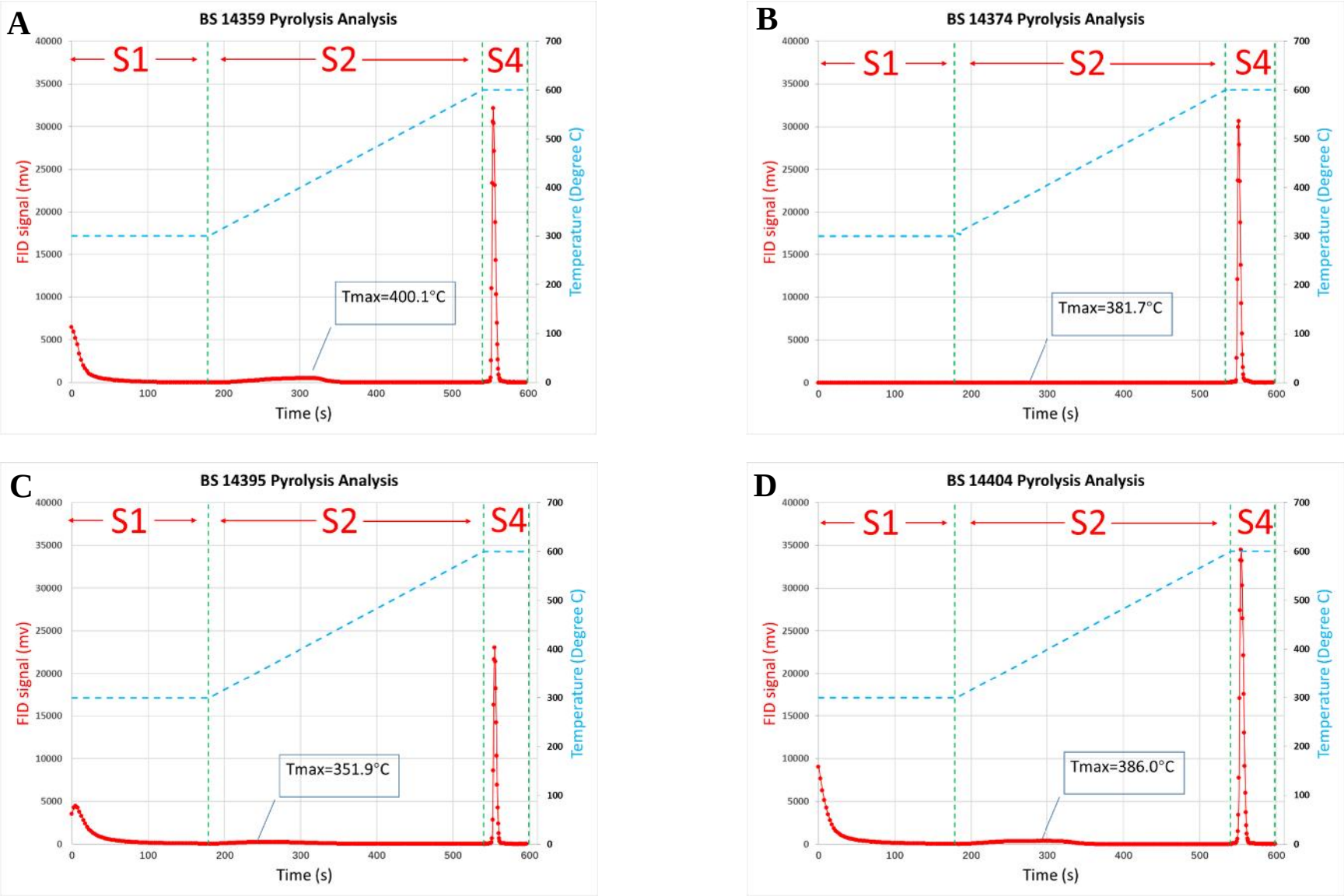

Figure 23. Pyrolysis plot: A) BS 14359, B) BS 14374, C) BS 14395, D) BS 14404.

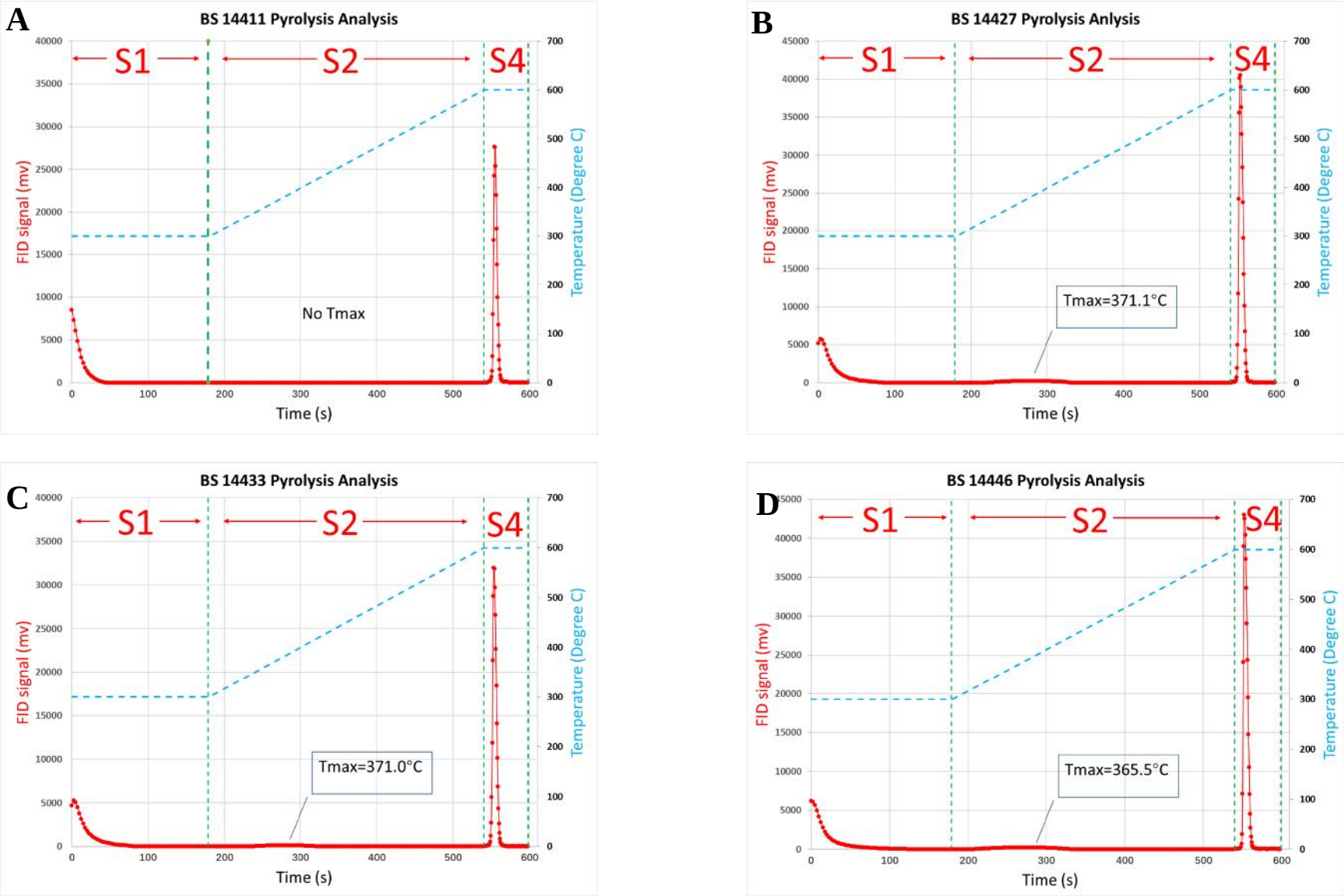

Figure 24. Pyrolysis plot. A) BS 14411, B) BS 14427, C) BS 14433, D) BS 14446.

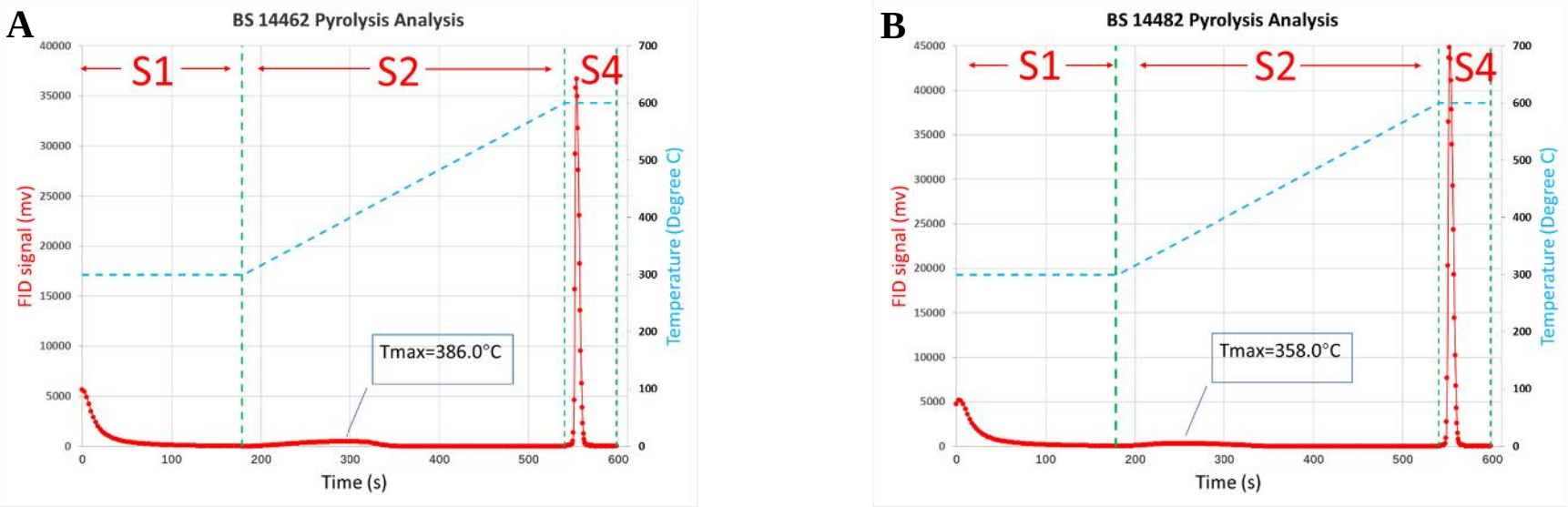

Figure 25. Pyrolysis plot. A) BS 14462, B) BS 14482.

4.3 Vacuum saturation

Our vacuum saturation set allows 240 cubic samples to be ran at the same time. In other words, it can measure porosities of 240 samples in 3 days. In this test, to reduce the sample selection bias, we selected four cubes from each sample to assess the influence of heterogeneity. Moreover, DI water (run on 4 samples), as well as DT2 and tetrahydrofuran (THF) (both run on one sample) were used to verify the impact of wettability on measured porosities. DI water edge-accessible porosities of Haynesville Shale range from 2.626±0.25 % to 6.631±0.890 %. DT2 edge-accessible porosities range from 3.14% to 7.74%. THF edge-accessible porosities range from 3.319 to 10.422%. The significant wettability of each fluid may lead to large variation of porosities. Comparing with DI water edge-accessible porosities, the DT2 porosities do not show an obvious increasing or decreasing trend. During the experiments, the higher evaporation rate of THF has been noticed to affect the measurement. Unlike the negligible evaporation rates of DI water and DT2 in vacuum saturation experiments, the higher evaporation rate of THF from both fluid-saturated samples and Archimedes' bucket tend to result in a large variation of porosities.

	Sample size	DI water						DT2 (mixture of 2 n-decane + 1 toluene)			Tetrahydrofuran		
		Porosity (%)	Average porosity (%)	Bulk density (g/cm^3)	Average Bulk density(g/cm^3)	Grain density (g/cm^3)	Average Grain density(g/cm^3)	Porosity (%)	Bulk density (g/cm^3)	Grain density (g/cm^3)	Porosity (%)	Bulk density (g/cm^3)	Grain density (g/cm^3)
BS 14359	Cube A	6.435	6.026±1.238	2.457	2.497±0.026	2.636	2.657±0.019				7.678	2.555	2.767
	Cube B	7.244		2.480		2.674							
	Cube C	3.957		2.535		2.640							
	Cube D	6.457		2.505		2.678		7.774	2.578	2.795			
BS 14374	Cube A	7.034	5.841±0.855	2.391	2.394±0.002	2.572	2.543±0.021						
	Cube B	5.075		2.397		2.525							
	Cube C	N/A		N/A		N/A					7.910	2.442	2.652
	Cube D	5.414		2.394		2.531		7.490	2.459	2.658			
BS 14395	Cube A	2.548	2.929±0.367	2.451	2.447±0.027	2.515	2.521±0.036						
	Cube B	2.804		2.432		2.503							
	Cube C	2.826		2.416		2.486					3.319	2.557	2.645
	Cube D	3.535		2.490		2.581							
BS 14404	Cube A	5.080	5.946±1.496	2.360	2.354±0.015	2.486	2.503±0.024						
	Cube B	6.583		2.345		2.510							
	Cube C	8.030		2.336		2.540					8.625	2.429	2.658
	Cube D	4.090		2.375		2.476		5.527	2.419	2.561			
BS 14411	Cube A	2.607	2.626±0.525	2.454	2.461±0.011	2.520	2.528±0.008						
	Cube B	2.054		2.479		2.531							
	Cube C	2.374		2.461		2.521					3.548	2.558	2.652
	Cube D	3.469		2.451		2.539		3.140	2.506	2.588			
BS 14427	Cube A	7.432	6.631±0.890	2.329	2.33±0.014	2.516	2.496±0.021						
	Cube B	7.352		2.330		2.515					1.175	2.427	2.456
	Cube C	5.218		2.348		2.477							
	Cube D	6.523		2.309		2.470		5.543	2.375	2.514			
BS 14433	Cube A	5.719	4.751±0.581	2.416	2.454±0.042	2.563	2.576±0.04						
	Cube B	4.585		2.523		2.644					6.254	2.540	2.709
	Cube C	4.172		2.452		2.559							
	Cube D	4.526		2.425		2.540		3.778	2.486	2.583			
BS 14446	Cube A	6.792	6.173±0.768	2.366	2.366±0.002	2.538	2.522±0.019						
	Cube B	5.657		2.368		2.510							
	Cube C	7.041		2.363		2.542					10.422	2.352	2.626
	Cube D	5.190		2.367		2.497		5.309	2.390	2.524			
BS 14462	Cube A	4.955	5.289±0.380	2.404	2.402±0.004	2.530	2.536±0.011						
	Cube B	5.646		2.396		2.539					6.073	2.480	2.641
	Cube C	5.690		2.408		2.553							
	Cube D	4.865		2.400		2.523		4.140	2.455	2.561			
BS 14482	Cube A	6.000	5.156±0.624	2.424	2.434±0.018	2.579	2.566±0.016						
	Cube B	5.084		2.453		2.584					6.624	2.526	2.706
	Cube C	4.250		2.448		2.557							
	Cube D	5.291		2.410		2.545		6.918	2.461	2.644			

Table 7. Vacuum saturation data of employing DI water, DT2, and THF fluids.

4.4 Mercury Intrusion Capillary Pressure

Mercury intrusion capillary pressure is one of the core experiments in this research. The MICP test can generate bulk density, grain density, total pore area, porosity, permeability, tortuosity, and pore-throat size distribution. In this study, porosity, pore-throat size distribution, permeability, and tortuosity are used as key parameters and the rest of the parameters are used for comparison with the results obtained from other methods. The porosity of the Haynesville Shale measured from MICP ranges from 2.8% to 7.3%. Permeability varies from 4 to 23 nano-darcy (nD). Effective tortuosity has a minimum value of 1413 and a maximum value of 3433m, whereas the geometrical tortuosity various from 8 to 12.

Sample ID	Bulk density (g/cm^3)	Apparent Grain density (g/cm^3)	Total Pore area (m^2/g)	Porosity (%)	Permeability (nD)	Effective tortuosity	Geometrical tortuosity
BS 14359	2.4171	2.6078	12.087	7.313	23.4	1580	10.748
BS 14374	2.4394	2.596	16.293	6.0342	13.1	1914	10.746
BS 14395	2.4818	2.5542	6.14	2.8373	7.9	3433	9.87
BS 14404	2.3805	2.4982	13.557	4.7119	4.8	3296	12.461
BS 14411	2.4536	2.5318	9.06	3.0905	3.7	2011	7.884
BS 14427	2.3437	2.5043	18.052	6.4127	6.5	1879	10.977
BS 14433	2.4584	2.5717	13.005	4.4062	4.0	1753	8.788
BS 14446	2.3824	2.5222	15.243	5.5404	6.4	2570	11.932
BS 14462	2.4225	2.5559	15.514	5.2166	4.7	2751	11.979
BS 14482	2.4776	2.5875	10.817	4.2453	5.9	1413	8.586

Table 8. Summary of MICP results.

A plot of intrusion pressure vs. Log differential intrusion (Figure 26 to Figure 35, plot A) illustrates various pore system in the shale sample. Gao and Hu (2013) introduced how to divide different pore systems by picking up inflection points. Each inflection point, representing a connected pore network, is used to calculate the permeability and tortuosity of each pore system. Another plot of pore-throat diameter vs. incremental pore volume (Figure 26 to Figure 35, plot C) shows the mercury intrusion volume at each pressure point, which was then converted to

pore-throat diameter; as a result, it gives a continuous picture of the mercury intrusion process. To understand the pore-throat diameter distribution and pore volume, the pore systems are divided into five groups based on pore-throat diameter, which are related to dominant pore types (Table 9). Overall, the pore-throat sizes of Haynesville Shale are concentrated from 2.8 to 50 nm. All the samples are rich in organic pores and intragranular pores. Most samples contain a large amount of inter-clay platelet pores, whereas the BS 14359 only contains a very small amount. Intergranular pores, micro-fractures, and laminations are not predominant pore types. However, microfracture or lamination occupies a considerable percentage in samples BS 14359 (17.6 %) and BS 14395 (23.5 %).

Pore-throat size (μm) / Sample ID	0.0028-0.005	0.005-0.01	0.01-0.05	0.05-1	1-50
BS 14359	0.6	44.4	25.3	12.0	17.6
BS 14374	30.1	35.4	20.2	4.4	9.8
BS 14395	27.4	22.8	18.8	7.4	23.6
BS 14404	35.9	30.8	15.8	6.2	11.3
BS 14411	35.2	36.8	15.6	5.6	6.7
BS 14427	29.8	35.7	20.5	6.5	7.4
BS 14433	36.0	36.3	16.5	4.5	6.6
BS 14446	29.9	36.1	17.6	6.3	10.0
BS 14462	34.1	39.4	14.9	4.0	7.7
BS 14482	26.3	37.1	21.8	6.4	8.4

Table 9. Pore throat size vs. pore distribution in percentage.

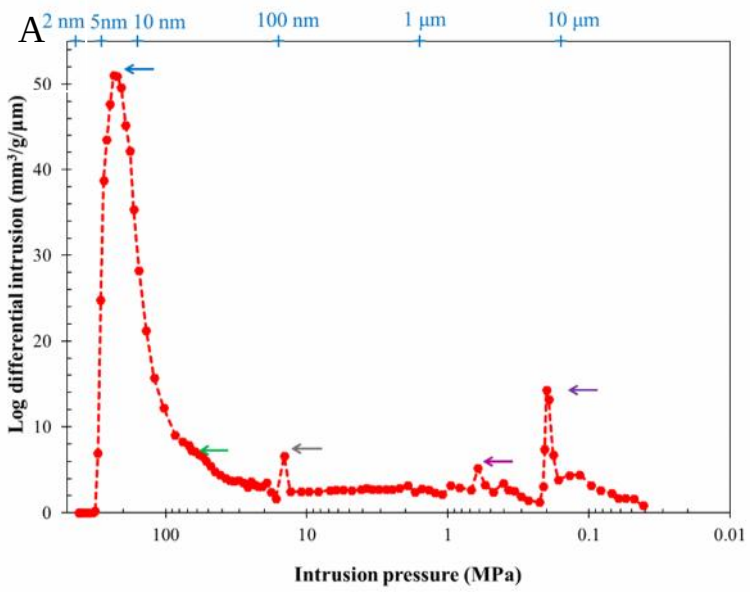

Figure 26. MICP plots of BS 14359: A) Inflection points shown with arrows; B) Pore volume vs. pore-throat diameter; C) Incremental pore volume vs. pore-throat diameter.

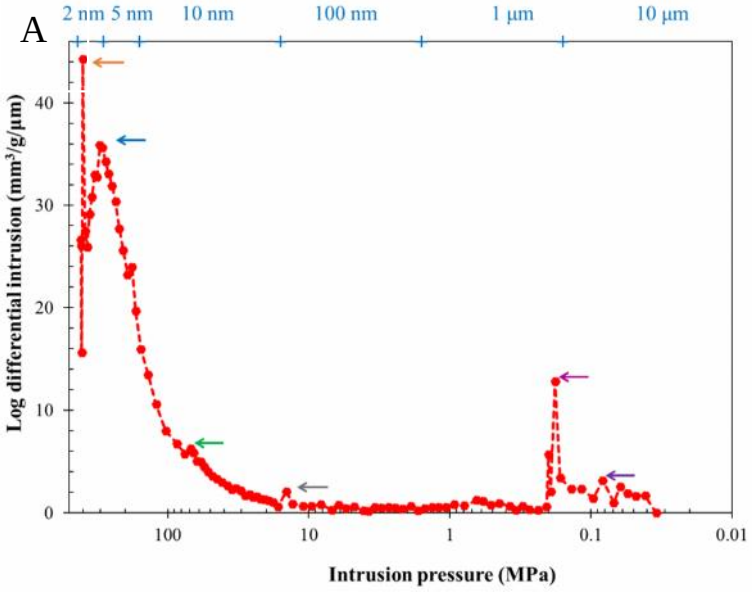

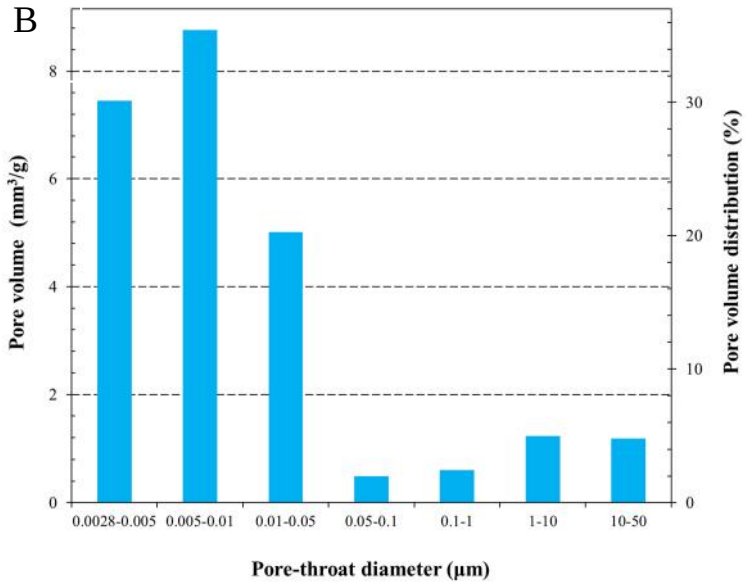

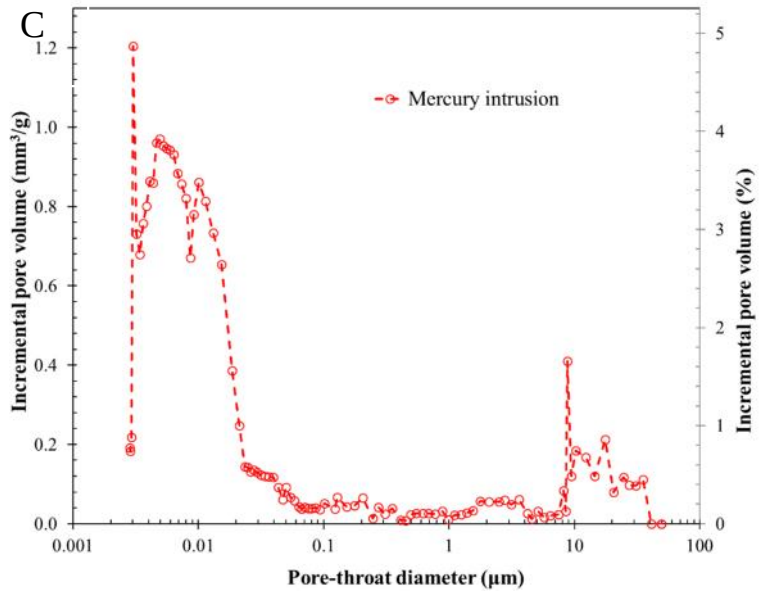

Figure 27. MICP plots of BS 14374: A) Inflection points shown with arrows; B) Pore volume vs. pore-throat diameter; C) Incremental pore volume vs. pore-throat diameter.

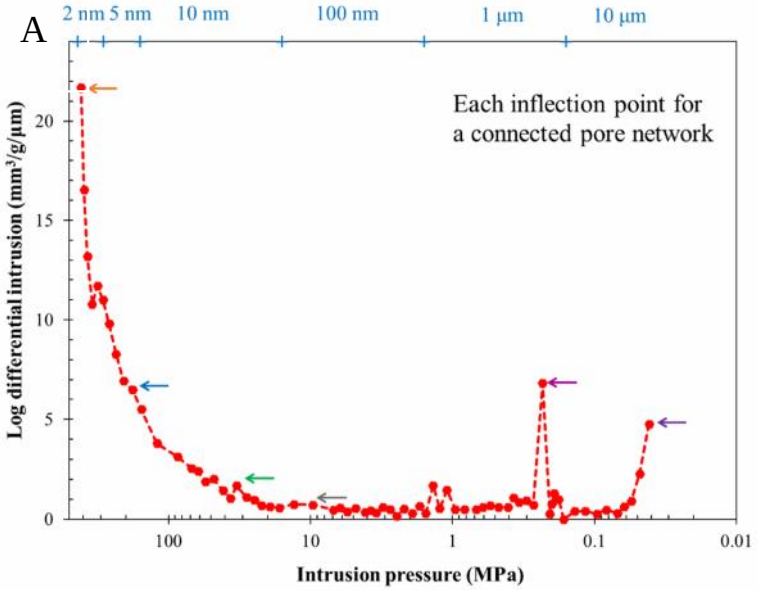

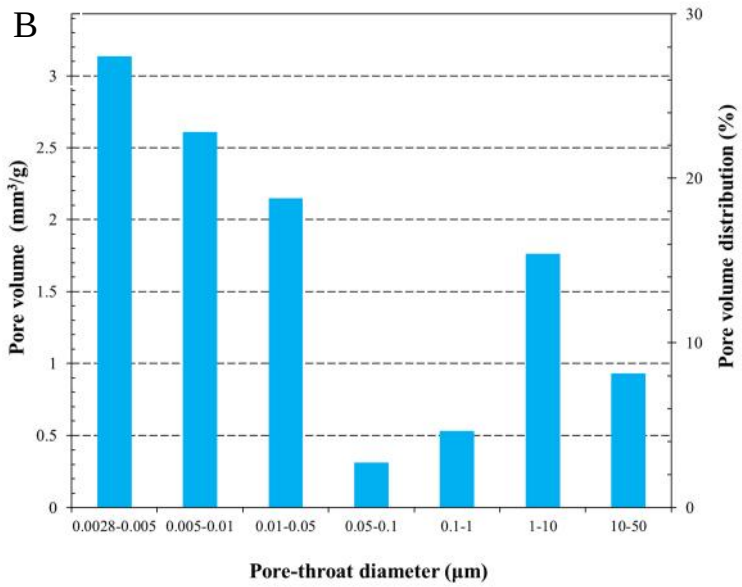

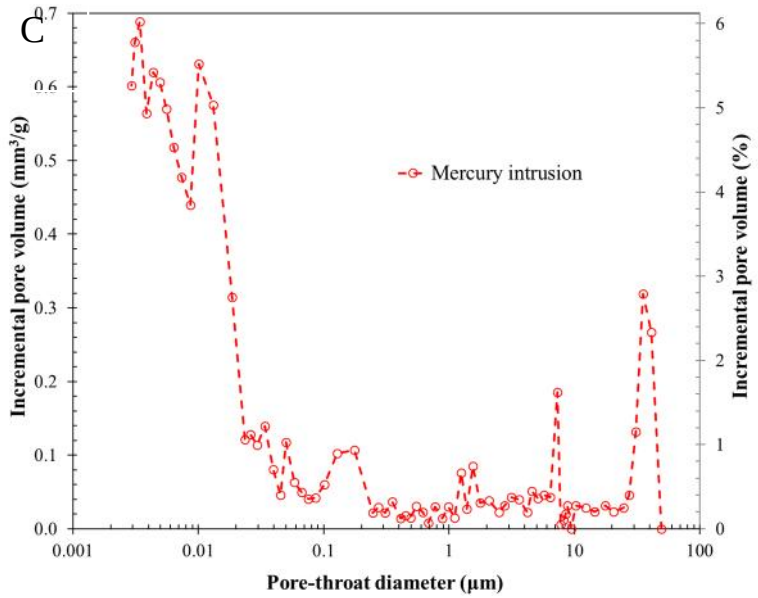

Figure 28. MICP plots of BS 14395: A) Inflection points shown with arrows; B) Pore volume vs. pore-throat diameter; C) Incremental pore volume vs. pore-throat diameter.

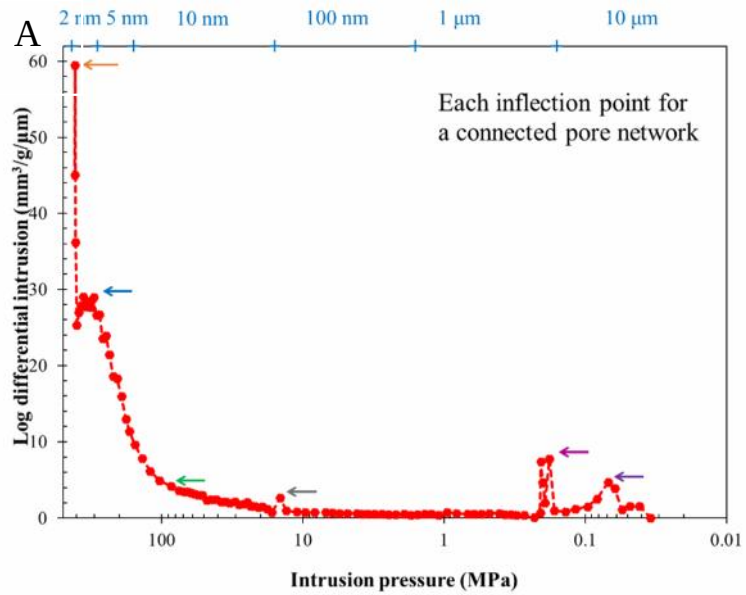

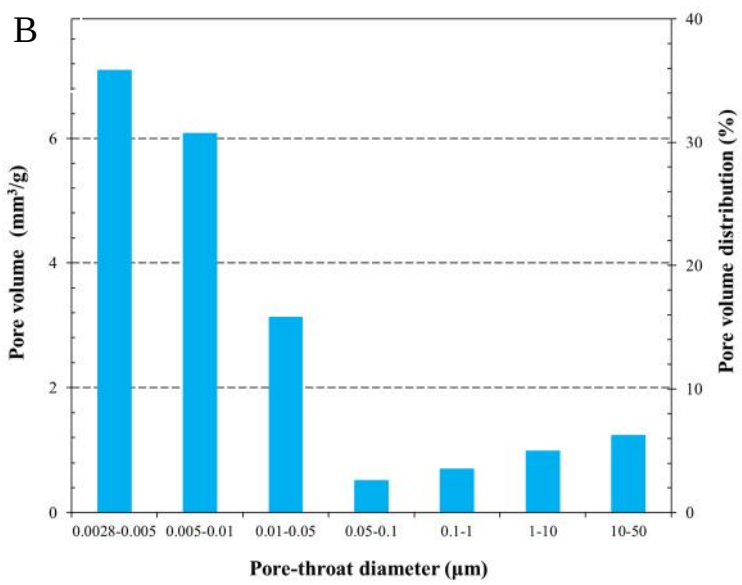

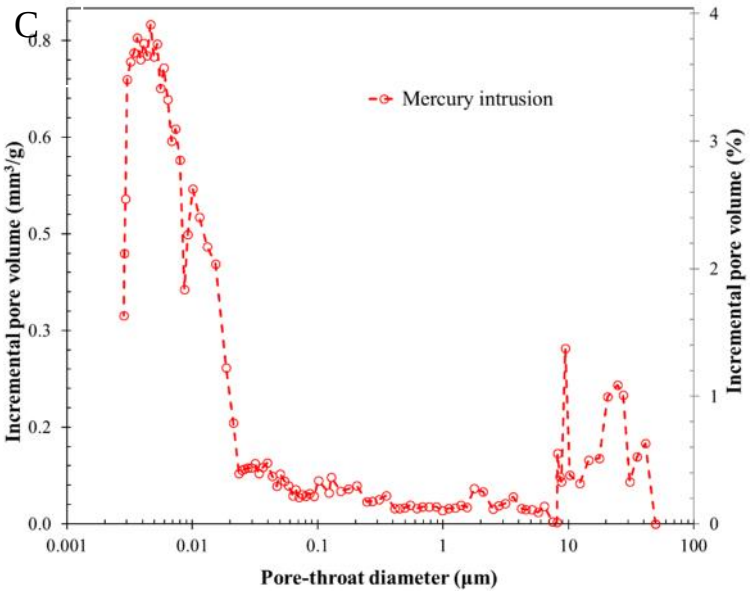

Figure 29. MICP plots of BS 14404: A) Inflection points shown with arrows; B) Pore volume vs. pore-throat diameter; C) Incremental pore volume vs. pore-throat diameter.

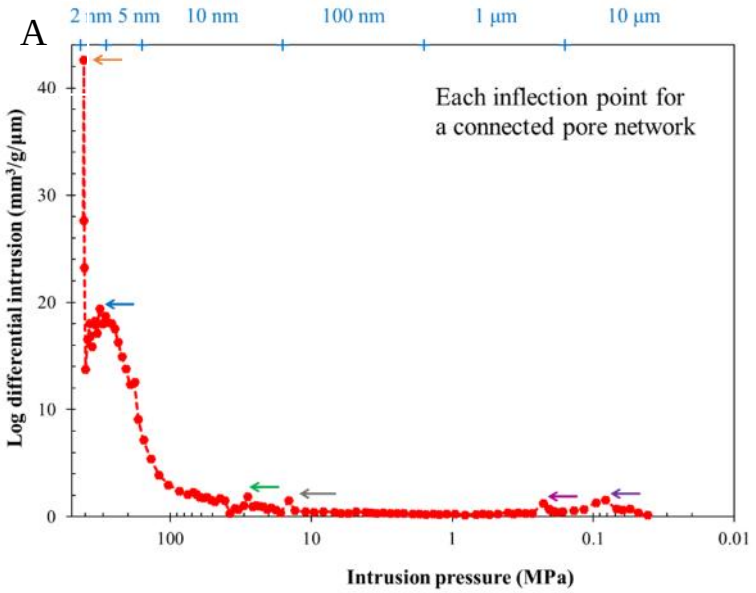

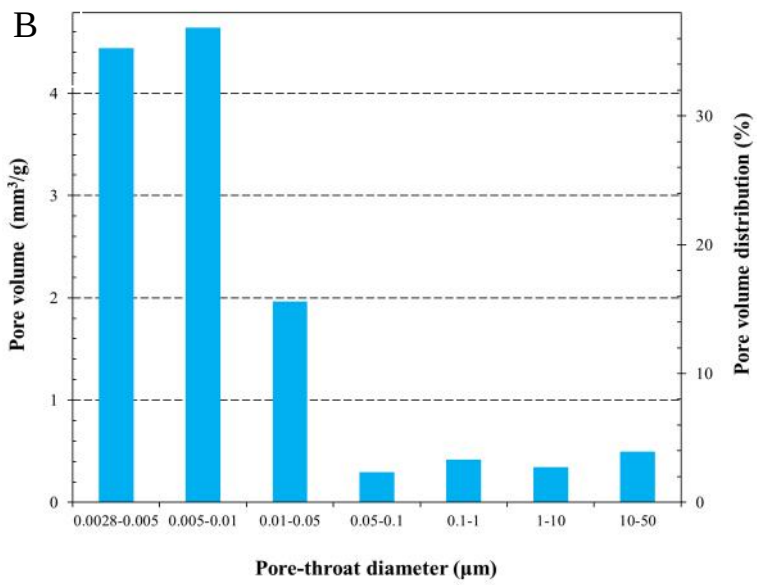

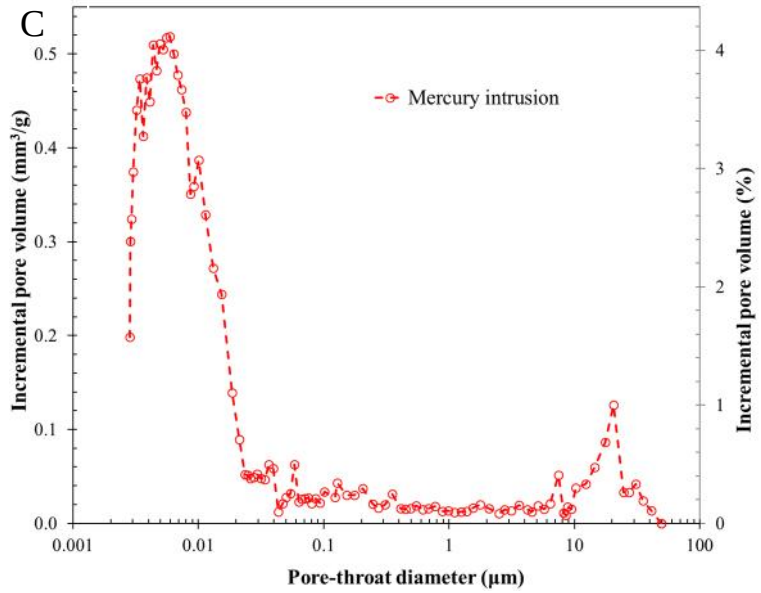

Figure 30. MICP plots of BS 14411: A) Inflection points shown with arrows; B) Pore volume vs. pore-throat diameter; C) Incremental pore volume vs. pore-throat diameter.

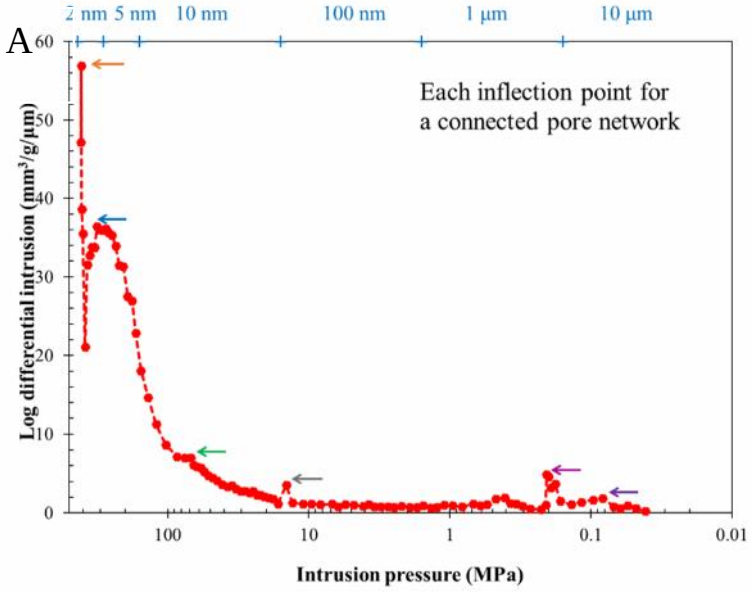

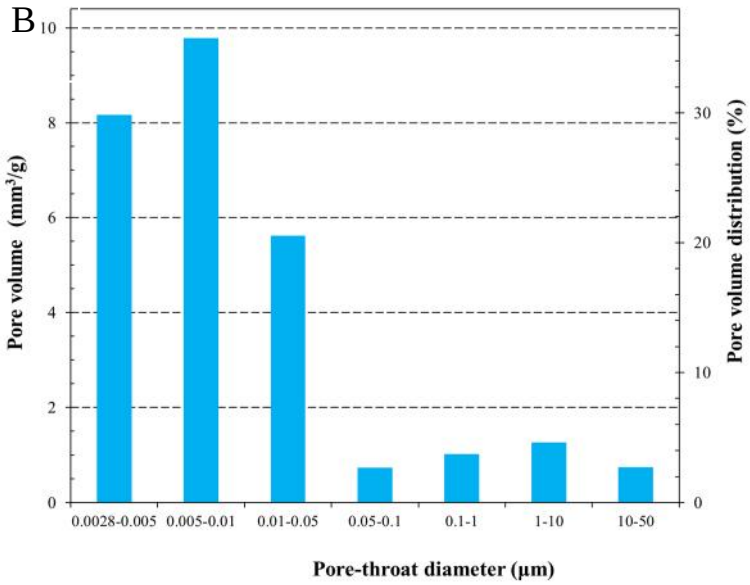

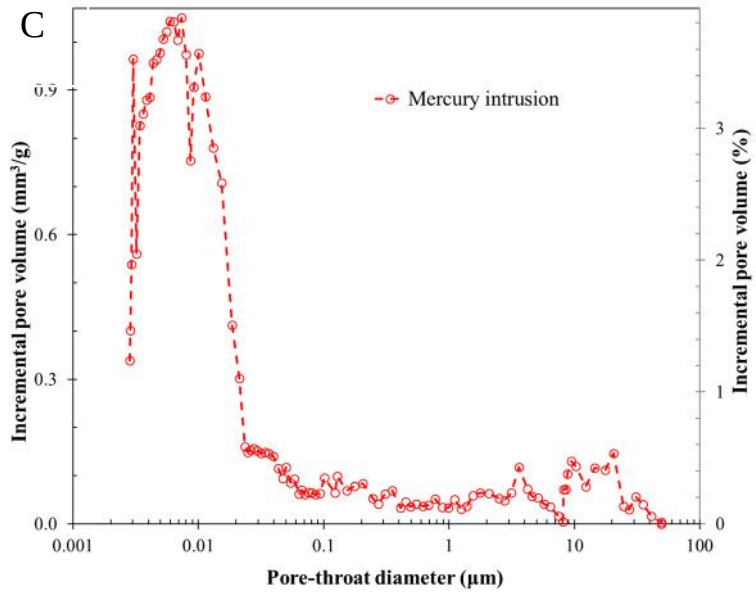

Figure 31. MICP plots of BS 14427-H: A) Inflection points shown with arrows; B) Pore volume vs. pore-throat diameter; C) Incremental pore volume vs. pore-throat diameter.

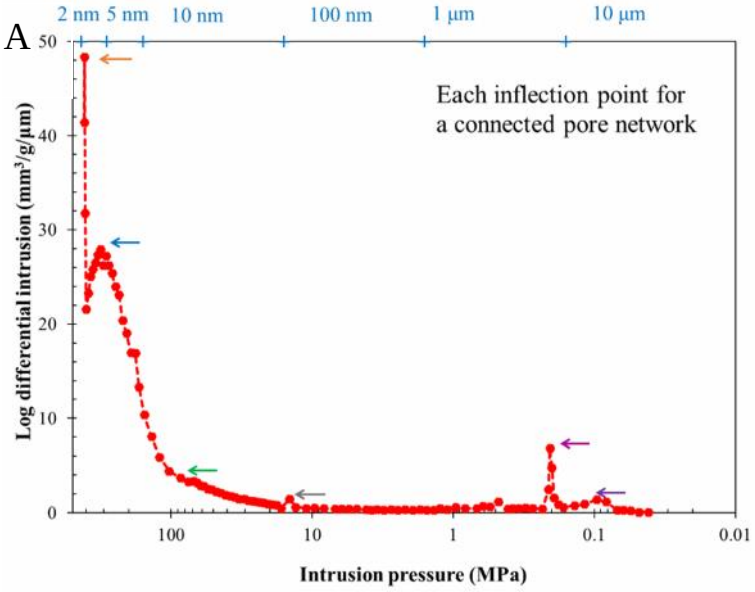

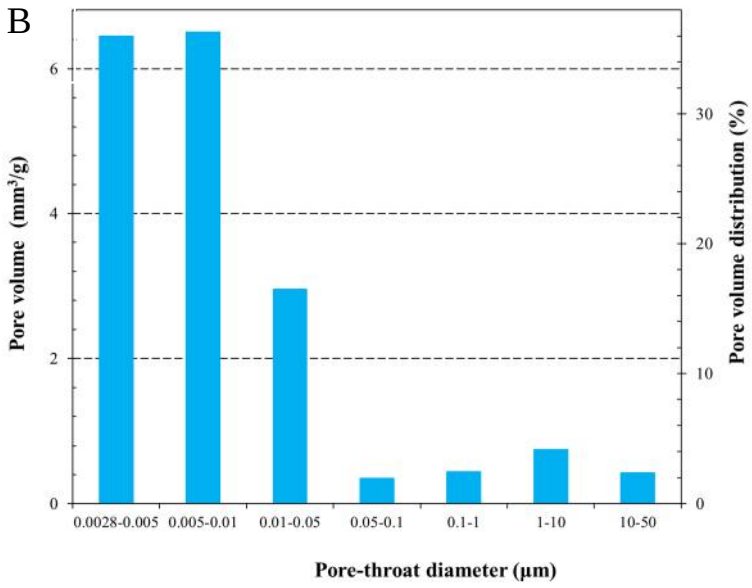

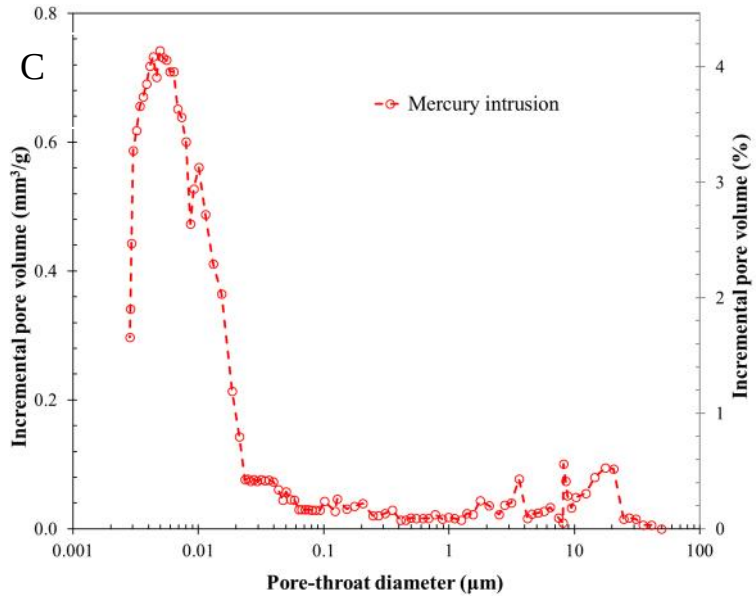

Figure 32. MICP plots of BS 14433-H: A) Inflection points shown with arrows; B) Pore volume vs. pore-throat diameter; C) Incremental pore volume vs. pore-throat diameter.

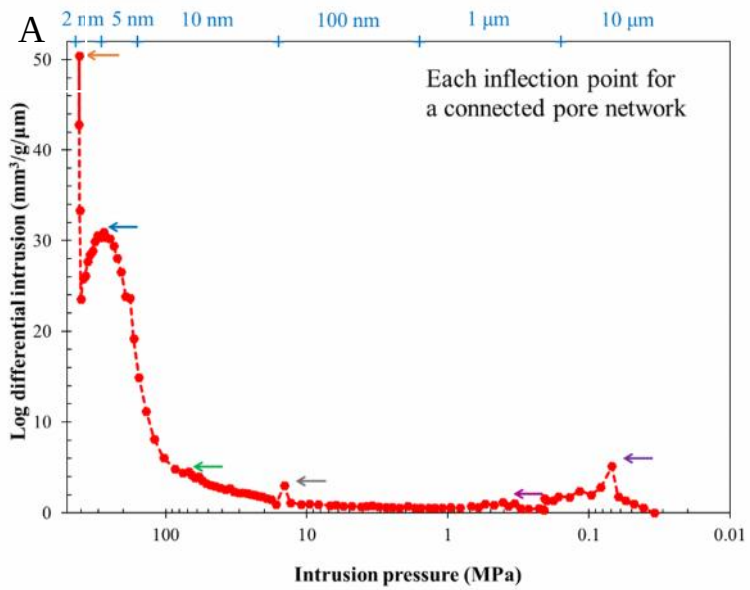

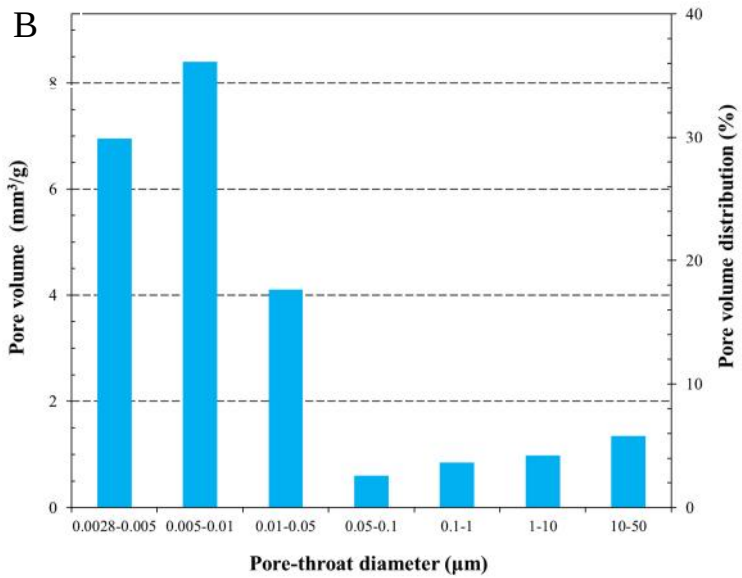

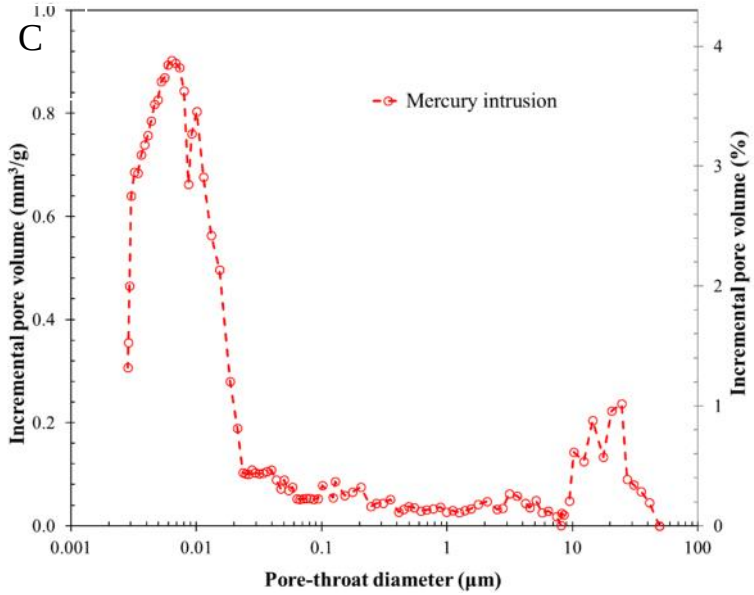

Figure 33. MICP plots of BS 14446-H: A) Inflection points shown with arrows; B) Pore volume vs. pore-throat diameter; C) Incremental pore volume vs. pore-throat diameter.

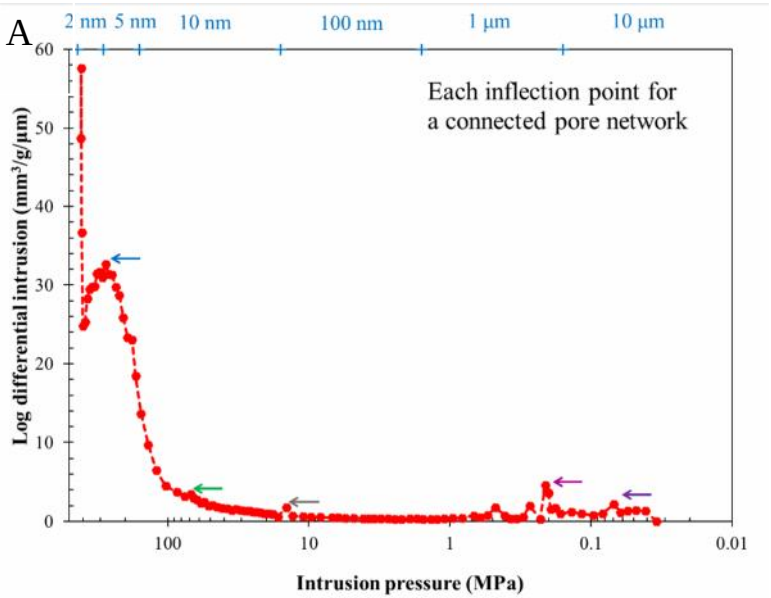

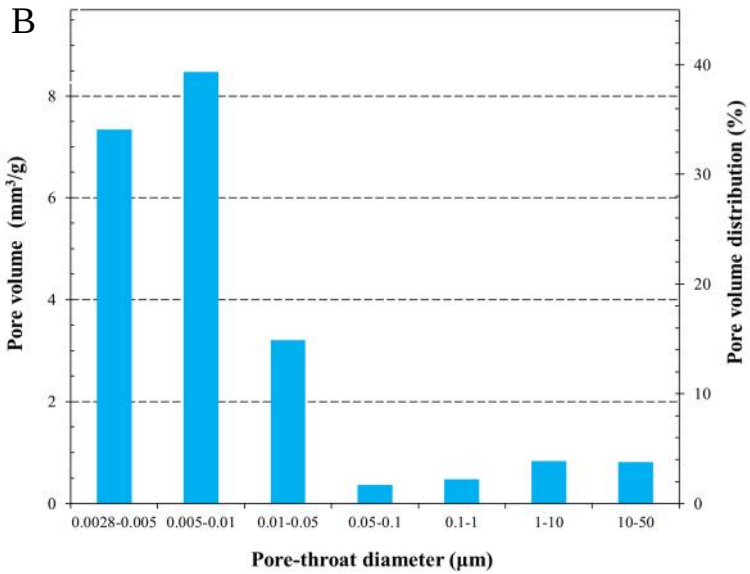

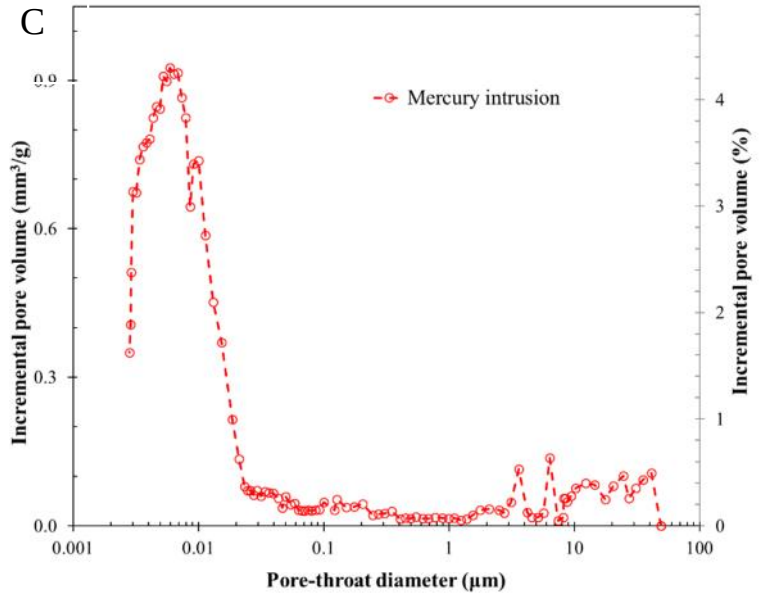

Figure 34. MICP plots of BS 14462-H: A) Inflection points shown with arrows; B) Pore volume vs. pore-throat diameter; C) Incremental pore volume vs. pore-throat diameter.

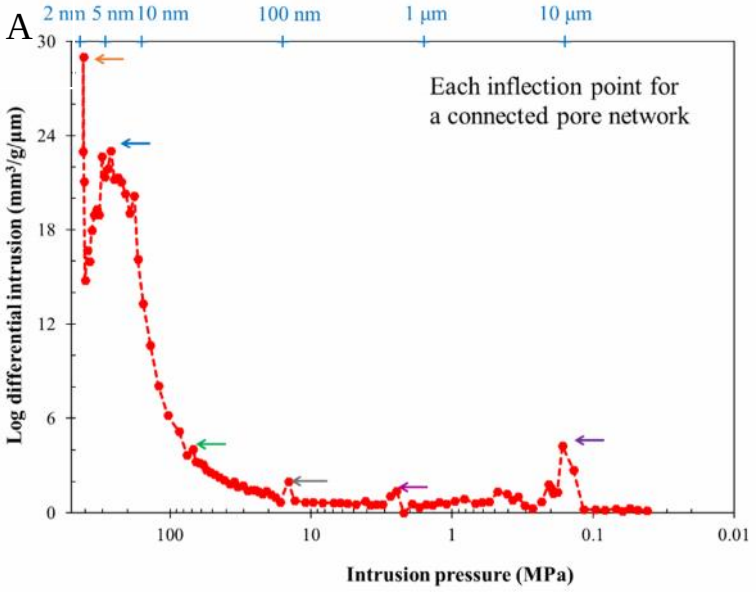

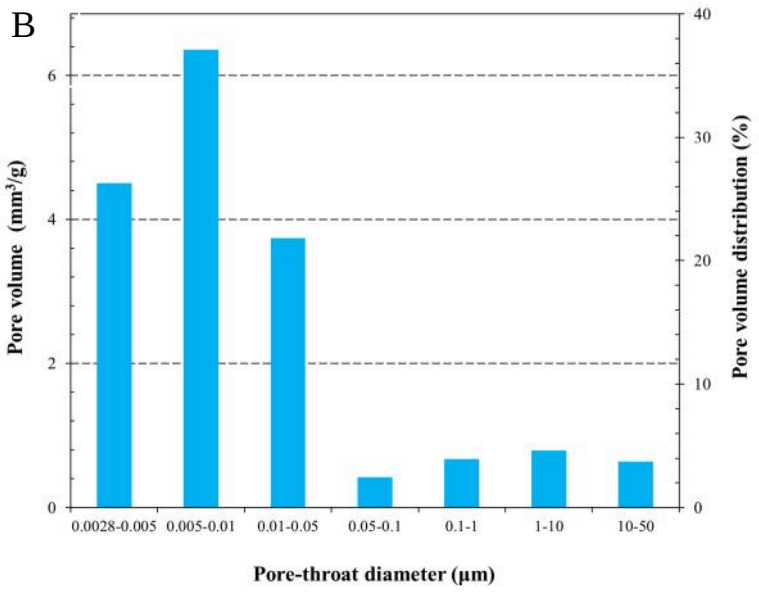

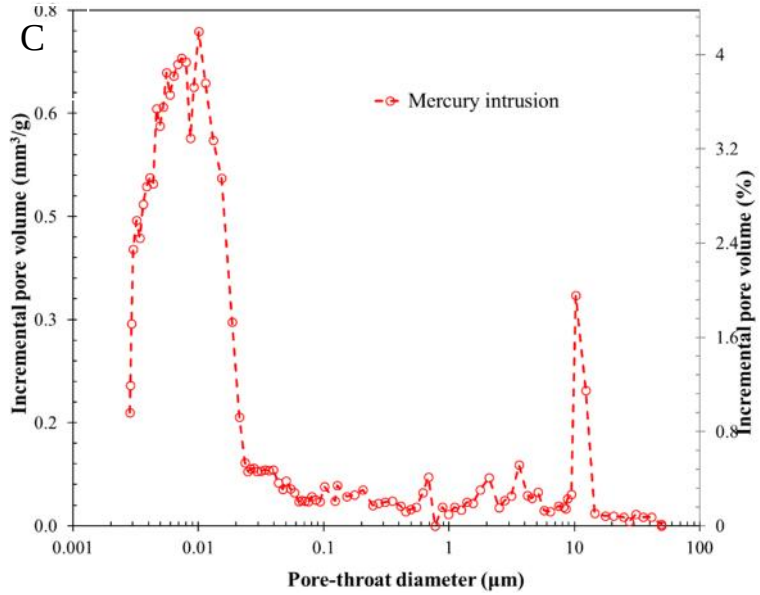

Figure 35. MICP plots of BS 14482: A) Inflection points shown with arrows; B) Pore volume vs. pore-throat diameter; C) Incremental pore volume vs. pore-throat diameter.

4.5 Contact angle and wettability

As a natural material with various compositions, shale has a complex wettability. Understanding wettability is the first step for researchers when studying liquid-solid interaction behavior. The contact angle is used to determine the wettability of shale samples. Four different fluids (DI water, API brine, 10% IPA, and n-decane) were used to measure the contact angles. The contact angle measurement suggested n-decane most easily wets the samples, but they also show a good wetting towards DI water, API brine, and 10% IPA. An example of BS 14411 is presented to explain the contact angle measurement and final results of the contact angle of four fluids vs. log elapsed time. Figure 36 shows the contact angle of DI water, API brine, and 10% IPA at 30 seconds after a droplet of liquid was placed onto the sample surface. Due to the fact that n-decane spreads out on sample surface very quickly, we used a high-speed camera to capture the contact angle images within 1 second. The contact angle detection limit is 3 degrees so that any contact angle less than 3 degrees will not be identified. In Table 10, those values are recorded as < 3 degrees.

Sample ID	DI water	API brine	10% IPA	n-decane	Wettability Classification
BS 14359	58.3	13.2	49.4	<3	Oil-Wet
BS 14374	28.0	22.3	25.0	<3	Oil-Wet
BS 14395	15.4	15.5	33.4	<3	Intermediate-Wet
BS 14404	41.0	30.0	24.3	<3	Oil-Wet
BS 14411	52.6	34.8	38.2	<3	Oil-Wet
BS 14427	33.3	32.5	28.0	<3	Oil-Wet
BS 14433	24.0	38.0	61.3	<3	Intermediate-Wet
BS 14446	7.4	33.3	24.1	<3	Intermediate-Wet
BS 14462	52.8	38.4	50.6	<3	Oil-Wet
BS 14482	46.1	26.9	6.1	<3	Oil-Wet

Table 10. Summary of contact angle data (degree).

A

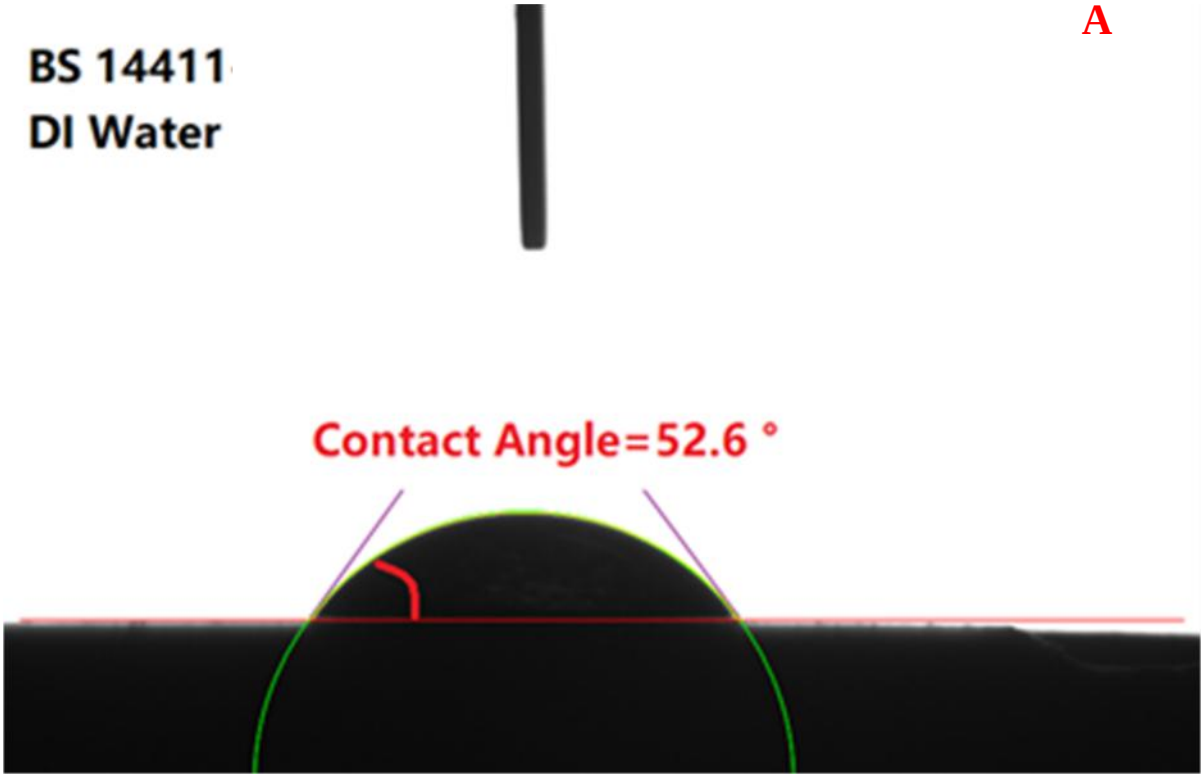
BS 14411
DI Water
Contact Angle=52.6 °

B

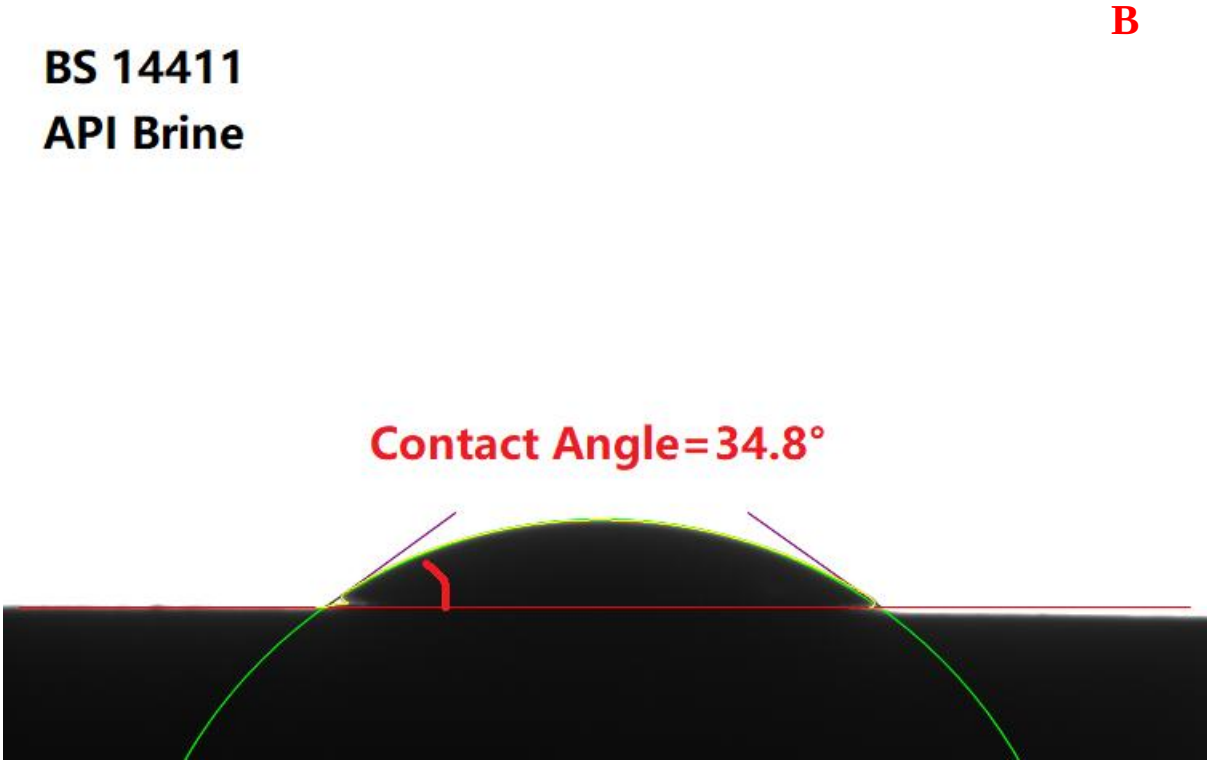
BS 14411
API Brine
Contact Angle=34.8°

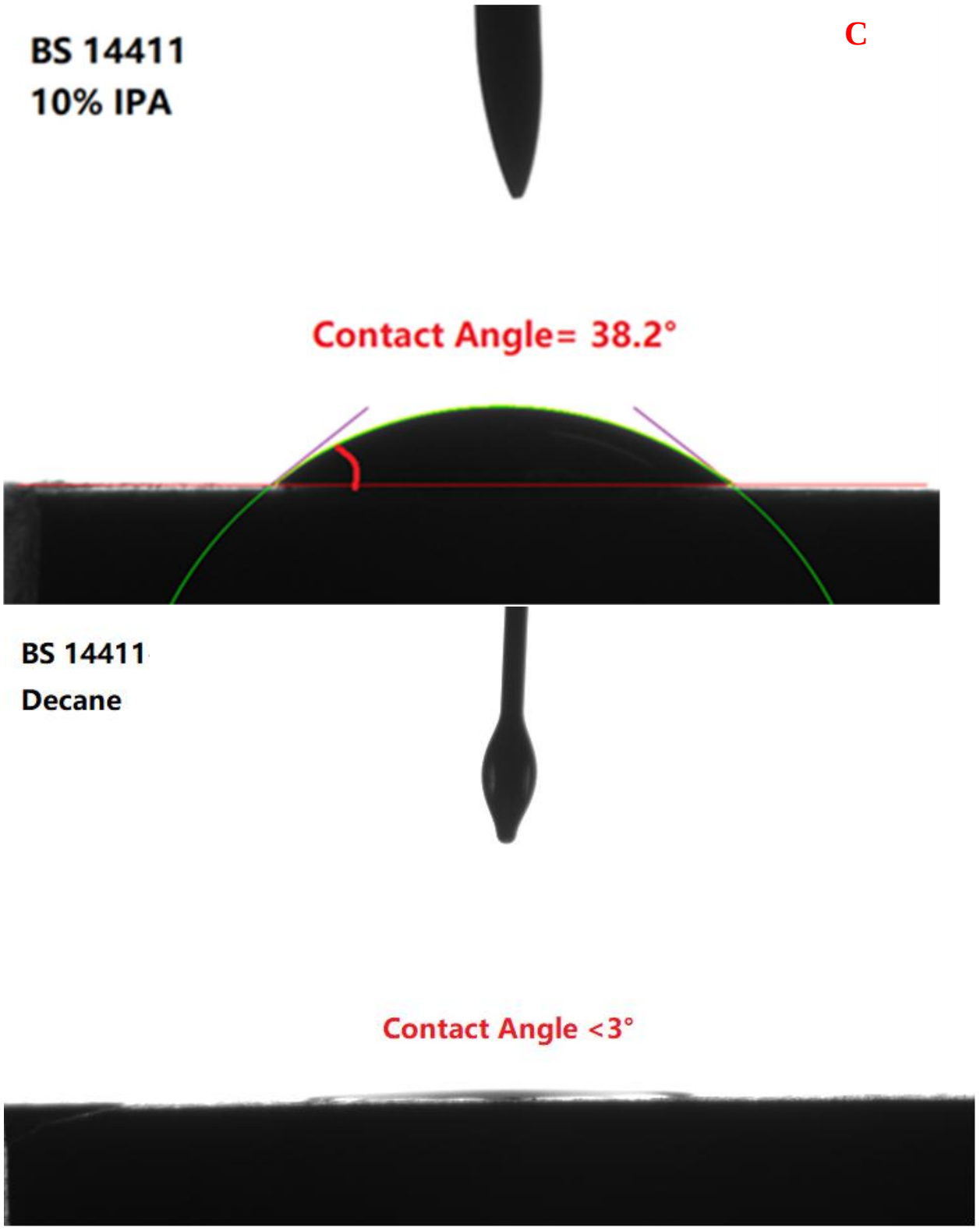

Figure 36. Contact angle of BS 14411-H. A) DI water, B) API Brine, C) 10% IPA, D) Decane.

4.6 Spontaneous imbibition

DI water and DT2 were used to detect wettability related pore connectivity. Based on the imbibition behavior and slope, the imbibition process could be divided into four stages. The first stage is the noisy stage which happens when the sample starts to touch the fluid surface and ends when the sample stops vibrating. The second stage is the fluid imbibition into the wall & edge of the sample. In the third stage, fluid starts to migrate into the interior of the shale matrix. When fluid reaches the top of the sample, the sample does not imbibe more fluid from the reservoir; the process enters the last and 4th stage, the stable stage. Hu et al. (2012) introduced the connectivity classification by the analysis of the interior stage slope. When the slope is about 0.5, the sample has a high connectivity to the imbibing fluid. When the slop is around 0.26, the sample has a low connectivity. The slope between 0.26 to 0.5 is considered as intermediate connectivity for the porous media. In general, the Haynesville shows a high connectivity to hydrophobic fluid and intermediate to low connectivity to the hydrophilic fluid (Table 11). Only BS 14446 shows a high connectivity to both water and DT2. The connectivity is related to the wettability but does not indicate a direct and linear relationship.

Sample ID	Fluid type	Wall & edge slope	Interior stage slope	Connectivity	Fluid type	Wall & edge slope	Interior stage slope	Connectivity
BS 14359	DI Water	0.516	0.430	Intermidate	DT2	1.801	0.660	High
BS 14374	DI Water	2.062	0.288	Low	DT2	0.784	1.108	High
BS 14395	DI Water	0.424	0.381	Intermidate	DT2	0.989	0.678	High
BS 14404	DI Water	1.313	0.519	High	DT2	1.175	0.417	Intermidate
BS 14411	DI Water	2.593	0.468	Intermidate	DT2	1.140	0.496	High
BS 14427	DI Water	2.531	0.428	Intermidate	DT2	1.261	0.573	High
BS 14433	DI Water	0.071	0.455	Intermidate	DT2	3.527	0.750	High
BS 14446	DI Water	-0.194	0.932	High	DT2	3.800	0.638	High
BS 14462	DI Water	0.818	0.234	Low	DT2	0.437	0.314	Intermidate
BS 14482	DI Water	5.697	0.545	High	DT2	5.973	0.450	Intermidate

Table 11. Imbibition results of DI water and DT2 fluids.

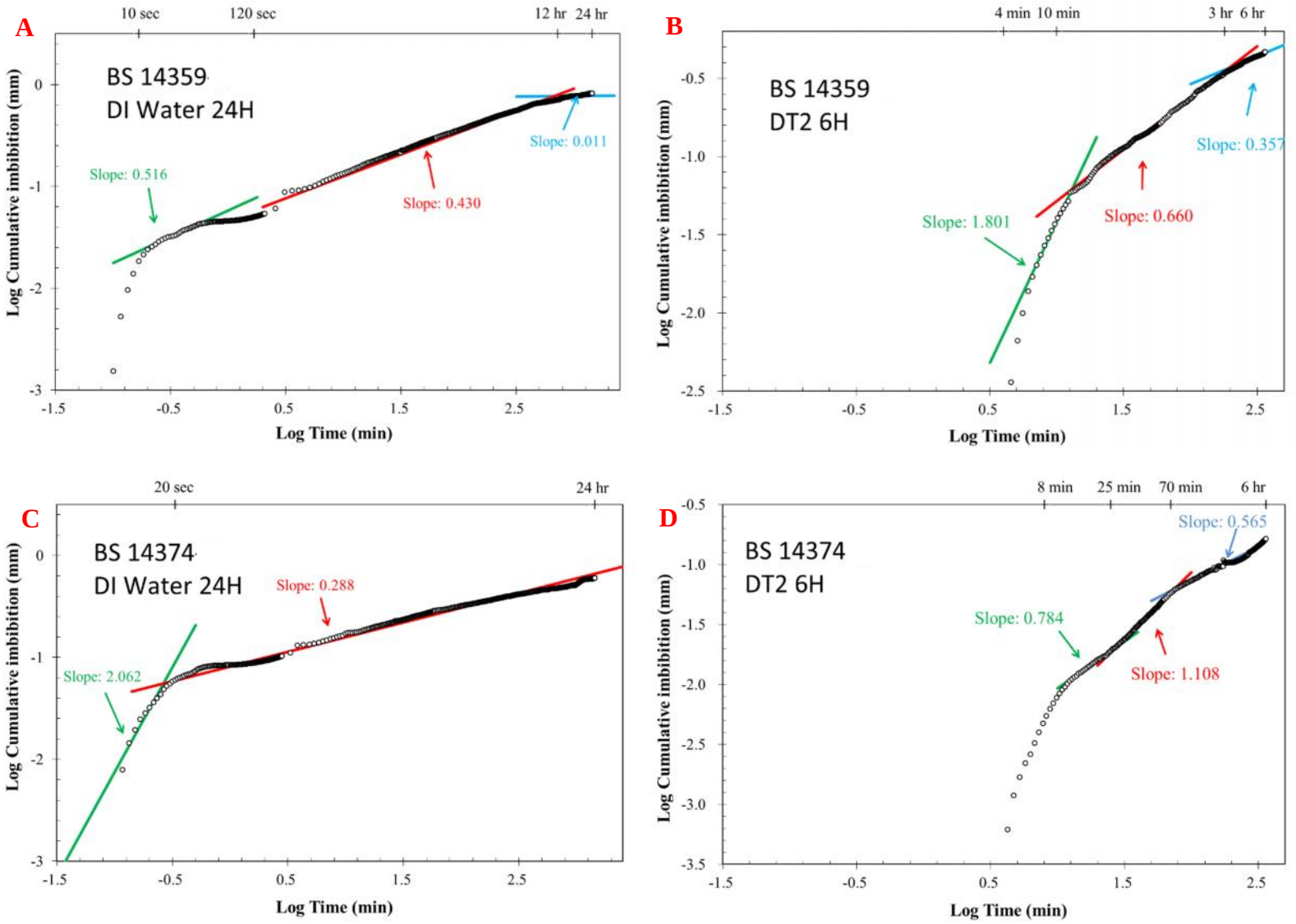

Figure 37. Imbibition for DIW (A and C) and DT2 (B and D) for samples BS 14359 and BS14374, respectively.

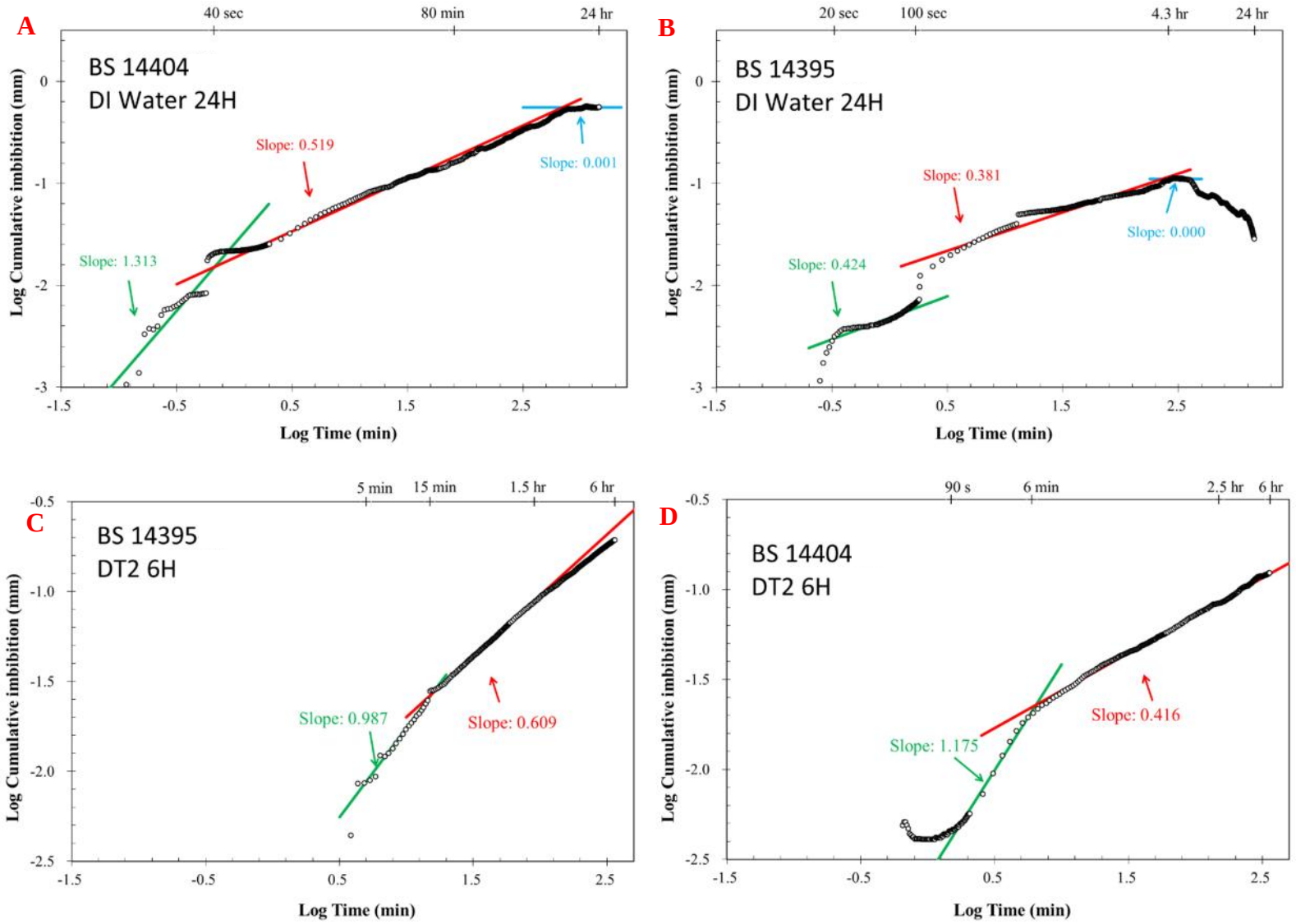

Figure 38. Imbibition for DIW (A and C) and DT2 (B and D) for samples BS 14395 and BS14404, respectively.

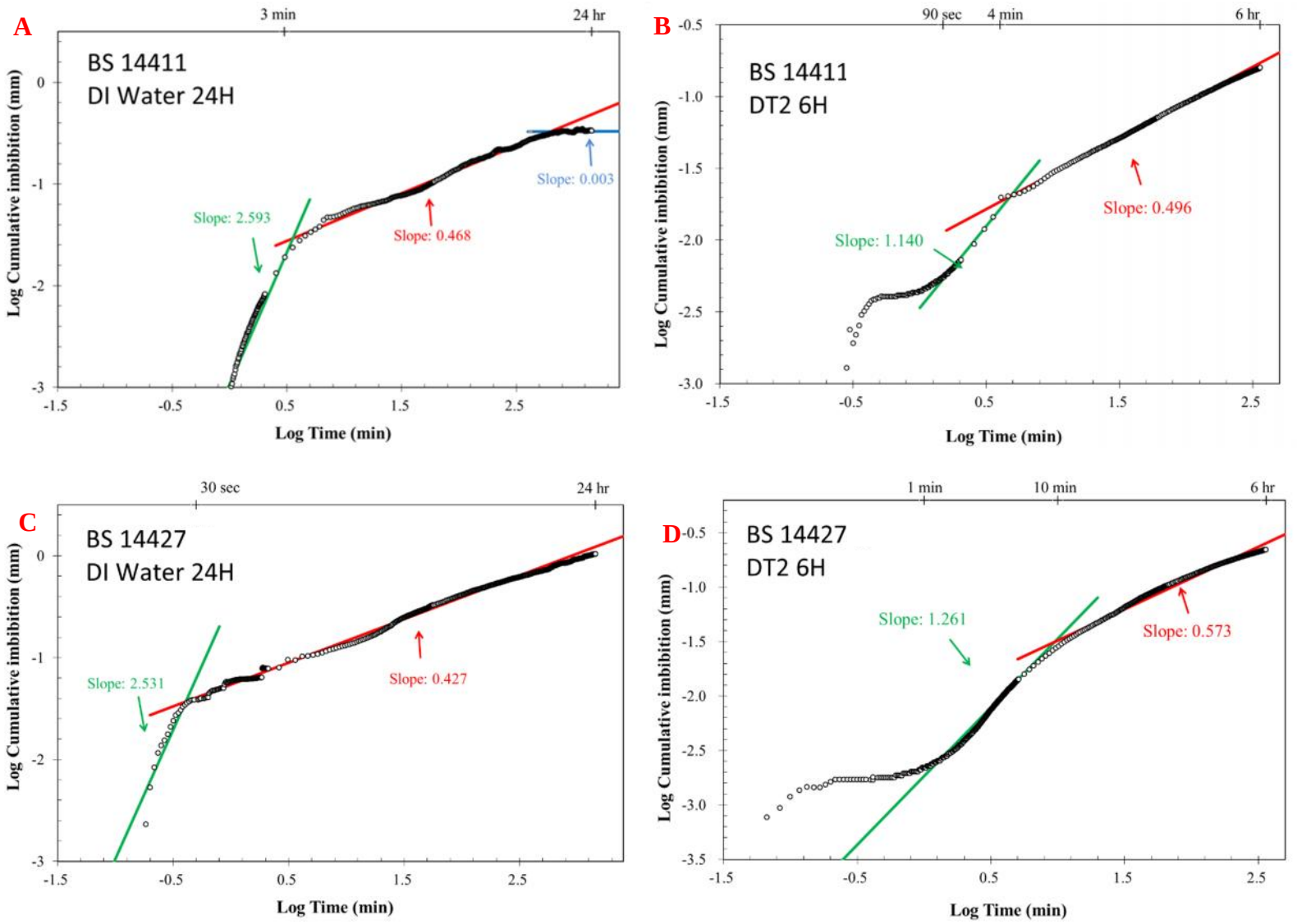

Figure 39. Imbibition for DIW (A and C) and DT2 (B and D) for samples BS 14411 and BS14427, respectively.

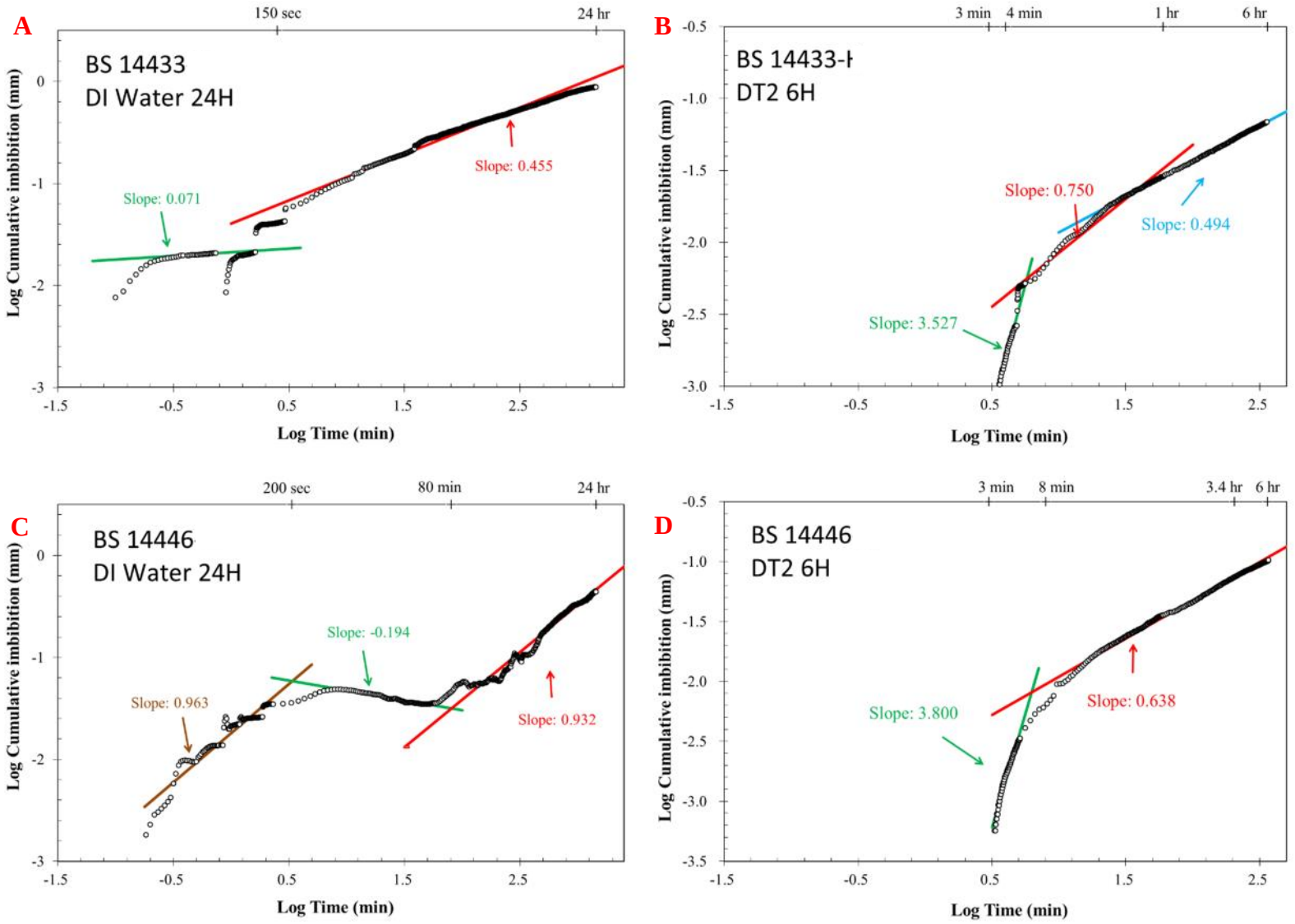

Figure 40. Imbibition for DIW (A and C) and DT2 (B and D) for samples BS 14433 and BS14446, respectively.

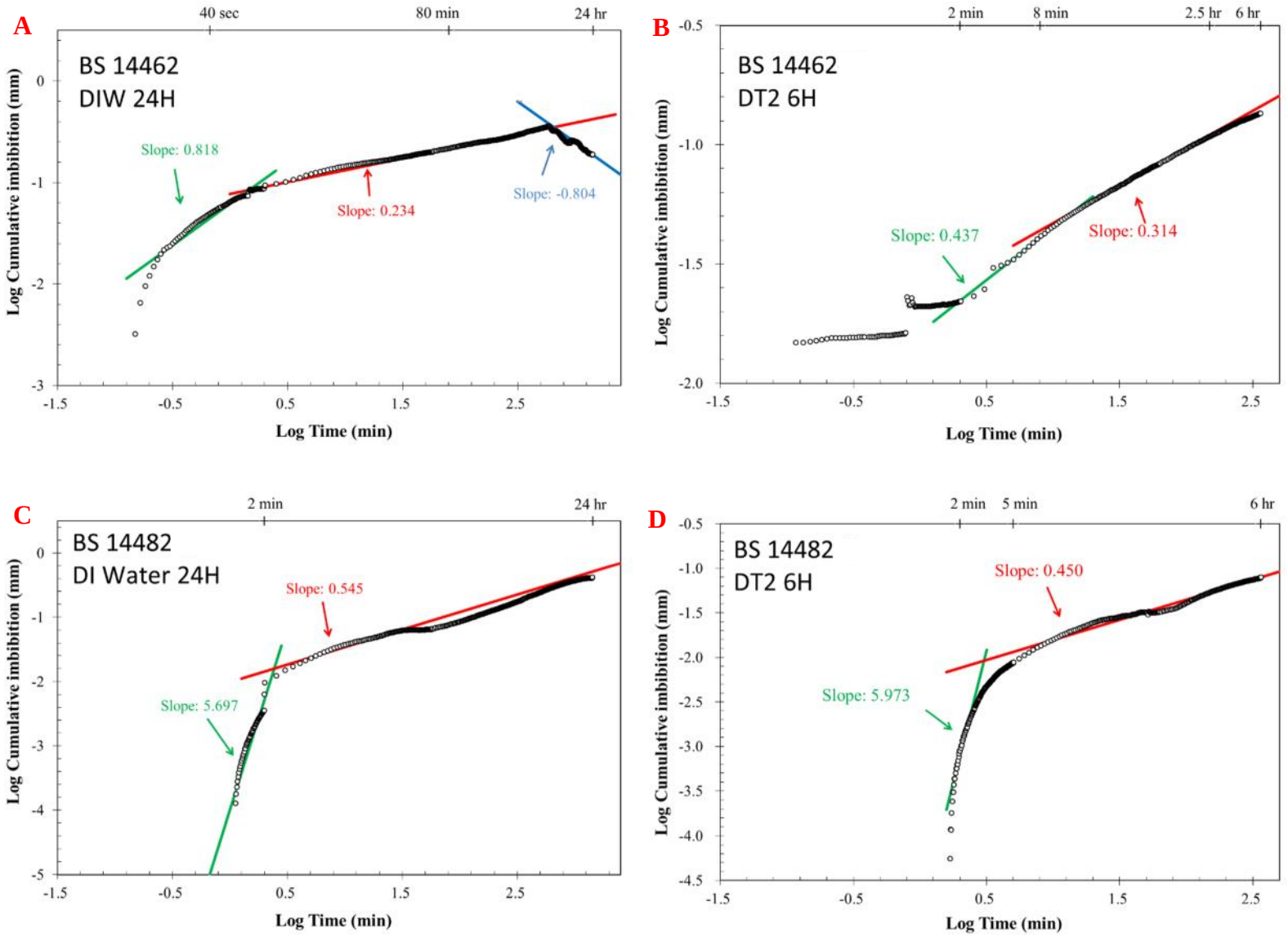

Figure 41. Imbibition for DIW (A and C) and DT2 (B and D) for samples BS 14462 and BS14482, respectively

4.7 Helium pycnometry

Helium pycnometry is one of the best methods to study grain density of porous media. Five different sizes, 1 cm^3 cube, #8 to #12 mesh, #20 to #35 mesh, #35 to #80 mesh, and #80 to #200 mesh samples were used for the analysis in this work. Table 12 presents the results, whereas Figure 42 shows grain density vs. sample size. The obtained grain densities of Haynesville Shale range from 2.594 to 2.832 g/cm^3. Figure 42 shows a slight density increase with decreasing sample size. Some of the samples, such as BS 14374 and BS 14446, show more noticeable trends; their densities increase from 2.661 to 2.767 and 2.466 to 2.656, respectively. The noticeable density increase is not due to analytical errors will be discussed in the Discussion.

Grain density (g/cm^3) / Sample ID	1 cm^3 Cube	#8 to #12 mesh	#20 to #35 mesh	#35 to #80 mesh	#80 to #200 mesh	Average Helium grain density
BS 14359	N/A	2.7356	2.8723	2.9511	2.7682	2.8318
BS 14374	2.6608	2.7466	2.7304	2.8406	2.8552	2.7667
BS 14395	2.4855	2.6371	2.6530	2.6847	2.6592	2.6239
BS 14404	2.5495	2.5873	2.7017	2.7069	2.7879	2.6667
BS 14411	2.5524	2.8869	2.3598	2.7643	3.1231	2.7373
BS 14427	N/A	2.5210	2.5473	2.6105	2.6952	2.5935
BS 14433	2.4581	2.7467	2.7654	2.7258	2.7902	2.6972
BS 14446	2.4665	2.4540	2.7201	2.7520	2.8867	2.6559
BS 14462	2.5021	2.6993	2.7173	2.7390	2.7664	2.6848
BS 14482	2.7283	2.6048	2.7491	2.7274	2.7383	2.7096

Table 12. Helium pycnometry grain density vs. Different sample sizes.

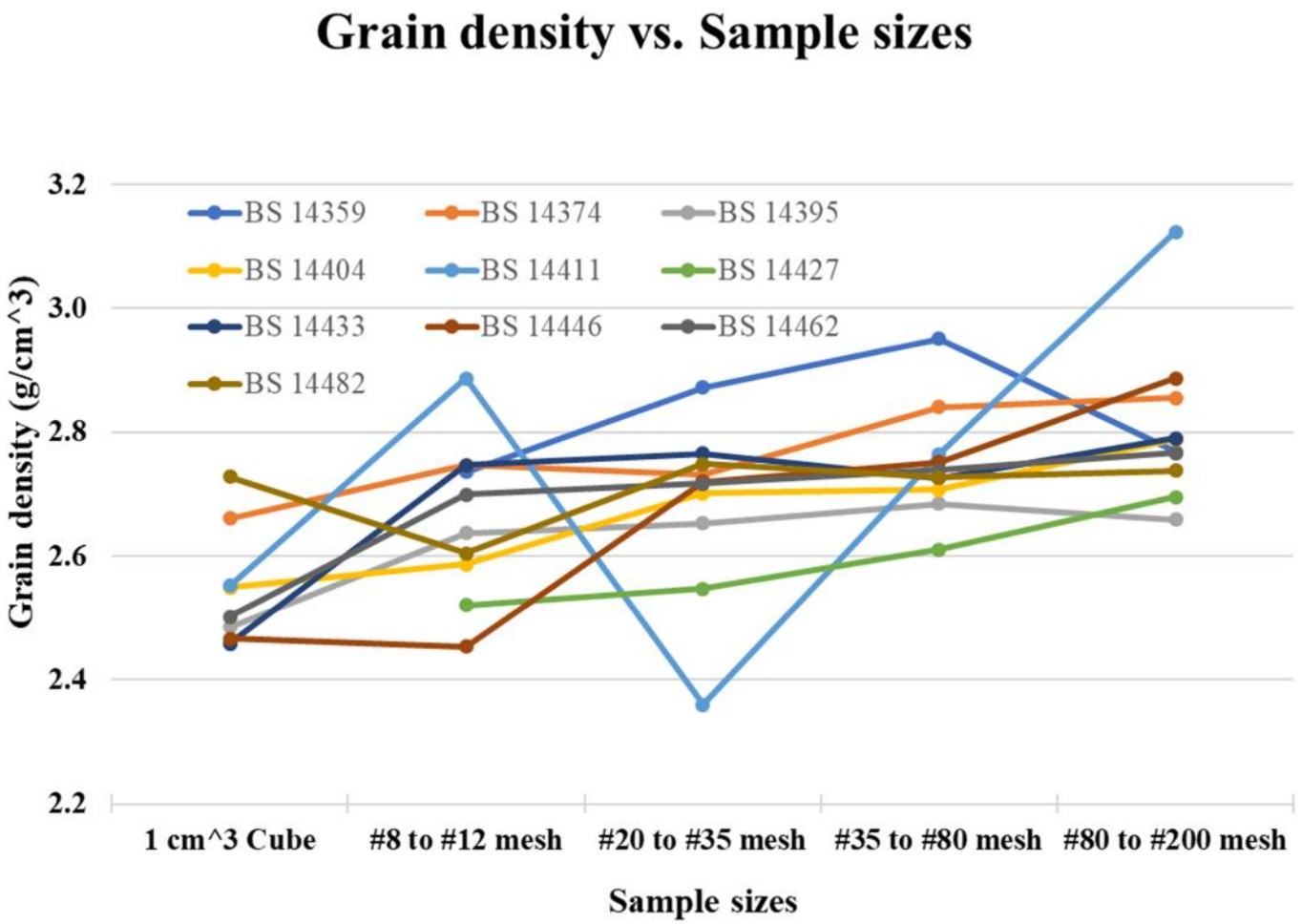

Figure 42. Helium grain density vs. sample sizes.

Chapter 5: Discussion

5.1 Mineralogy

XRD is a direct measurement of mineral composition. Mineralogical studies indicate the depositional environment and if there was any catastrophic event. In the Haynesville Shale, the carbonate group shows an opposite trend with quartz & feldspar group and clay & mica group. It shows that transgressions and regressions happened during deposition. During the transgressions, the study area accepts more marine sediments. When regression replaces transgression, more siliceous sediments charged the study area. Pyrite, as an important indicator for the anoxic environment, accounts for a 2.1% to 5.6%. The presence of considerable pyrite in the Haynesville Shale reveals that although the transgression and regression do influence the sedimentary processes, the study area remained an anoxic and relatively quiet environment. Under this situation, a large amount of organic matter was well preserved and became the source of hydrocarbons. Clay contents are relatively low in the Haynesville Shale, 7.3% to 23.9%. The low clay content in shale has the advantages of increasing formation brittleness and avoiding the swelling problem caused by high clay contents (Zhang et al., 2017).

Lacking petrographic studies in this work, the grain size, grain type, and roundness data are not available. Those petrographic properties can be not only used in the aspect of sedimentology studies such as the provenance of sediments, sedimentary system classification, and basin analysis, but also in the aspect of petrophysical studies to determine the effects of the above properties on porosity, permeability, and tortuosity.

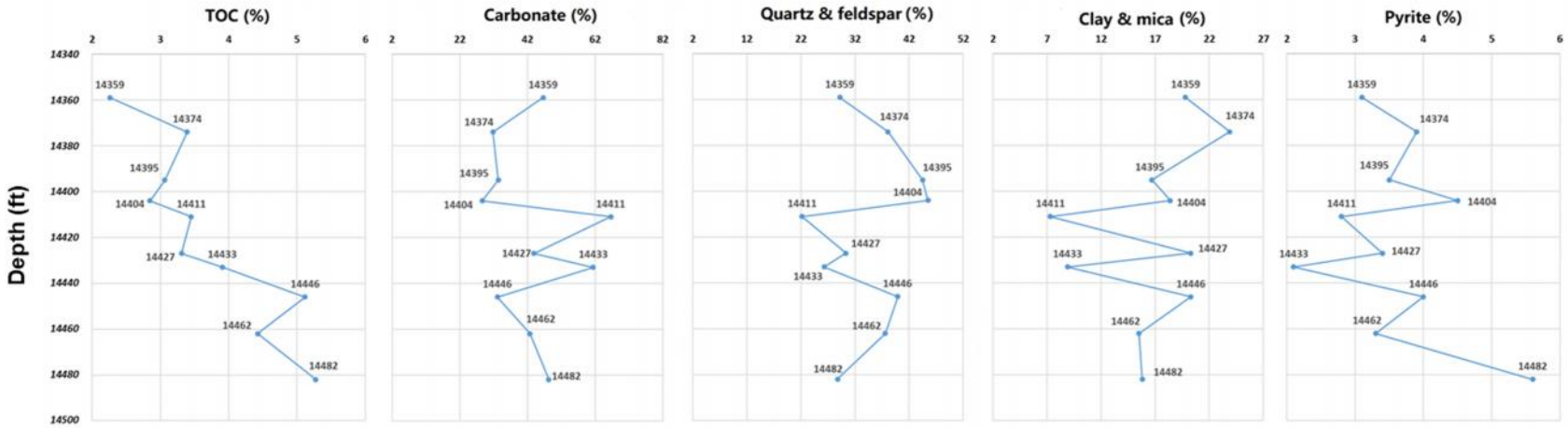

Figure 43. TOC, carbonate, quartz & feldspar, clay & mica, and pyrite vs. depth.

5.2 Organic Richness and Thermal Maturation

Total organic carbon contents obtained from direct measurements range from 2.26 to 5.12%, and values derived from pyrolysis are between 1.97 and 6.40%. The organic richness of the Haynesville Shale is good and meets the general commercial development criteria (Zou, 2013). PI values of this formation range from 0.68 to 1 and the T_{max} between 351.9 °C and 400.1 °C and. A PI value larger than 0.5 indicates that the sample is overmature (Espitalie et al., 1977). In Tissot et al. (1987), T_{max} below 435°C means an immature source rock. In the Haynesville Shale, this criterion is no longer valid. T_{max} is the maximum temperature of the S2 peak point. From Figures 23 to 25, S2 in all the samples are too small, and the correct T_{max} cannot be detected. In other words, during the burial and thermal evolution, most of the kerogen which could generate S2 peak in the pyrolysis tests has been transformed to bitumen. In the study area and across most of basin, the Haynesville Shale is overmature and has less potential to generate more gas.

5.3 Porosity and Permeability

Porosity is a critical parameter to reflects reservoir storage capacity and interior pathways for hydrocarbon migration. In this research, porosity was determined by MICP and vacuum saturation. High heterogeneity of shale is always a big problem for shale characterization. Even two cubes from one core plug could show different results. In addition, various techniques also lead to inconsistent results. For example, the minimum pore-throat size detection limit for MICP is 2.8 nm, any pore space less than 2.8 nm cannot be detected. However, the water molecules can invade pore size large than 0.275 nm. Some pore space cannot be recorded because of the technique limitation. So that in, we set ± 1.5% as porosity heterogeneity evaluation line as the rule of thumb of porosity comparison. The porosity heterogeneity evaluation line is defined as when using different parts of samples from one larger shale sample or using multiple methods to

determine the porosity; a good fitting of measured porosities difference should be less than 1.5%. In this study, porosity measured from MICP, DI water vacuum saturation, and DT2 vacuum saturation agree with each other well. Only some of the THF results show a large offset due to its high evaporation rate which leads to inaccurate measurements. The porosity in the Haynesville ranges from 3% to 8% which is generally lower than other published results of 10.23% (Parker et al., 2009), 8% to 14% (Wang & Hammes, 2010). Such a disagreement probably comes from the locality and the selection of samples.

Due to the ultra-low matrix permeability, conventional permeability methods did not work well on shale. In this study, permeability is estimated from MICP. Permeability values vary from 3.7 to 23.4 nD. Our data are consistent with results from previous studies, such as 5.6 nD calculated by Parker et al. (2009) and 0.2~100 nD measured by Tinni et al. (2012).

Porosity (%) / Sample ID	MICP	Vacuum saturation		
	Mercury	DI Water	DT2	THF
BS 14359	7.313	6.026±1.238	7.774	7.678
BS 14374	6.034	5.841±0.855	7.490	7.910
BS 14395	2.837	2.929±0.367	N/A	3.319
BS 14404	4.712	5.946±1.495	5.527	8.625
BS 14411	3.091	2.626±0.525	3.140	3.548
BS 14427	6.413	6.631±0.890	5.543	1.175
BS 14433	4.406	4.751±0.581	3.778	6.254
BS 14446	5.540	6.173±0.768	5.309	10.422
BS 14462	5.217	5.289±0.380	4.140	6.073
BS 14482	4.245	5.156±0.624	6.918	6.624

Table 13. Porosity (%) determined from different methods for cubic samples.

5.4 Pore Structure

The pore structure of marine shale is controlled by its composition, the total amount of organic matter, cementation, thermal evolution, and burial history. In this study, the pore structure was characterized by MICP which can generate porosity, permeability, pore-throat size distribution, and tortuosity. Although the samples are from different depths with various mineral compositions and TOC contents, the pore structure of the Haynesville Shale is consistently similar. From MICP results, the pore-throat sizes are concentrated in the 2.8 to 50 nm range, and the effectivity tortuosity and geometrical tortuosity varies from 1413 to 3433 and 8 to 12, respectively. The geometrical tortuosity is the tortuosity only be used to characterize tortuous pathways geometrically. The effective tortuosity takes the fluid movement into considering and can explain the complexity of pathways that fluid moving in the porous media have to undergo. Those nanopores are mainly inter-clay platelet layer pores, organic pores, and intraparticle pores. From the aspect of pore composition and morphology, pores are divided into inter-clay platelet pores, organic pores, intraparticle pores, interparticle pores, microfractures, and natural fractures. With respect to fluid migration, pore types can be merged into organic pores, inorganic pores, and fractures.

Fluid migration in shale is complex; it includes flow mechanisms from nanometer to micrometer scales. Fluid flow includes (1) free gas flow in natural fractures; (2) gas desorption from the surface of kerogen into the pore space; (3) gas diffusion between the interior of the kerogen and the surface of the kerogen; and (4) liquid imbibition (Javadpour et al., 2007; Wang & Reed, 2009). Natural fractures provide a pathway for free gas to connect to hydraulic fractures and the wellbore. Due to its oil-wetting characteristics, organic matter is like filters which block the

hydrophilic fluids and only allow hydrophobic fluids to flow through it. This behavior indicates that samples with higher TOC contents have the potential to have higher permeability towards hydrophobic fluids. Fluid imbibition is also related to wettability; this will be detailed discussed later.

The tortuosity reflects the complexity of the pore structure. It explains the exact travel length of a liquid molecule through porous media between two ends of a straight line. As highly heterogeneous porous media with various compositions and pore types, the shale shows a high effective tortuosity. The effective tortuosity of 2.8nm to 50 nm pore-throats in the Haynesville Shale ranges from 1413 to 3433 and the geometrical tortuosity ranges from 8 to 12. The geometrical tortuosity of 8 to 12 indicates that for one fluid molecule to travel 1 cm in a straight line, the distance it actually needs to travel is 8 to 12 cm.

5.5 Wettability Related Connectivity

Pore connectivity of shale is highly related to wettability. Organic-rich shale has the preference to be oil-wet because of the high TOC content and well-developed organic matter-hosted pores in the gas generating window. The organic matter acts as a nano filter which will block the hydrophilic fluid but allow the hydrophobic fluids to pass through (Wang & Reed, 2009). Our contact angle results showed that 7 samples are only oil-wet and 3 samples are intermediately wet (both wet to hydrophilic and hydrophobic fluids). Imbibition results with two wettability fluids suggest that the Hayneville Shale has the preference to imbibe hydrophobic fluid (DT2) with a high fluid uptake rate. Although the uptake rate of the hydrophilic fluid is not as high as that of hydrophobic fluid, eight samples still show intermediate to high rates of the hydrophilic fluid, consistent with low to modest contact angle measurements towards both DI water and API brine.

5.6 Density and Sources of Error

Density is also an important parameter in the shale reservoir evaluation. Table 14 illustrates the density results of cubic samples measured by different methods. The results agree with each other very well.

Helium pycnometry was not only applied to the cubic sample, but also to granular samples. The slight grain density increase with a decreasing sample size is caused by the opening of isolated pore space which makes samples slightly denser.

Each experiment has its sources of error, and a clear understanding of those sources of error can help researchers reduce inaccurate operations and assess the pros and cons of each method.

The sources of errors from liquid vacuum saturation measurement and helium pycnometry have been discussed in detail in Helsel et al. (2016) and were also observed in this study.

For vacuum saturation fluid density measurement, human error cannot be neglected. When weighing the fluid-saturated samples, we usually wipe out extra fluid by moist Kimwipe. Although we try only to wipe out the extra fluid and keep the surface of the sample moist, there could be an error especially for low porosity samples. Another source of error is caused by fluid evaporation. Fluid evaporation from the saturated sample will cause a lower mass of saturated sample and liquid evaporation from Archimedes' bucket will cause a decrease in measured bulk volume. Among three fluids used in porosity and density measurement, THF has the highest evaporation rate which poses a big challenge during the measurements. However, the high evaporation rate of THF could lead to a smaller porosity, and our results (Table 13) still mostly show larger porosity results than DI water and DT2 fluids; this indicates that amphiphilic fluid of THF is able to access more pore spaces, both hydrophilic and hydrophobic.

Helium pycnometry has two major types of error. The first source of error is temperature. The temperature in the laboratory is set to be constant, but the temperature of the helium pycnometry will not always be stable. After several test runs, the vacuum pump will become a heat source which will heat helium. The second source of error is from the transportation of sample from balance to pycnometry. The improper handling of operators may lose some sample, especially when the sample size is very small.

Density (g/cm^3) / Sample ID	Helium Grain density	MICP bulk density /MICP grain density	Vacuum saturation DI water bulk density / grain density	Vacuum saturation DT2 bulk density / DT2 grain density	Vacuum saturation THF bulk density / THF grain density	Average of bulk density / average of grain density
BS 14359		2.417	2.497	2.578	2.555	**2.512±0.062**
	N/A	2.608	2.657	2.795	2.767	**2.707±0.077**
BS 14374		2.439	2.394	2.459	2.442	2.434±0.024
	2.661	2.596	2.543	2.658	2.652	2.622±0.046
BS 14395		2.482	2.447	N/A	2.557	**2.495±0.046**
	2.486	2.554	2.521	N/A	2.645	**2.552±0.059**
BS 14404		2.381	2.354	2.419	2.429	2.396±0.03
	2.549	2.498	2.503	2.561	2.658	2.554±0.058
BS 14411		2.454	2.461	2.506	2.558	**2.495±0.042**
	2.552	2.532	2.528	2.588	2.652	**2.57±0.046**
BS 14427		2.344	2.329	2.375	2.427	2.369±0.038
	N/A	2.504	2.495	2.514	2.456	2.492±0.022
BS 14433		2.458	2.454	2.486	2.540	**2.484±0.034**
	2.458	2.572	2.576	2.583	2.709	**2.58±0.08**
BS 14446		2.382	2.366	2.390	2.352	2.373±0.015
	2.466	2.522	2.522	2.524	2.626	2.532±0.052
BS 14462		2.423	2.402	2.455	**2.480**	**2.44±0.03**
	2.502	2.556	2.536	2.561	**2.641**	**2.559±0.046**
BS 14482		2.478	2.434	2.461	2.526	2.475±0.034
	2.728	2.588	2.566	2.644	2.706	2.646±0.063

Table 14. Density measurements of cubic samples from different methods.

5.7 Reservoir quality evaluation

To evaluate the reservoir quality, Burnaman et al. (2009) came up with 17 criteria. By adding more criteria in the nano-petrophysical and geochemical aspects, modified criteria are shown in Table 15, and criteria in orange-colored cells are applied in this study.

Geology	Mineral conposition	Tectonic setting	Lateral continuity of shale	Absolute age of shale	
Geochemical	Organic richness	kerogen type	Thermal maturation	Wettability	
Storage capacity	Shale thickness	Gas-in-place and reserves	Porosity	Permeability	
Nano-petrophysics	Pore type	Pore distribution	Connectivity	Tortuosity	
Engineering	Shale brittleness	3-D sesmic avaliable prior to drilling	Pressure gradient	Tranport infrasturture in place	Drill sites with easy access and constraution
Environmental	Produced water dispoal	Logistics of water supplies for hydraulic fracturing			

Table 15. Reservoir evaluation criteria (modified from Burnaman et al. 2009).

In this study, we adopted 12 parameters to evaluate the Haynesville Shale. Table 16 provides all results for reservoir evaluation.

1) Mineral composition: around 70% of the minerals are brittle ones (carbonate, quartz, and mica), clay content ranges from 7.3 to 20.3%.
2) Organic richness: TOC ranges from 2.26 to 5.28 and show a generally increasing trend with increasing depth.
3) Thermal maturation: overmatured shale, no hydrocarbon generation potential.
4) Wettability: strongly oil-wet, modestly water-wet.

5) Shale thickness: the total thickness is 123 ft in this area.
6) Porosity: 3-8%.
7) Permeability: 3.7 to 23.4 nD.
8) Pore type: inter-clay platelet pores, organic pores, intraparticle pores.
9) Pore distribution: pore-throat sizes concentrated in 2.8 to 50 nm.
10) Connectivity: good connectivity to hydrophobic fluid and intermediate connectivity to the hydrophilic fluid.
11) Tortuosity: effectivity tortuosity and geometrical tortuosity various from 1413 to 3433 and 8 to 12, respectively.
12) Pressure gradient: >0.9 psi/ft.

Sample ID	Depth (ft)	Lithology	TOC (%)	MICP porosity (%)	DI Water porosity (%)	2.8-50 nm pore volume to the whole pore volume (%)	MICP (2.8-50 nm pore system) Permeability (nD)	Effective tortuosity (2.8-50 nm pore system)	Geometrical tortuosity (2.8-50 nm pore system)	Average grain density (MICP, vacuum saturation, helium pycnometry) g/cm^3	Average bulk density (MICP, vacuum saturation) g/cm^3	Wettability	Hydrophilic connectivity	Hydrophobic connectivity
BS 14359	14358.5	Mixed Mudstone	2.261	7.313	6.026±1.238	70.318	23.4	1580	10.748	2.512±0.062	2.707±0.077	Oil-wet	Intermidate	High
BS 14374	14374	Mixed Mudstone	3.393	6.034	5.841±0.855	85.775	13.1	1914	10.746	2.434±0.024	2.622±0.046	Oil-wet	Low	High
BS 14395	14395	Carbonate/Siliceous Mdustone	3.065	2.837	2.929±0.367	69.066	7.9	3433	9.870	2.495±0.046	2.552±0.059	Intermediate-wet	Intermidate	High
BS 14404	14404	Mixed Mudstone	2.848	4.712	5.946±1.495	82.528	4.8	3296	12.461	2.396±0.03	2.554±0.058	Oil-wet	High	Intermidate
BS 14411	14411	Silica-rich Carbonate mudstone	3.452	3.091	2.626±0.525	87.648	3.7	2011	7.884	2.495±0.042	2.57±0.046	Oil-wet	Intermidate	High
BS 14427	14426.5	Mixed Mudstone	3.309	6.413	6.631±0.890	86.138	6.5	1879	10.977	2.369±0.038	2.492±0.022	Oil-wet	Intermidate	High
BS 14433	14432.5	Silica-rich Carbonate mudstone	3.906	4.406	4.751±0.581	88.878	4.0	1753	8.788	2.484±0.034	2.58±0.08	Intermediate-wet	Intermidate	High
BS 14446	14446	Mixed Mudstone	5.117	5.540	6.173±0.768	83.709	6.4	2570	11.932	2.373±0.015	2.532±0.052	Intermediate-wet	High	High
BS 14462	14462	Carbonate/Siliceous Mdustone	4.424	5.217	5.289±0.380	88.376	4.7	2751	11.979	2.44±0.03	2.559±0.046	Oil-wet	Low	Intermidate
BS 14482	14482	Mixed Carboante Mudstone	5.276	4.245	5.156±0.624	85.208	5.9	1413	8.586	2.475±0.034	2.646±0.063	Oil-wet	High	Intermidate

Table 16. Result compilation of Haynesville Shale.

Chapter 6: Conclusions

6.1 Conclusions

Overall, the thick (123 ft), overmature, organic-rich (TOC 2.26-2.58%) Haynesville Shale is a good shale gas reservoir with a relatively high porosity (3-8%), and the high-pressure gradient (>0.9psi/ft) provides good driving force for production. High hydrophobic connectivity indicates oil and gas migrate faster than water in the formation. However, small pore-throat sizes (2.8-50 nm), ultra-low permeabilities (3.7 to 23.4 nD) and high effective tortuosity (1413-3433) and geometrical tortuosity (8-12) increase production difficulties. A high percentage of brittle mineral content (~70%) and low clay content (<20%) make hydraulic fracturing easier, but the intermediate hydrophilic connectivity will lead to the loss of a large amount of hydraulic fracturing water in the long term.

6.2 Future works

To evaluate more aspects of the Haynesville Shale, petrographic thin section and SEM imaging, and lithofacies identification from well logs need to be conducted along with the methods used in this study. Although most of the grains in mudstone are too fine to be identified by polarizing microscopy, there is still a large amount of information (grain type, grain size, roundness, sedimentary structures, cementation) to be extracted from the petrographic thin section studies. In addition, the current pore system characterization methods do not include any imaging method. SEM images provide an intuitive understanding of pore type and morphology. Lastly, sedimentary process is one of the most critical factors

controlling shale evolution. Having a better understanding on both sedimentology and nano-petrophysics will give petroleum geologists more insights for effective oil and gas exploration.

References

Adams, R. L. (2009). Basement tectonics and origin of the Sabine Uplift. *Gulf Coast Association of Geology Societites Tranasctions*, *59*, 3–19.

American Petroleum Institute. (1998). RP-40 Recommended practices for core analysis section. In *API Recommended Practice* (2rd ed.). Washington, D.C: API Publishing Services.

Arthur, D. J., Bohm, B., Coughlin, B. J., & Layne, M. (2008). Hydraulic fracturing considerations for natural gas wells of the Fayetteville Shale. *Gulf Coast Association of Geological Societies Transactions*, *59*, 49–59.

Baihly, J. D., Altman, R. M., Malpani, R., & Luo, F. (2010). Shale gas production decline trend comparison over time and basins. *SPE Annual Technical Conference and Exhibition*, (September), 19–22.

Boggs, S. (2009). *Petrology of Sedimentrary Rocks* (2nd ed). Cambridge: Cambridge University press.

Brown, A. A. (2015). Interpreting permeability from mercury injection capillary pressure data. *AAPG 2015 Annual Convention and Exhibition*, *41660*, 3–5.

Burnaman, M., Xia, W., & Shelton, J. (2009). Shale gas play screening and evaluation criteria. *China Petroleum Exploration*, (3), 1–23.

Chen, S., Zhu, Y., Wang, H., Liu, H., Wei, W., & Fang, J. (2011). Shale gas reservoir characterisation: A typical case in the southern Sichuan Basin of China. *Energy*, *36*(11), 6609–6616.

Cicero, A. D., & Steinhoff, I. (2013). Sequence stratigraphy and depositional environments of

the Haynesville and Bossier Shales, East Texas and North Louisiana. In *AAPG Memoir 105* (pp. 25–46).

Clarkson, C. R., Solano, N., Bustin, R. M., Bustin, A. M. M., Chalmers, G. R. L., He, L., Melnichenko, Y.B., Radlin´ ski, A.P., Blach, T. P. (2013). Pore structure characterization of North American shale gas reservoirs using USANS/SANS, gas adsorption, and mercury intrusion. *Fuel*, *103*, 606–616.

Cui, X., Bustin, A. M. M., & Bustin, R. M. (2009). Measurements of gas permeability and diffusivity of tight reservoir rocks: Different approaches and their applications. *Geofluids*, *9*(3), 208–223.

Daigle, H. (2016). Application of critical path analysis for permeability prediction in natural porous media. *Advances in Water Resources*, *96*, 43–54.

Dehghanpour, H., Lan, Q., Saeed, Y., Fei, H., & Qi, Z. (2013). Spontaneous imbibition of brine and oil in gas shales: Effect of water adsorption and resulting microfractures. *Energy and Fuels*, *27*(6), 3039–3049.

Dehghanpour, H., Zubair, H. A., Chhabra, A., & Ullah, A. (2012). Liquid intake of organic shales. *Energy and Fuels*, *26*(9), 5750–5758.

Espitalie, J., Madec, M., Tissot, B., Mennig, J. J., & Leplat, P. (1977). Source rock characterization method for petroleum exploration. *Offshore Technology Conference*.

Euzen, T. (2011). *Shale Gas : An Overview*. https://doi.org/10.13140/RG.2.1.2236.6242

Ewing, T. E. (2009). The ups and downs of the Sabine Uplift and the Northern Gulf of Mexico Basin: Jurassic basement blocks, Cretaceous thermal uplifts, and Cenozoic flexure. *Gulf*

Coast Association of Geological Societies Transactions, *59*, 253–269.

Folk, R. L. (1980). Petrologie of Sedimentary Rocks. Hemphll Publishing Company, Austin.

Galloway, W. E. (2008). Chapter 15 Depositional evolution of the Gulf of Mexico sedimentary basin. In *Sedimentary Basins of the World* (Vol. 5).

Gao, Z., & Hu, Q. (2013). Estimating permeability using median pore-throat radius obtained from mercury intrusion porosimetry. *Journal of Geophysics and Engineering*, *10*(2).

Gao, Z., & Hu, Q. (2016a). Initial water saturation and imbibition fluid affect spontaneous imbibition into Barnett shale samples. *Journal of Natural Gas Science and Engineering*, *34*, 541–551.

Gao, Z., & Hu, Q. (2016b). Wettability of Mississippian Barnett Shale samples at different depths: Investigations from directional spontaneous imbibition. *AAPG Bulletin*, *100*(1), 101–114.

Gao, Z., Hu, Q., & Liang, H. (2013). Gas diffusivity in porous media: determination by mercury intrusion porosimetry and correlation to porosity and permeability. *Journal of Porous Media*, *16*(7), 607–617.

Goldhammer, R. K. (1998). Second-order accommodation cycles and points of "stratigraphic turnaround": implications for carbonate buildup reservoirs in Mesozoic Carbonate Systems of the East Texas Salt Basin and South Texas. In W. D. Demis & M. K. Nelis (Eds.), *West Texas Geological Society Annual Field Conference Guildbook* (pp. 11–28). West Texas Geologic Society Publication.

Ground Water Protection Council. (2009). *Modern shale gas development in the United States: A*

Primer. Retrieved from https://energy.gov/sites/prod/files/2013/03/f0/ShaleGasPrimer_Online_4-2009.pdf

Hammes, U., & Frébourg, G. (2012). Haynesville and Bossier mudrocks: A facies and sequence stratigraphic investigation, East Texas and Louisiana, USA. *Marine and Petroleum Geology*, *31*(1), 8–26.

Hammes, U., Hamlin, H. S., & Ewing, T. E. (2011). Geologic analysis of the upper jurassic haynesville shale in east Texas and west Louisiana. *AAPG Bulletin*, *95*(10), 1643–1666.

Handy, L. L. (1960). Determination of effective capillary pressures for porous media from imbibition data. *Differential Equations*, *219*, 75–80.

Helsel, M. A., Ferraris, C. F., & Bentz, D. (2016). Comparative study of methods to measure the density of cementitious powders. *Journal of Testing and Evaluation*, *44*(6), 20150148.

Hu, Q., Ewing, R. P., & Dultz, S. (2012). Low pore connectivity in natural rock. *Journal of Contaminant Hydrology*, *133*, 76–83.

Hunt, A. G., & Gee, G. W. (2002). Application of critical path analysis to fractal porous media: Comparison with examples from the Hanford site. *Advances in Water Resources*, *25*(2), 129–146.

Institute for Energy Research. (2011). *Haynesville Shale fact sheet*. Retrieved from Insittute for Energy Research website: http://instituteforenergyresearch.org/wp-content/uploads/2012/08/Haynesville-Shale-Fact-Sheet.pdf

Jarvie, D. M. (2012). Shale Resource Systems for Oil and Gas: Part 1—Shale-gas Resource Systems. *Shale Reservoirs—Giant Resources for the 21st Century: AAPG Memoir 97*,

97(AAPG Mem.), 89–119.

Javadpour, F., Fisher, D., & Unsworth, M. (2007). Nanoscale gas flow in shale gas sediments. *Journal of Canadian Petroleum Technology*, *46*(10), 55–61.

Kargbo, D. M., Wilhelm, R. G., & Campbell, D. J. (2010). Natural gas plays in the Marcellus Shale: Challenges and Potential Opportunities. “Tapping the lucrative Marcellus Shale natural gas deposits may have a host of environmental concerns”. *Environ. Sci. Technol.*, *44*(15), 5679–5684.

Keator, A. E. (2018). *Geologic characterization and reservoir properties of the upper Smackover Formation, Haynesville Shale, and Lower Bossier Shale, Thorn Lake Field, Red River Parish, Louisiana, USA*. The Colorado School of Mines.

Kiepsch, S., & Pelster, R. (2016). Interplay of vapor adsorption and liquid imbibition in nanoporous Vycor glass. *Physical Review E*, *93*(4), 1–11.

Klemme, H. D. (1994). Petroleum system of the world involving Upper Jurassic Source Rocks. In *AAPG Memoir* (Vol. 60). 51-72.

Kwok, D. Y., & Neumann, A.W.U. (1999). Contact angle measurement & contact angle interpretation. *Advances in Colloid and Interface Science*, *8*, 167–249.

Lafargue, E., Marquis, F., & Pillot, D. (1998). Rock-Eval 6 Applications in hydrocarbon exploration, production, and soil Contamination studies. *Revue de l’Institut Français Du Pétrole*, *53*(4), 421–437.

Lan, Q., Xu, M., Binazadeh, M., Dehghanpour, H., & Wood, J. M. (2015). A comparative investigation of shale wettability: The significance of pore connectivity. *Journal of Natural*

Gas Science and Engineering, *27*, 1174–1188.

Li, J., Lu, S., Chen, G., Wang, M., Tian, S., & Guo, Z. (2019). A new method for measuring shale porosity with low-field nuclear magnetic resonance considering non-fluid signals. *Marine and Petroleum Geology*, *102*(January), 535–543.

Loucks, R. G., Reed, R. M., Ruppel, S. C., & Hammes, U. (2010). Preliminary classification of matrix pores in mudrocks. *Gulf Coast Association of Geological Societies Transactions*, *60*(2), 435–441.

Loucks, R. G., Reed, R. M., Ruppel, S. C., & Jarvie, D. M. (2009). Morphology, genesis, and distribution of nanometer-Scale pores in siliceous mudstones of the Mississippian Barnett Shale. *Journal of Sedimentary Research*, *79*(12), 848–861.

Lu, S., Xue, H., Wang, M., Huang, W., Li, J., Xie, L., … Liu, X. (2016). Several key issues and research trends in evaluation of shale oil. *Acta Petrolei Sinica*, *37(10)*, 1309–1322.

Makhanov, K., Dehghanpour, H., & Kuru, E. (2012). An Experimental study of spontaneous imbibition in Horn River Shales. *SPE Canadian Unconventional Resources Conference*,.

Mancini, E. A., Li, P., Goddard, D. A., Ramirez, V. O., & Talukdar, S. C. (2008). Mesozoic (Upper Jurassic-Lower Cretaceous) deep gas reservoir play, central and eastern Gulf coastal plain. *AAPG Bulletin*, *92*(3), 283–308.

Michel, G. G., Sigal, R. F., Civan, F., & Devegowda, D. (2011). Parametric investigation of shale gas production considering nano-scale pore size distribution, formation factor, and non-darcy flow mechanisms. *SPE Annual Technical Conference and Exhibition*.

Neithalath, N., Sumanasooriya, M. S., & Deo, O. (2010). Characterizing pore volume, sizes, and

connectivity in pervious concretes for permeability prediction. *Materials Characterization*, *61*(8), 802–813.

Nunn, J. A. (2012). Burial and thermal history of the Haynesville Shale: Implications for overpressure, gas generation, and natural hydrofracture. *GCAGS Journal*, *1*(1), 81–96.

Oil & Gas Journal. (2018). Goodrich to commence completion operations in Haynesville. Retrieved from https://www.ogj.com/articles/2018/03/goodrich-to-commence-completion-operations-in-haynesville.html

Parker, M. A., Buller, D., Petre, J. E., & Dreher, D. T. (2009). Haynesville Shale-Petrophysical Evaluation. *2009 SPE Rocky Mountain Petroleum Technology Conference*.

Peng, S., Hu, Q., & Hamamoto, S. (2012). Diffusivity of rocks: Gas diffusion measurements and correlation to porosity and pore size distribution. *Water Resources Research*, *48*(2), 1–9.

Peng, S., & Loucks, B. (2016). Permeability measurements in mudrocks using gas-expansion methods on plug and crushed-rock samples. *Marine and Petroleum Geology*, *73*, 299–310.

Reig, P., Luo, T., & Proctor, J. N. (2014). *Global Shale Gas Development*.

Rodriguez1, R., Crandall, D., Song, X., Verba, C., & Soeder1, D. (2014). *Imaging Techniques for Analyzing Shale Pores and Minerals*. Morgantown, WV.

Roychaudhuri, B., Tsotsis, T. T., & Jessen, K. (2013). An experimental investigation of spontaneous imbibition in gas shales. *Journal of Petroleum Science and Engineering*, *111*, 87–97.

Rystad Energy. (2019). Haynesville Shale set to surpass historical gas output record from 2011. Retrieved from https://www.rystadenergy.com/newsevents/news/press-

releases/Haynesville-Shale-set-to-surpass-historical-gas-output-record-from-2011/

Schlumberger. *sCore Lithofacies Classification Reveals Barnett Shale Reservoir Quality*. , (2014).

Schlumberger Oilfield Glossary. (2018). Geopressure gradient - Schlumberger Oilfield Glossary. Retrieved from https://www.glossary.oilfield.slb.com/en/Terms/g/geopressure_gradient.aspx

Shen, W., Xu, Y., Li, X., Huang, W., & Gu, J. (2016). Numerical simulation of gas and water flow mechanism in hydraulically fractured shale gas reservoirs. *Journal of Natural Gas Science and Engineering*, *35*(May), 726–735.

Boosari, S.S.H., Aybar, U., & Eshkalak, M. O. (2016). Unconventional resource's production under desorption-induced effects. *Petroleum*, *2*(2), 148–155. 4

Slatt, R. M. (2011). Important geological properties of unconventional resource shales. *Central European Journal of Geosciences*, *3*(4), 435–448.

Slatt, R. M., & O'Brien, N. R. (2011). Pore types in the Barnett and Woodford gas shales: Contribution to understanding gas storage and migration pathways in fine-grained rocks. *AAPG Bulletin*, *95*(12), 2017–2030.

Sondergeld, C., Newsham, K., Comisky, J., Rice, M., & Rai, C. (2010). Petrophysical considerations in evaluating and producing shale gas resources. *SPE Unconventional Gas Conference Held in Pittsburgh*.

Speight, J. G. (2017). Chapter Two - Reservoirs and Reservoir Fluids. *Deep Shale Oil and Gas*. Cambridge: Elsevier.

Swami, V., & Settari, A. (2012). A pore scale gas flow model for shale gas reservoir. *Americas Unconventional Resources Conference*.

Thomas, Y. (1804). An essay on cohesion of fluids. *Philosophical Transactions of the Royal Society of London*, *95*, 65–87.

Tian, W., Wu, X., Liu, D., Knaup, AmandaChen, C., & Sondergeld, C. (2019). Investigating effects of pore size distribution and pore shape on Radon production in Marcellus Shale Gas Formation. *Energy & Fuels*, *33*, 700–707.

Tinni, A., Fathi, E., Agarwal, R., Sondergeld, C. H., Akkutlu, I. Y., & Rai, C. S. (2012). Shale rermeability measurements onplugs and crushed Samples. *SPE Canadian Unconventional Resources Conference*.

Tissot, B. P., Pelet, R., & Ungerer, P. (1987). Thermal history of sedimentary basins, maturation indices, and kinetics of oil and gas generation. *AAPG Bulletin*, *71*(12), 1445–1466.

Tissot, B. P., & Welte, D. H. (1985). Petroleum formation and occurrence. In *Eos, Transactions American Geophysical Union* (Vol. 66).

Torsch, W. (2013). *Thermal and pore pressurehistory of the Haynesville Shale in North Louisiana : A two-dimensional numerical study of hydrocarbon generation, overpressure, and natural hydraulic frracture*. Louisiana State University.

U.S. Energy Information Administration. (2011). Review of Emerging Resources: U.S. Shale Gas and Shale Oil Plays. *U.S. Energy Information Administration Report*, (July), 105. Retrieved from ftp://ftp.eia.doe.gov/natgas/usshaleplays.pdf

U.S. Environmental Protection Agency. (2016). Hydraulic Fracturing for Oil and Gas: Impacts

from the Hydraulic Fracturing Water Cycle on Drinking Water Resources in the United States. In *EPA's Study of Hydraulic Fracturing and Its Potential Impact on Drinking Water Resources*. Retrieved from https://www.epa.gov/hfstudy/hydraulic-fracturing-water-cycle%0Ahttps://www.epa.gov/sites/production/files/2016-12/documents/hfdwa_executive_summary.pdf

U.S. Geological Survey. (2017). USGS Estimates 304 Trillion Cubic Feet of Natural Gas in the Bossier and Haynesville Formations of the U.S Gulf Coast.

Wang, F. P., & Hammes, U. (2010). Key petrophysical factors affecting fluid flow in geopressured Haynesville Shale. *AAPG Search and Discover*, (April 2010), 90104.

Wang, F. P., & Reed, R. M. (2009). Pore Networks and Fluid Flow in Gas Shales. *2009 SPE Annual Technical Conference and Exhibition*.

Wang, Q., Chen, X., Jha, A. N., & Rogers, H. (2014). Natural gas from shale formation - The evolution, evidences and challenges of shale gas revolution in United States. *Renewable and Sustainable Energy Reviews*, *30*, 1–28.

Washburn, E. W. (1921). Note on a method of determining the distribution of pore size in a porous material. *Physics*, *7*, 115–116.

Yang, R., Guo, X., Yi, J., Fang, Z., Hu, Q., & He, S. (2017). Spontaneous Imbibition of Three Leading Shale Formations in the Middle Yangtze Platform, South China. *Energy and Fuels*, *31*(7), 6903–6916.

Yuan, W., Pan, Z., Li, X., Yang, Y., Zhao, C., Connell, L. D., Li, S., He, J. (2014). Experimental study and modelling of methane adsorption and diffusion in shale. *Fuel*, *117*(PART A),

Zhang, C., Gamage, R. P., Perera, M. S. A., & Zhao, J. (2017). Characteristics of clay-abundant shale formations: Use of CO2 for production enhancement. *Energies*, *10*(11), 5–7.

Zhou, Z., Hoffman, B. T., Bearinger, D., & Li, X. (2014). Experimental and numerical study on spontaneous imbibition of fracturing fluids in shale gas formation. *SPE/CSUR Unconventional Resources Conference*.

Zou, C. (2013). Shale gas. In *Unconventional Petroleum Geology*, pp. 149–190.

Biographical Information

Qiming Wang is from Qianjiang, Hubei, China and entered the Yangtze University (YU) in 2012 as petroleum geology major student. After two and half years in the Yangtze University, he transferred to the Missouri University of Science and Technology (MST). After another two and half years majored in geology & geophysics, he received bachelor of science from MST and bachelor of engineering from YU. In 2017, he joined the University of Texas at Arlington as a master's student. In the following two years, he showed special interests in the nano-petrophysics field as his MS thesis topics. His career goals include a PhD degree and a satisfying career in universities or research and development institutes.